SPECTROSCOPY OF DEFECTS IN GALLIUM OXIDE

By

JACOB RUDOLPH RITTER

A dissertation submitted in partial fulfillment of
the requirements for the degree of

DOCTOR OF PHILOSOPHY

WASHINGTON STATE UNIVERSITY
Department of Physics and Astronomy

DECEMBER 2019

To the Faculty of Washington State University:

The members of the Committee appointed to examine the dissertation of JACOB RUDOLPH RITTER find it satisfactory and recommend that it be accepted.

_____

Matthew D. McCluskey, Ph.D., Chair

_____

Yi Gu, Ph.D.

_____

Kelvin Lynn, Ph.D.

ACKNOWLEDGMENTS

My advisor, Matt McCluskey, for teaching me some fraction of the physics that he knows and supporting and guiding me in all my research.

The Kelvin Lynn lab for growing all of my Ga_2O_3 samples.

My cohort, for the help they gave me in my first two year of classes and the fun they provided in the next 4 years of research.

My lab mates, for always lending a helping hand and letting me bounce ideas off of them.

My parents, who always encouraged my learning and education every single step of the way.

My wife, Megan, who carried me through all of my complaining and panic attacks and made Pullman a wonderful place to be.

The financial support from the DOE. This research was supported by the U.S. Department of Energy, Office of Basic Energy Sciences, Division of Materials Science and Engineering under Award DE-FG02-07ER46386.

SPECTROSCOPY OF DEFECTS IN GALLIUM OXIDE

Abstract

by Jacob Rudolph Ritter, Ph.D.
Washington State University
December 2019

Chair: Matthew D. McCluskey

β-Gallium oxide (β-Ga_2O_3) is a promising semiconductor for its potential as a material in the field of power electronics. Magnesium doping of Ga_2O_3 has been shown to create a semi-insulating material, which could be utilized in ultrahigh-power devices. The properties of iridium impurities in undoped, magnesium-doped, and calcium-doped gallium oxide were investigated with IR spectroscopy. In undoped and Ca-doped β-Ga_2O_3, IR peaks at 3313, 3450, and 3500 cm^{-1} are tentatively assigned to O–H bond stretching modes of IrH complexes. Hydrogen-annealed Ga_2O_3:Mg shows an IR peak at 3492 cm^{-1}, and H-annealed Ga_2O_3: Ca shows an IR peak at 3441 cm^{-1}. These are assigned to an O-H bond-stretching mode of a neutral MgH and CaH complex, respectively. Polarization experiments were used to place the O-H bond of the MgH complex in the *a*-*c* plane. Mg, Ca, and Fe doped samples show an Ir^{4+} electronic transition feature at 5148 cm^{-1}. By measuring the strength of this feature versus photoexcitation, the $Ir^{3+/4+}$ donor level was determined to lie 2.2-2.3 eV below the conduction band minimum, which matches theory. Ga_2O_3:Mg also has a range of sidebands between 5100 and 5200 cm^{-1}, attributed to IrMg pairs. Polarized IR measurements were used to show that the 5148 cm^{-1} peak is anisotropic, weakest for light polarized along the **c** axis.

TABLE OF CONTENTS

Page

LIST OF TABLES

Page

LIST OF FIGURES

Page

Dedication

To Megan, easily the best thing I got out of grad school

CHAPTER ONE: INTRODUCTION

Modern technology is built on a mountain of previous scientific and technologic discoveries. From the microchips in our computers to switches and junctions in our power plants, semiconductors play a crucial role in an inconceivably large number of modern tools. However, none of these tools started out as clean and optimized devices. It took decades of work between Schottky's first conceptual theories on semiconductor junctions[1] and the first functional transistor at Bell Labs in 1947.[2] H. J. Round first noted light emitting properties from a semiconductor in 1907[3], and new advances and uses in LED technology are still being produced every year.[4,5]

Because there is always room for improvement in semiconductor technologies, semiconductor research often involves attempting to use new materials in roles where other materials already have had some success. To do this, characterization of the properties of the new material is an important early step in bringing that semiconductor into use. The focus of this dissertation, gallium oxide (β-Ga_2O_3), has been rapidly emerging as a potential player in the field of power electronics. Typically, ultrahigh-voltage power switching applications utilize silicon carbide (SiC) or gallium nitride (GaN), but as gallium oxide's properties are better understood it shows potential to replace them in many applications if some limitations are overcome.

This dissertation and the motivation for this research is based on the promise of what gallium oxide could be. But before gallium oxide-based power devices can give us unlimited energy and flying cars (or perhaps instead more realistic advances in power switching technology), we first must understand the properties and limitations of it as a material. The present work uses characterization techniques, primarily spectroscopic, to study undoped Ga_2O_3

as well as the effect of several dopants. The dissertation structure is as follows: Chapter 1 introduces some necessary basics on semiconductors and then reviews Ga_2O_3 as a material, briefly covering some recent literature. Chapter 2 details the experimental techniques and characterization tools utilized in this body of work. Chapter 3 describes the common methods of crystal growth for thin film and single crystal semiconductors. Chapter 4 contains the primary focus of this work, detailing our characterization of gallium oxide with iridium, magnesium, calcium, and other dopants. Chapter 5 concludes this work's findings for research in Ga_2O_3. Chapters 6 and 7 cover materials research not related to the primary field of gallium oxide, but that have yielded publications during my graduate study. Chapter 6 discusses Raman studies of zinc sulfide oxide alloys (ZnS_xO_{1-x}) and Chapter 7 investigates the effects of substrate surface interactions on the luminescence and absorption of the pyrene molecule.

1.1: Introduction to semiconductors

1.1.1: Definitions

A material is usually defined as a semiconductor when its electrical resistivity falls in the range of 10^{-2} to 10^{-9} Ω·cm.[6] In other words, it is not conducting enough to qualify as a conductor or metal, but conducts too well to be a proper insulator.

Another way to define a semiconductor is through the behavior of its electrons. The complicated atomic structure of a semiconductor gives rise to allowed energies for the electrons to occupy. These allowed levels are referred to as energy *bands.* When a material is at absolute zero, which means not stimulated by any external energies at all, the bands that are filled with electrons are known collectively as the *valence band*, and the empty bands are the *conduction band* (Fig. 1.1). The highest allowed point in the valence band is the *valence band maximum*

(VBM), and the lowest energy point of the conduction band is the *conduction band minimum* (CBM). The space between the VBM and CMB is the *band gap*, the zone forbidden to the electrons of a perfect semiconductor.

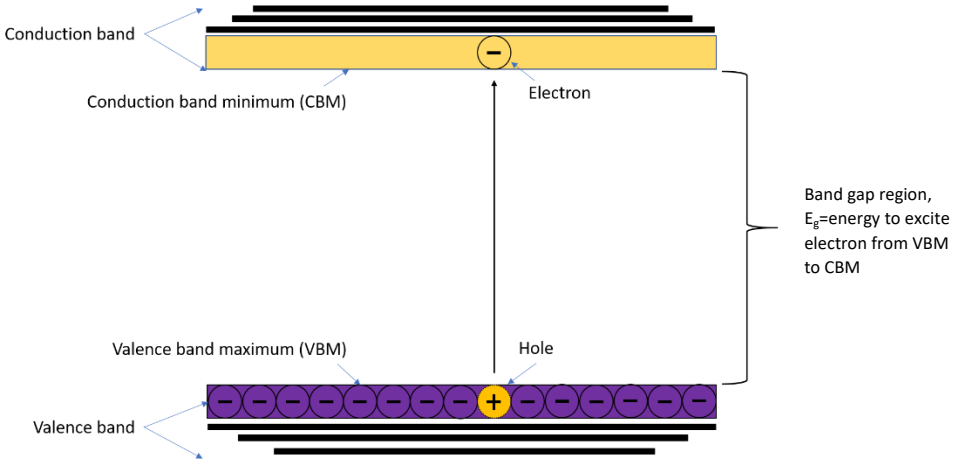

Figure 1.1: Basic band gap diagram. Electrons stimulated by energy E_g can move from the valence band to the conduction band, leaving a positively charged hole behind.

A material with a band gap of 0 is a metal. Electrons are free to move along in the conduction band of the material, so a metal conducts electricity easily. In an insulator, the gap is exceedingly large, so it takes too much energy to promote the electrons from the VBM to the CBM. The electrons stay locked in the valence band and so the material does not conduct electricity. A semiconductor is a material that splits the difference. A semiconductor is sometimes defined as a material whose band gap is between 0 and 3 electron volts (eV). These specific numbers should be taken with grain of salt, especially in the context of this dissertation. Gallium oxide is what is known as a wide band gap semiconductor and has a gap of ~4.8 eV. Even some materials normally considered to be an insulator, like diamond or aluminum nitride, can be treated as a semiconductor with band gaps of up to 6 eV.

An electron promoted to the conduction band is free to move along the crystal. Because an electron carries a negative charge, it can carry current through the material. For this reason, an electron in the conduction band is known as a *charge carrier*. Meanwhile, in the valence band, the space once occupied by the electron is now empty, which means it has a positive charge compared to its default filled state. This space where an electron should be is called a *hole* (Fig 1.1), which we treat as a quasi-particle with mass, charge, and energy. Because any of its neighboring electrons in the valence band can easily move to fill it, the hole can drift along the valence band, carrying positive charge much the way an electron carries a negative charge.

The electron enters the conduction band and a hole is created when enough energy is given to the system to excite the electron across the gap. This can occur thermally; as temperature increases the likelihood of finding electrons in the conduction band also increases. The probability of finding electrons in any given state is given by the *Fermi-Dirac distribution:*

$$f(E) = \frac{1}{e^{\frac{(E-E_F)}{k_B T}} + 1} \tag{1.1}$$

E_F is the *Fermi energy*, which is the energy of the highest state that would be filled at absolute zero. T is the temperature of the semiconductor and k_B is the Boltzmann constant. This means that $f(E)$ is the probability that a state with energy E will be occupied by an electron. At absolute zero the probability of finding electrons in states above E_f is 0 and below E_f is 1 (Fig. 1.2). As temperature increases, the probability of finding electrons above the Fermi energy increases and below decreases as electrons are thermally excited across the band gap. At room temperature, this effect is small for wide band gap semiconductors but significant for semiconductors with smaller gaps.

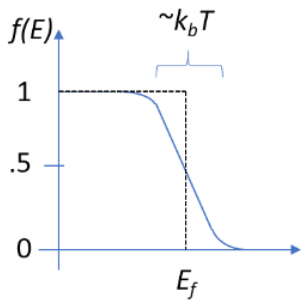

Figure 1.2: Fermi-Dirac distribution for T>0 (solid line) and T=0 (dotted line).

Another way to excite an electron from the valence band to the conduction band is through photon absorption. When a photon of sufficient energy strikes the material, the photon is absorbed and that energy is used to make an electron jump the gap (Fig. 1.3). When this occurs, it can be described as the creation of an *electron-hole pair*. The reverse of this process is called *emission*. Without continued excitation, the electrons in the highest bands want to relax back down to the lowest unfilled states. An electron-hole pair is destroyed, and to conserve energy a photon of the equivalent energy is emitted in a process called *radiative recombination*.[6] It is also possible to have *non-radiative* processes, if energy is converted into heat or some other means.

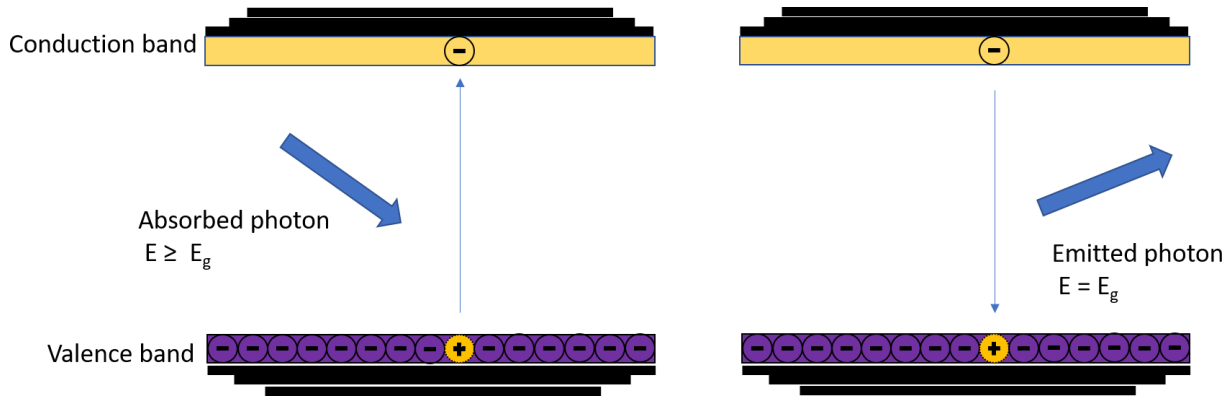

Figure 1.3: Demonstration of the radiative recombination process. When the electron absorbs a photon with the energy of the gap it is excited to the conduction band. When it falls back to the valence band, a photon of equivalent energy is emitted.

At temperatures above absolute zero, atoms in a crystal oscillate around their equilibrium positions collectively in what are called *lattice waves*.[7] These waves are quantized into *phonons*. In addition to energy, phonons have crystal momentum defined by $\hbar\mathbf{K}$, where $\mathbf{K}$ is a wavevector in the direction of wave propagation. Energy bands are often described in terms of energy (E) and a vector $\mathbf{k}$ in momentum space. In this way, a band gap can either be *direct* or *indirect* (Fig. 1.4). When a band gap is direct, the transition from VBM to CBM requires only the energy from a photon, which carries effectively no momentum. When the gap is indirect, the lowest point in the CBM is shifted in momentum space from the highest point of the VBM. In order for a transition between the two to occur, momentum must be conserved, so this process requires both a photon and a phonon. The phonon energy $\hbar\boldsymbol{\Omega}$ is much smaller than the size of the gap, typically 10s of meV, so on this scale it corresponds only to a horizontal transition, much like the photon can be approximated as only a vertical transition.

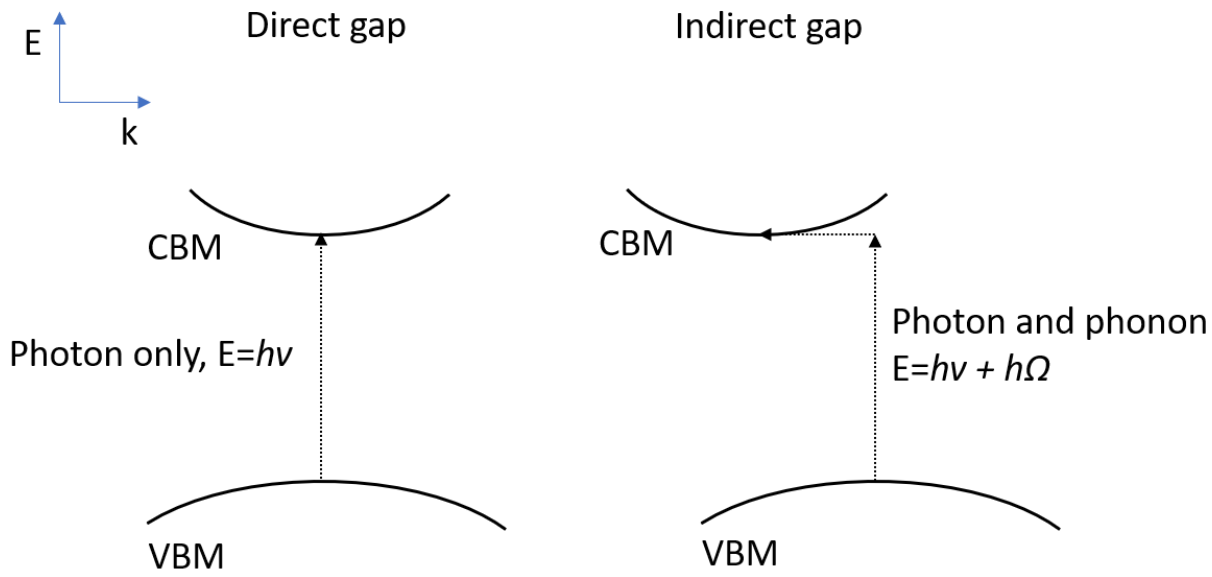

Figure 1.4: Comparison between the processes of indirect and direct band gaps.

Whether or not a band gap is direct or indirect is an important characteristic for many semiconducting roles. Because the indirect gap process requires multiple particles, the radiative recombination process is probabilistically less likely, so an indirect gap material like silicon makes poor light emitting devices compared to a direct gap material like GaN.

1.1.2: Crystal structure and defects

The structure of a semiconductor can most often be described as a crystal. This means that its atoms are arranged in a highly ordered manner and extend in a repeating pattern in all directions to form the *crystal lattice* of the material. The smallest grouping of atoms of the material that still contains the symmetry of the lattice is called the *unit cell*. The lattice can be built by copying and repeating the unit cell in all directions. Most semiconducting crystals (though not Ga_2O_3) can be described by a cubic cell (Fig. 1.5).

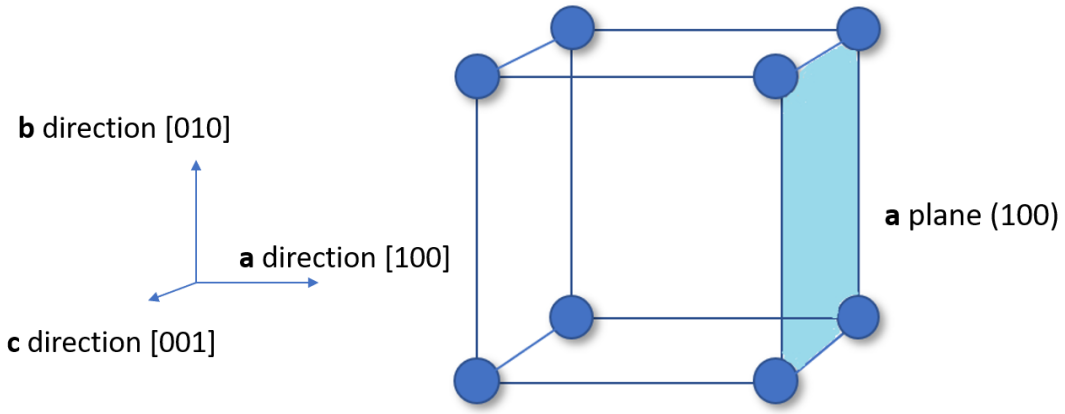

Figure 1.5: Example of directions and the (100) plane for a cubic cell.

Directions are defined from the origin of the cell and expressed [*xyz*], such that [100] is pointing in only the **x** direction. An atomic plane is noted (*hkl*) and is perpendicular to the direction [*hkl*], where *h*, *k*, and *l* are known as the *Miller indices.* This means that when in a later chapter I describe light as incident to the (100) surface of a gallium oxide crystal, light is striking the sample traveling along the [100] direction. Often these directions are also referred to as the **a**, **b**, and **c** directions, where the *a* plane is formed by the **b** and **c** axes and perpendicular to the **a** axis.

Semiconductors can be classified as *elemental* or *compound*. An elemental semiconductor is composed of a single species of atom, so every lattice point in the crystal is the same atom if there are no defects. Compound semiconductors are formed from two or more species of atom. The simplest compound semiconductors are referred to by the groups their elements belong to in the periodic table. Gallium is in group III and arsenic is in group V, so gallium arsenide (GaAs) is called a III-V semiconductor. Zinc is group II and oxygen is group

VI, so zinc oxide (ZnO) is a II-VI semiconductor. This naming scheme is only typically applied to two-atom compound semiconductors.

The crystal cell of a semiconductor is entirely dependent on the elemental makeup. There are 14 distinct types of cells that have the necessary translational symmetry to create a crystal lattice. These are known as *Bravais* lattices.[8] A cubic cell can be *primitive*, with only eight corners, *body-centered*, with eight corners and a lattice point at the center, or *face-centered*, with lattice points at the corners and also the center of each face (Fig. 1.6).

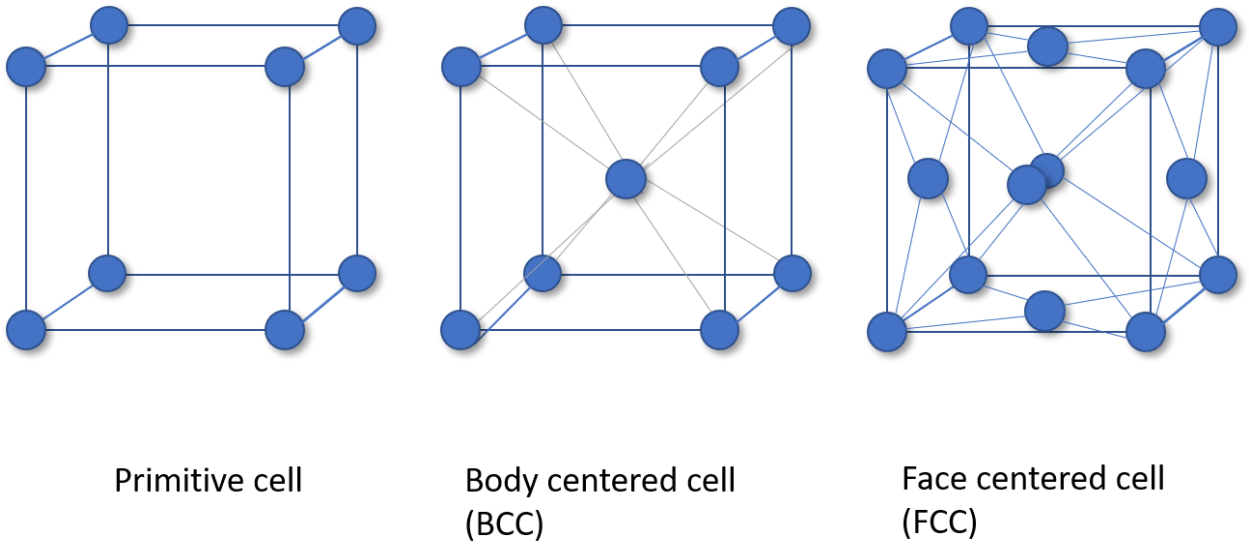

Figure 1.6: Bravais lattice options for a cubic cell.

The most common elemental semiconductors, carbon, silicon, and germanium, have what is known as the diamond structure. They have a face-centered cubic cell with atoms at each face and corner, and each of those atoms has a second atom displaced by (a/4, a/4, a/4), where a is the length of the cell, also known as the *lattice parameter* (Fig 1.7).

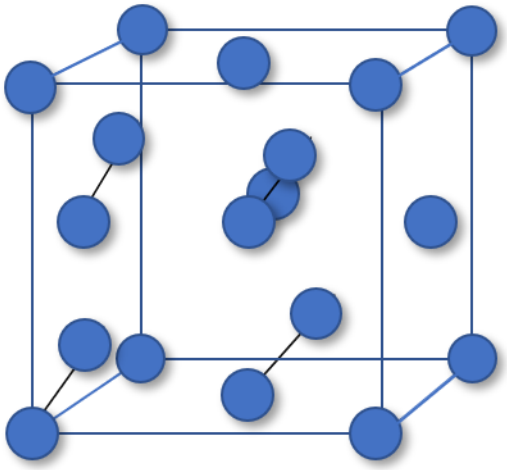

Figure 1.7: Example of diamond cell, like C, Si, and Ge.

Most simple compound semiconductors have what is known as the *zinc blende* structure. This is the exact same structure as the diamond cell, but the displaced atoms are the second elemental species (Fig. 1.8). Common semiconductors with the zinc blende structure are zinc sulfide (ZnS), GaAs, and gallium phosphide (GaP).

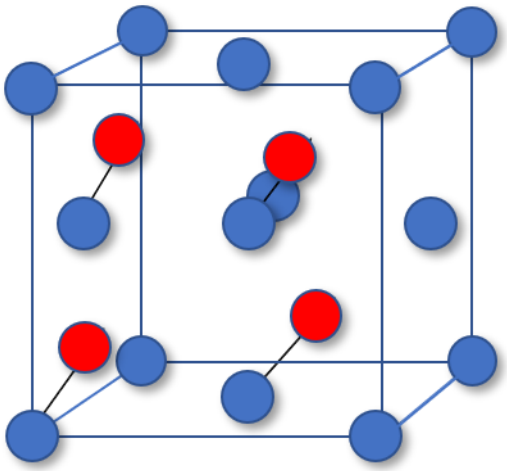

Figure 1.8: Example of zincblende cell, e.g. GaAs.

A third important structure is not cubic, but hexagonal. Some semiconductors discussed in this work like zinc oxide (ZnO) and GaN have what is known as the *wurtzite* structure (Fig

1.9). The wurtzite structure also has two species of atoms, but the unit cell is one sixth of a hexagonal shape and is only symmetric around the vertical *c* axis.

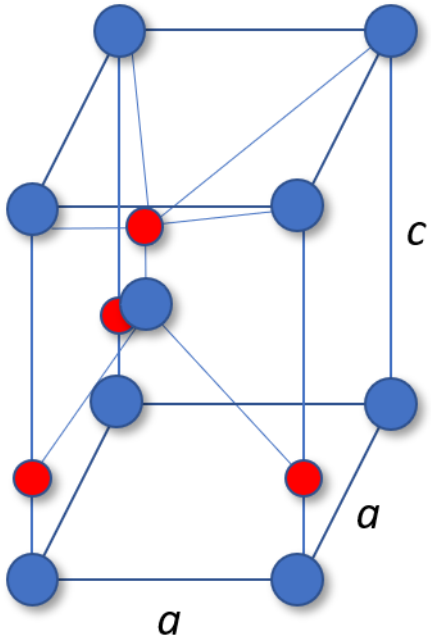

Figure 1.9: Example of a wurtzite crystal cell, e.g. ZnO.

Together, the diamond, zinc blende, and wurtzite structures cover the majority of important semiconductors.[7] One last structure very important to this body of work is that of gallium oxide, which has the monoclinic crystal structure (Fig. 1.10). In a monoclinic crystal structure, the angle between **a** and **c** departs from 90 degrees and described by the β variable, so most of the symmetry is lost. The **b** axis still perpendicular to the (010) plane but due to the angle between **a** and **c**, **a** is not perpendicular to the (100) plane and **c** is not perpendicular to the (001) plane.

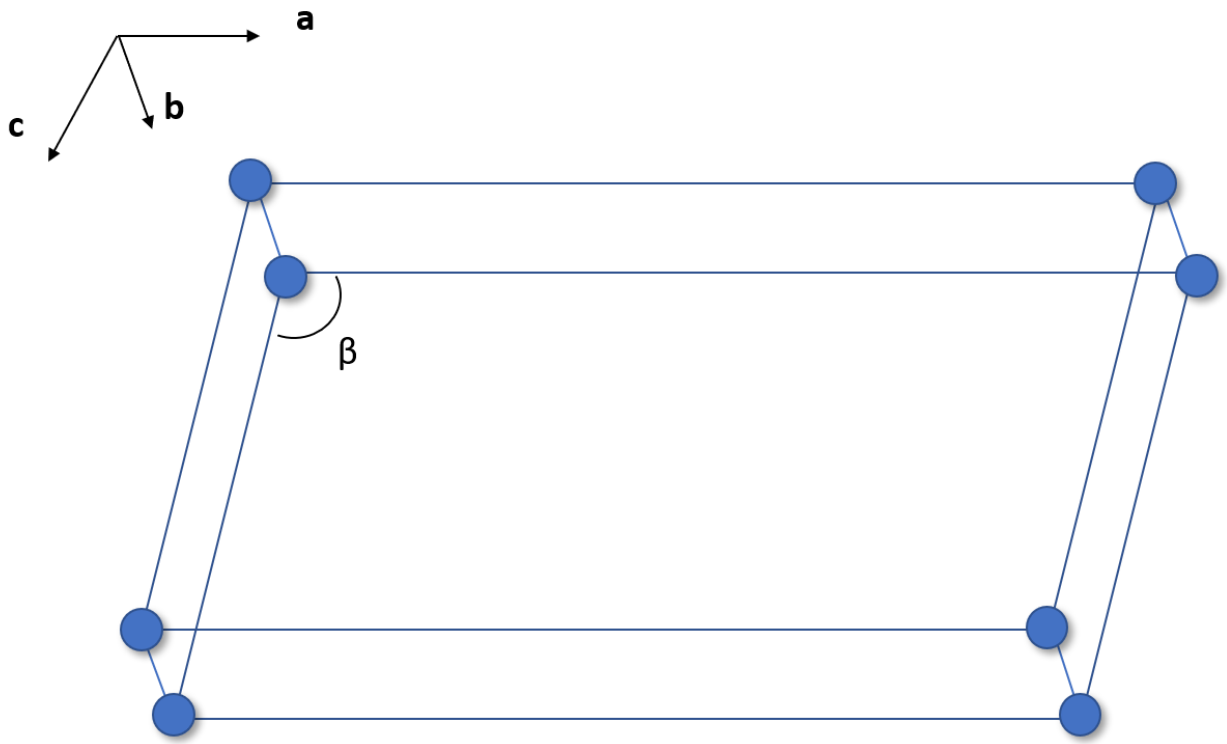

Figure 1.10: General shape of a monoclinic crystal cell, like that of Ga_2O_3.

1.1.3: Defects and dopants

One of the most interesting and useful aspects of semiconductors is how much their properties can change in the presence of defects. Defects can be classified as *point defects* and *line defects.* Line defects involve rows of atoms and misalignment of sections of crystal lattices. As such, line defects are always detrimental to devices.[6] Point defects, and also small groups of point defects known as *complexes*, are much more interesting.

Point defects can further be classified in the following groups:

- *Vacancy*: Missing atom *A* is written as V_A
- *Interstitial*: Atom *A* is located interstitially between normal sites, written I_A

- *Substitutional*: Atom *B* has replaced atom *A* on what is normally atom *A*'s site, written B_A
- *Frenkel defect pair*: a V_A-I_A complex in which atom *A* moves from its normal site to an interstitial.

A defect is *native* if it doesn't involve any atoms foreign to the crystal, and *extrinsic* if it does.

An important feature of defects is that they are usually electrically active. Defects that contribute free electrons, and therefore negative charge carriers, to the host crystal are known as *donors*. Defects that contribute positively charged holes can accept electrons in the crystal, and so are known as *acceptors.* Semiconductors in which the majority of charge carriers are electrons are referred to as *n-type*. When the majority of charge carriers are holes, the material is referred to as *p-type*. The inclusion of enough donor defects can make a semiconductor *n*-type and enough acceptors can make it *p*-type. Entire lifetimes of work have gone into the many varied and useful devices that are created from application of *p-n* junctions, from diodes to solar cells to rectifiers for power devices.

In a pure semiconductor, the band gap is a region where electronic states are disallowed. Adding defects to the material can introduce states inside the gap that are electrically active, both for donors and acceptors. This means that many of the properties of the material can be expected to change. One example is the absorption and emission properties of the material (Fig. 1.3). In the defect-free case only energy contributions equal to or greater than the gap can excite the electrons, and likewise the only possible emission is slightly less than the band gap energy. In a real, defective system defect states allow for a much more unique and complicated system of absorption and emission. From an electron excited to the conduction band with even a single

defect state, it is now possible to have emission from CBM to VBM, CBM to defect state, and defect state to VBM.

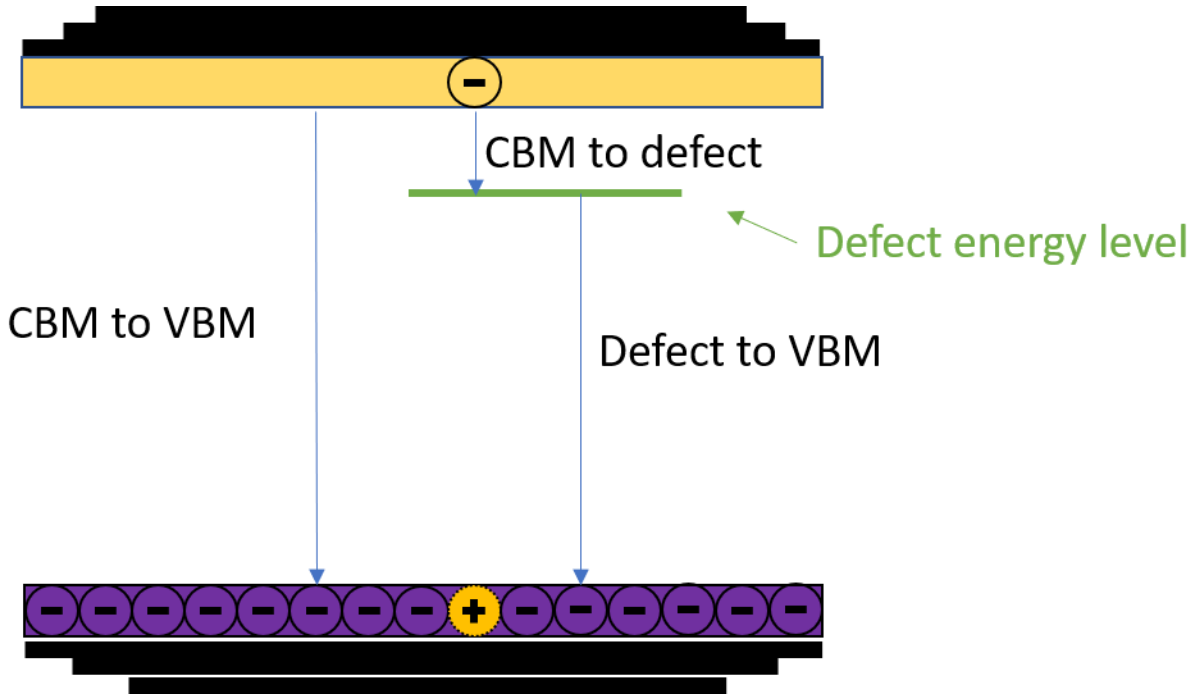

Figure 1.11: Radiative emission process with a defect state present. Even a single level opens up many more options for emission and absorption energies.

Even this is much more simple than a real crystal, where defects can have several levels each and many defects are possible. ZnO doped with copper is a good example of this complication. The band gap of ZnO is 3.37 eV, but by doping ZnO with copper it is possible to create a lower energy blue-green emission of ~2.6 eV. [9,10]

A *shallow* center is a level inside the band gap caused by a defect that doesn't take much energy to ionize. A *deep* center is any center that is not shallow, so usually closer to the center of the gap. Deep donors and acceptors do not do as much for the conduction of the material, as it takes much more to free the electrons from those levels. They can, however, compensate

shallow impurities. A shallow donor level is close to the conduction band edge and a shallow acceptor is close to the valence band edge. Consider a phosphorus (P) atom substituted into silicon. The P nucleus has an extra positive charge and so has an extra valence electron. This extra valence electron is only loosely bound to the P atom when in the Si crystal, so it is easily ionized thermally. For this reason, P is a donor in Si, and deliberate addition of P impurities can make Si into a more *n*-type material. Likewise, boron (B) can act as an acceptor in Si and be used to make it *p*-type.

This controlled and deliberate introduction of impurities into a semiconductor is referred to as *doping*. There are many ways to dope a semiconductor, both during growth and after. For larger atomic impurities it is common to include small concentrations of the impurity during growth processes. For smaller atoms like hydrogen it is possible to simply diffuse the atom into the crystal thermally. Dopants must be in the correct substitutional or interstitial lattice points to act as electrically active donors/acceptors. The process of heating a sample to move impurities to the appropriate sites is known as thermal *annealing*.

1.1.4: Vibrational properties of semiconductors

Defects also create changes in the vibrational properties of semiconductors.[11] Because of their perfect symmetry, the atoms in a crystal lattice vibrate together in lattice waves. When a light-mass defect is introduced, this symmetry is broken by the change in mass at that point and new vibrational modes will arise. These vibrational modes are localized to real space relative to their neighboring atoms and are referred to as *local vibrational modes* (LVM). Following the discussion in Chapter 5 of McCluskey and Haller[7], in 1 dimension this can be demonstrated using a diatomic linear chain (Fig. 1.12).

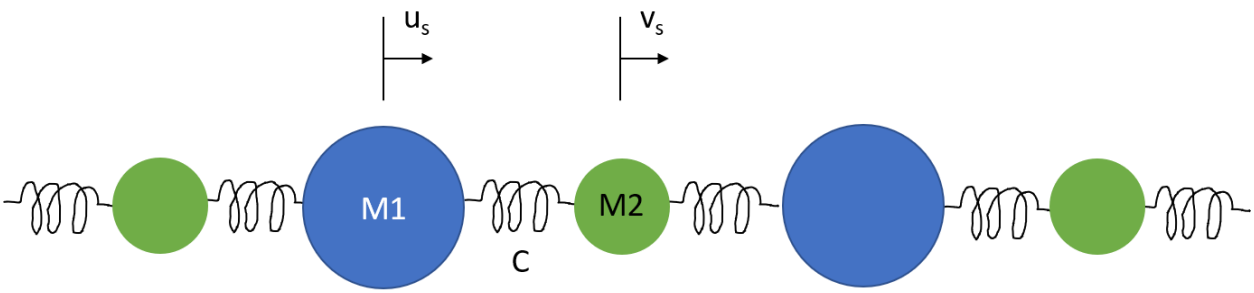

Figure 1.12: Simple model of a diatomic linear chain.

For a pure lattice, the displacement of the atoms from their equilibrium points is given by a linear superposition of the lattice waves in complex exponentials:

$$u_s = u_K e^{i(Ksa-\omega t)} \tag{1.2}$$

$$v_s = v_K e^{i(Ksa-\omega t)} \tag{1.3}$$

u_s and v_s are the displacements of M_1 and M_2, $K = 2\pi/\lambda$ is the wave momentum, and ω is the frequency of a normal-mode oscillation. The equations of motion are given by:

$$M_1\ddot{u}_s = C(v_{s-1} + v_s - 2u_s) \tag{1.4}$$

$$M_2\ddot{v}_s = C(u_s + u_{s+1} - 2v_s) \tag{1.5}$$

where C is the spring constant. Choosing the normal modes to be given by

$$u_s = u_s^0 e^{-i\omega t} \tag{1.6}$$

$$v_s = v_s^0 e^{-i\omega t} \tag{1.7}$$

and substituting them into equations 1.4 and 1.5 gives

$$\left(\frac{2C}{M_1} - \omega^2\right) u_s - (C/M_1)(v_{s-1} + v_s)) = 0 \quad (1.8)$$

$$\left(\frac{2C}{M_2} - \omega^2\right) v_s - (C/M_2)(u_{s+1} + u_s)) = 0 \quad (1.9)$$

where the eigenvalues ω and modes can be determined numerically. In the case of an added mass defect one of the atoms in the chain can be replaced by a new mass *m*. Diagonalizing the matrix created from 1.8 and 1.9 gives rise to a new mode. Unlike the uniform vibrations of the lattice, it has a decaying vibrational amplitude (Fig. 1.13). This vibration can then be studied spectroscopically, using some of the methods described in chapter 2.

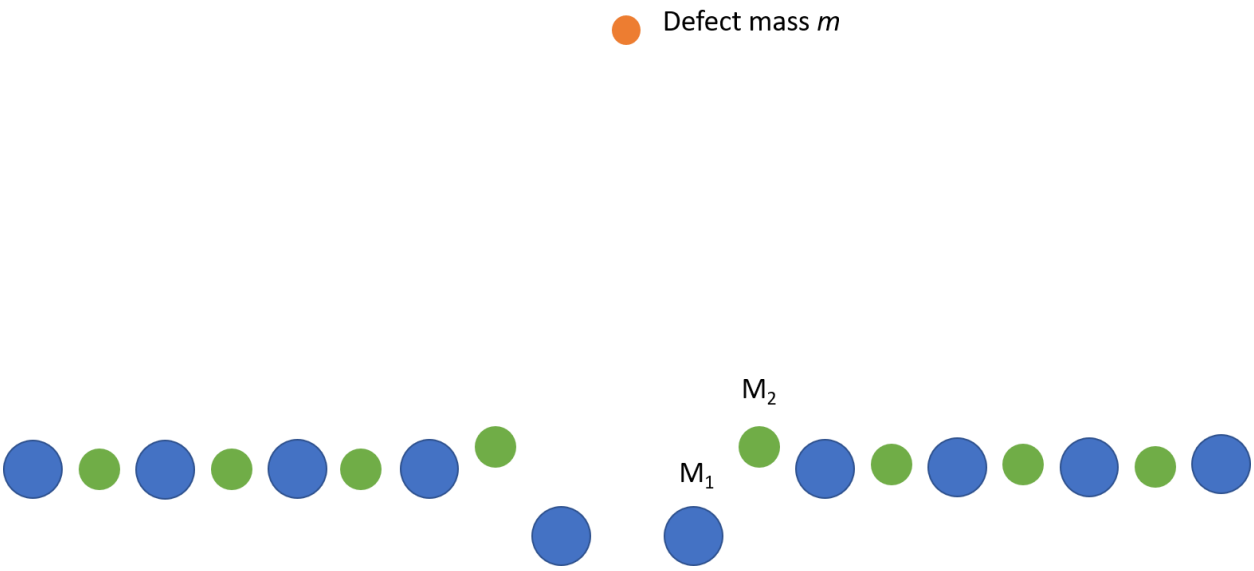

Figure 1.13: Example of a mass defect causing a local vibrational mode in a diatomic chain.

1.2: Introduction to gallium oxide

1.2.1: Basics of Ga_2O_3

Gallium oxide is a transparent semiconducting oxide (TSO) discovered in 1875 with the discovery of the element gallium and its possible compounds.[12] It has many possible phases, noted α-, β-, γ-, δ-, and ε-. Of these, our focus is on the β phase. The β phase is the only truly stable phase, and as such baking any other Ga_2O_3 polymorph in air at a high enough temperature will result in β-Ga_2O_3. Because of this, and because of the properties of the material, all our work focuses on β-Ga_2O_3. Unless otherwise noted, for the remainder of this work discussion of Ga_2O_3 can be interpreted as β-Ga_2O_3.

Gallium oxide's crystal structure is monoclinic, as described in section 1.1. This means that it has 3 different lattice parameters: a = 12.23 Å, b = 3.04 Å, and c = 5.80 Å. The angle between **a** and **c** is designated β = 103.7°. It has an indirect band gap of 4.83 eV, and an only slightly larger direct gap of 4.87 eV.[13]

Ga_2O_3 is intrinsically very *n*-type, and any successful reports of *p*-type gallium oxide growth are highly controversial. There have been claims of nitrogen doped nanowires with *p*-type behavior, but the *p*-type measurements were based exclusively on I-V (current-voltage) measurements with no analysis of carrier concentration or mobility.[14] It may be the case that functional *p*-type conductivity is not possible in gallium oxide, if any good shallow acceptors cannot be found. Magnesium has been shown in several studies to greatly increase the insulating properties of gallium oxide.[15,16] From this it can be interpreted that Mg shows some compensating acceptor traits, and on this foundation much of our research and doping is based.

1.2.2: Research in Ga_2O_3

In the last few years, gallium oxide has become a much-investigated material for all of the reasons previously stated. The types of studies reported on for gallium oxide can be broken into three broad categories: growth, characterization, and devices.

Studies on material growth report on the many ways researchers have produced both bulk and thin film gallium oxide samples. Thin films have been produced via sputtering,[17] metal-organic chemical vapor deposition (MOCVD)[18], and many other deposition methods.[19,20] The techniques of bulk crystal growth are being constantly refined, and high quality Ga_2O_3 crystals have been grown with all of the modern methods described in Chapter 3, including float zone[21], edge defined film fed[22], and Czochralski[16,23] growth techniques. For my work, we did not grow any of the materials ourselves, but rather acquired our single crystal samples from Professor Kelvin Lynn's group at the WSU Institute for Material Research or commercial producers. While my studies are not on the growth processes involved, all of the work done on the subject is very important to us, because without high quality crystals it is impossible to perform proper characterization.

This dissertation falls in the category of characterization. Gallium oxide has only been an exciting material for study for the last 1-2 decades, and as such there is much to be understood about the material. Work has been done to understand everything about gallium oxide as a material from luminescence[15] to band structure[24]. Joel Varley at Lawrence Livermore National Labs has collaborated with many different groups, including our own, and helped model in great detail many of the traps and defect levels for a large number of dopants in gallium oxide.[25–27]

Devices are the future of gallium oxide. Early studies by Higashiwaki *et al*. have put forward the idea that gallium oxide is an ideal material for power electronics.[28,29] The high breakdown voltage and wide band gap of the Ga_2O_3 rivals or surpasses that of current high power device materials, and it is much cheaper to grow.[28] They have recently demonstrated the ability to make metal-semiconductor field-effect transistors (MESFETs) and Schottky barrier diodes (SBDs), so early device experimentation for gallium oxide has begun.[30]

CHAPTER TWO: EXPERIMENTAL TECHNIQUES

2.1: Fourier transform infrared spectroscopy (FTIR)

Fourier transform infrared spectroscopy is a spectroscopic technique commonly used to measure the intensity of infrared radiation as a function of frequency. In the field of semiconductors, this is useful for measuring the free carrier absorption and local vibrational modes. An FTIR is based on the setup of the Michelson interferometer (Fig. 2.1).

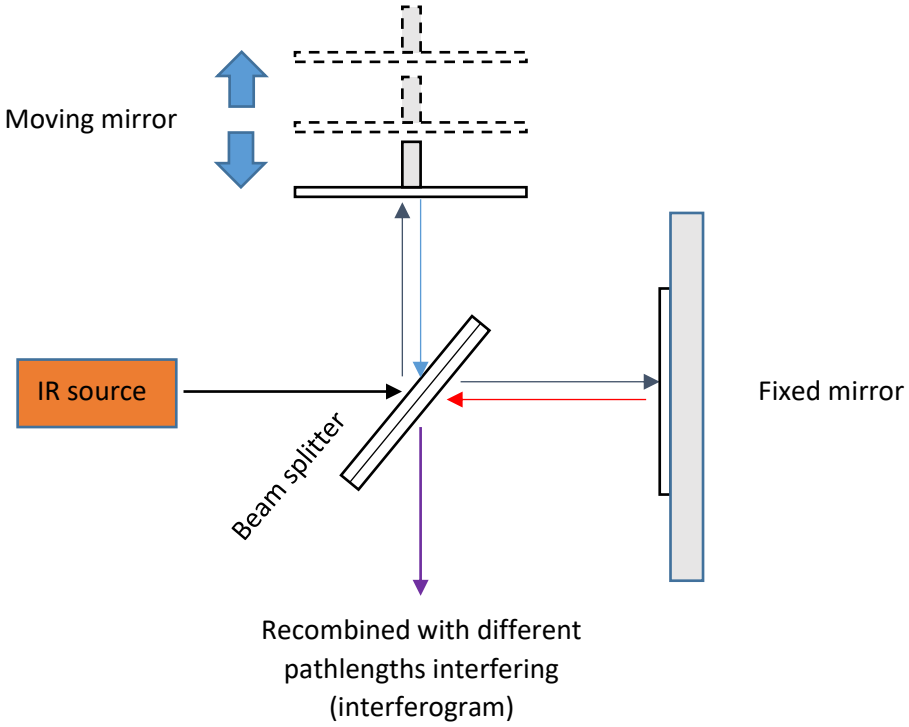

Figure 2.1: Diagram depicting a generalized Michelson interferometer.

The interferometer uses a beam splitter to split the infrared beam source beam and reflect off both a fixed mirror and a mirror set to vary the pathlength very precisely. The beams are then recombined by the beam splitter, where the different phases induced by difference in pathlength

cause the beams to interfere with one another. This resultant signal is known as an "interferogram", an example of which can be seen in figure 2.2.

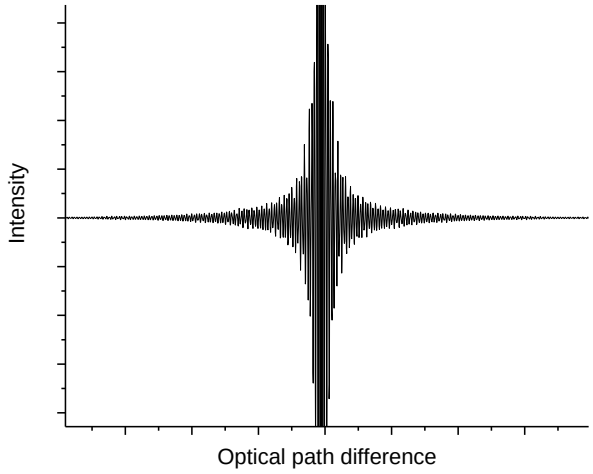

Figure 2.2: Interferogram of low temperature background signal for our FTIR system.

This interferogram signal contains one of the primary advantages of FTIR spectroscopy over other IR measurements: it holds the information from all measured wavelengths simultaneously. Instead of scanning across all wavelengths individually with a monochromator, an FTIR increases signal to noise by averaging across multiple scans and allows for a shorter scan time for the same resolution. This is referred to as the *Fellgett* advantage. The resolution is proportional to the length of the movement of the mirror. Because FTIR instruments do not require slits to achieve resolution, much greater throughput is achieved compared to a system that uses a grating. This is referred to as the *Jacquinot* advantage.[7]

The interferogram signal leaves the interferometer and then passes through the sample, where the material being measured absorbs energy. The light transmitted through (or reflected off, depending on the system/setup) is then measured by the detector, still in interferogram form. The detector digitizes the interferogram signal, and the computer uses fast Fourier transformations (FFT) to unpack the data into a more scientifically useful and recognizable spectrum, with energy as a function of frequency or wavelength (Fig. 2.3).

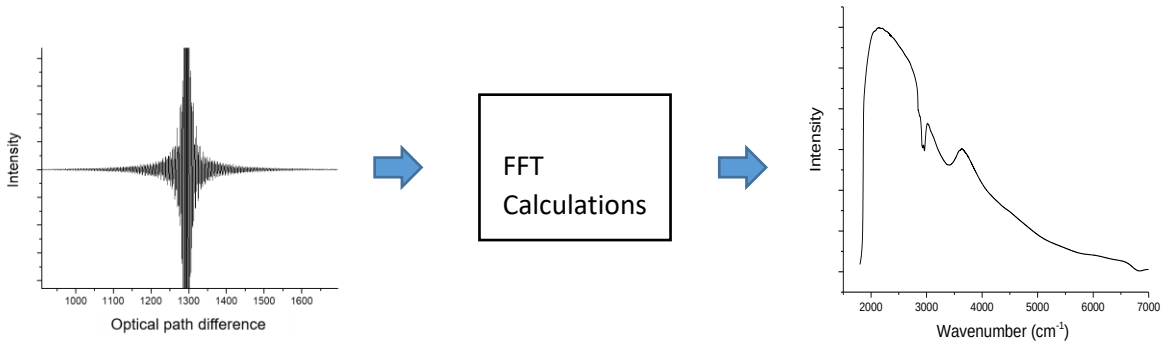

Figure 2.3: An interferogram is converted into a transmission spectrum via computer using fast Fourier transformation calculations.

The FFT calculations are described here following the derivation given in chapter 9 of McCluskey and Haller.[7] For a broadband source of IR light, the intensity seen by the detector can be given by an integral over all wavelengths, written:

$$I \propto \int_0^\infty E_0(k)^2 dk + \int_0^\infty E_0(k)^2 \cos(k\delta)\, dk \tag{2.1}$$

where the second term is the interferogram and can be written as a Fourier transform of the spectrum $I_0(k)$:

$$I(\delta) = \int_0^\infty I_0(k) \cos(k\delta)\, dk \tag{2.2}$$

To obtain our normal spectrum, we perform an inverse Fourier transform:

$$I_0(k) \propto \int_0^\infty I(\delta)\cos(k\delta)\,d\delta \tag{2.3}$$

The computer uses what is known as a fast Fourier transform (FFT) algorithm to evaluate this integral.

The material's optical properties can then be studied based on what light is transmitted. The absorbance (*A*) of a signal can be calculated from the transmission with equation 2.4:

$$A = -log(T), \tag{2.4}$$

where the *T* is simply the ratio of the light that passes through the sample over the light incident on the sample. This can be derived from the Beer-Lambert law discussed in chapter 1.

For all FTIR measurements performed in this work, the spectra were obtained with Bomem DA8 FTIR spectrometer (Fig. 2.4). The source was a silicon carbide globar that emits blackbody radiation between 200 and 4000 cm^{-1}. This source is split by a potassium bromide (KBr) beamsplitter. The detector used is a liquid nitrogen-cooled indium antimonide (InSb) detector with a range of 1800-7000 cm^{-1}. The system contains both a room temperature sample compartment and a cryostat helium cooled to as low as 9 K. Because water and carbon dioxide strongly absorb in the mid IR, both low temperature and room temperature measurements require vacuum to obtain a good absorption spectrum from a sample in that range. For this body of work, all FTIR measurements were performed at ~10 K unless specified otherwise.

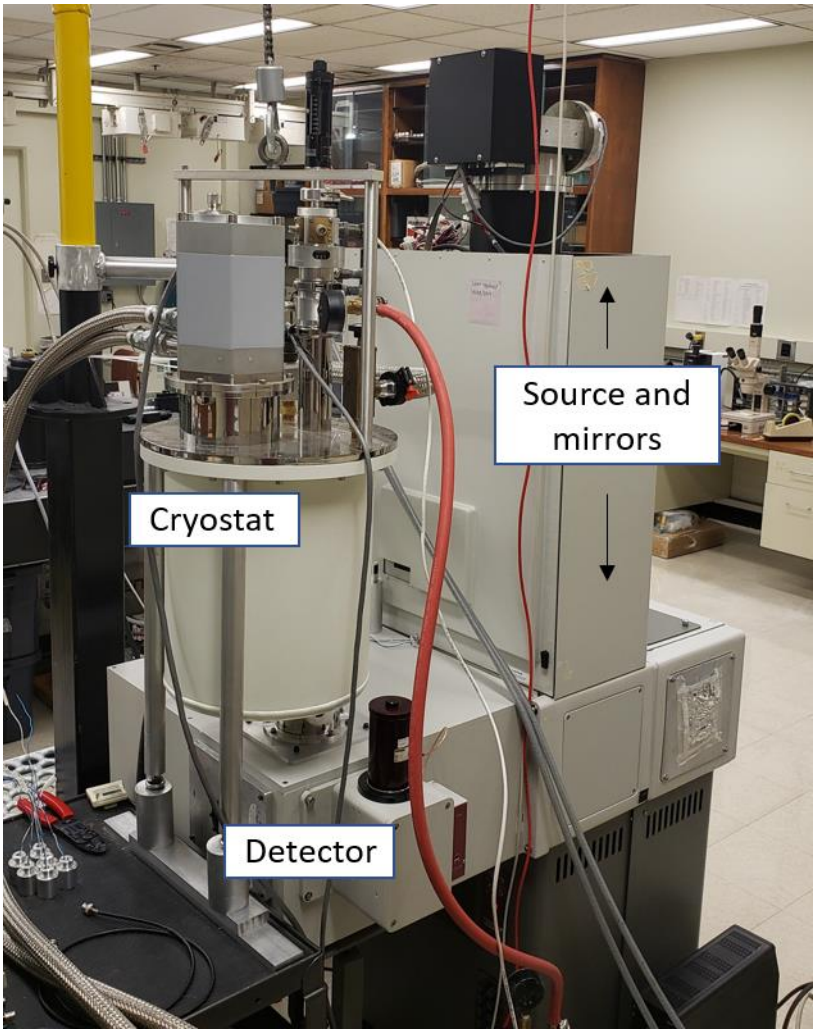

Figure 2.4: Image of the Bomem DA8 FTIR low temperature setup.

2.2: Photoluminescence (PL) and photoluminescence excitation (PLE) spectroscopy

When a molecule absorbs photons, some of its electrons are excited to a higher electronic state. Then, in many circumstances, the molecule radiates a new photon as the electron returns to a lower state by a process known as photoluminescence. Photoluminescence spectroscopy is the technique that involves stimulating this process and measuring the resultant emission to learn more about the defects and properties of the material being studied. In PL, a fixed photon source

is directed onto the sample in question, and the emitted light is passed through a scanning monochromator and into a detector like a photomultiplier tube (PMT). The resulting spectrum gives luminescence intensity in counts as a function of wavelength or energy. Figure 2.5 gives an example of a PL spectrum for luminescing pyrene excited by a 325 nm source. The sample emits more or less strongly depending on the excitation wavelength applied, and the resulting spectrum is unique to the material or defects being studied.

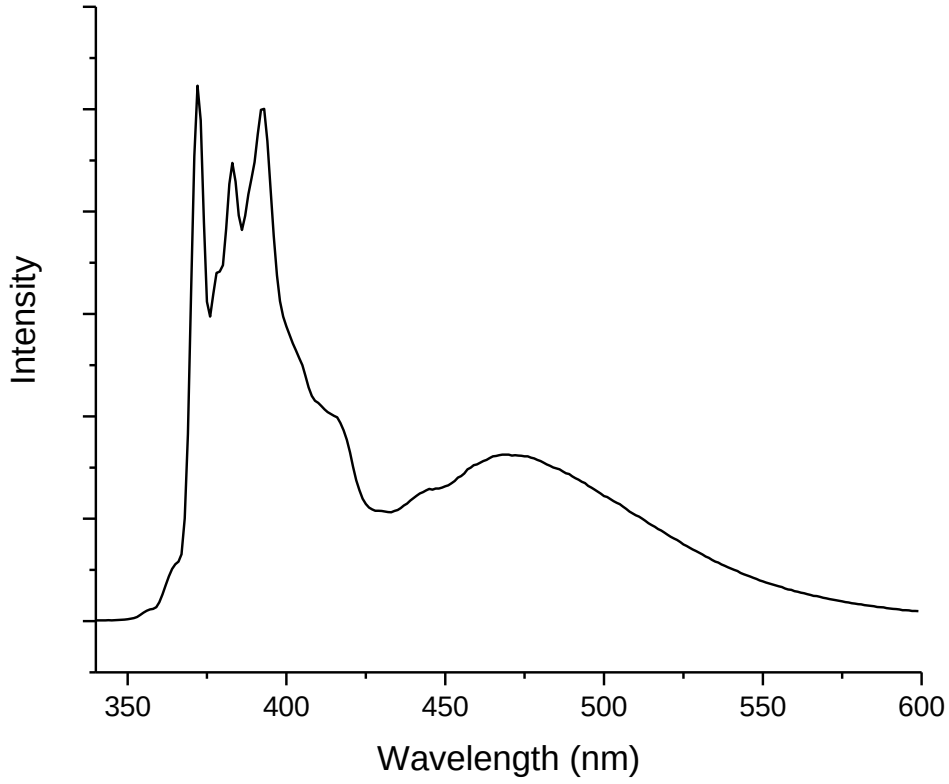

Figure 2.5: 325 nm PL excitation of pyrene dissolved in alcohol.

Photoluminescence excitation (PLE) is a technique that uses the same physical process but measures in a different way to gather different information about the sample. While the PL technique uses a fixed source and a monochromator to control the light reaching the detector,

PLE uses a monochromator grating to vary the source wavelength. The detector then only measures a single specific wavelength of the emission. PL is often performed with a laser source, but PLE requires a broadband source in order to be able to scan across the excitation range. Figure 2.6 gives an example of PLE for the pyrene in figure 2.5. The emission wavelength has been fixed on the largest peak of the pyrene monomer emission at 373 nm, while the source is varied from 240 to 360 nm. This demonstrates that in this range the 373 nm peak is most excited by the peaks seen in the spectrum, which can be helpful for choosing a better excitation source to observe the peak. This also gives information on the absorption of the sample, as the absorption process is where the energy needed to excite the photons is acquired.

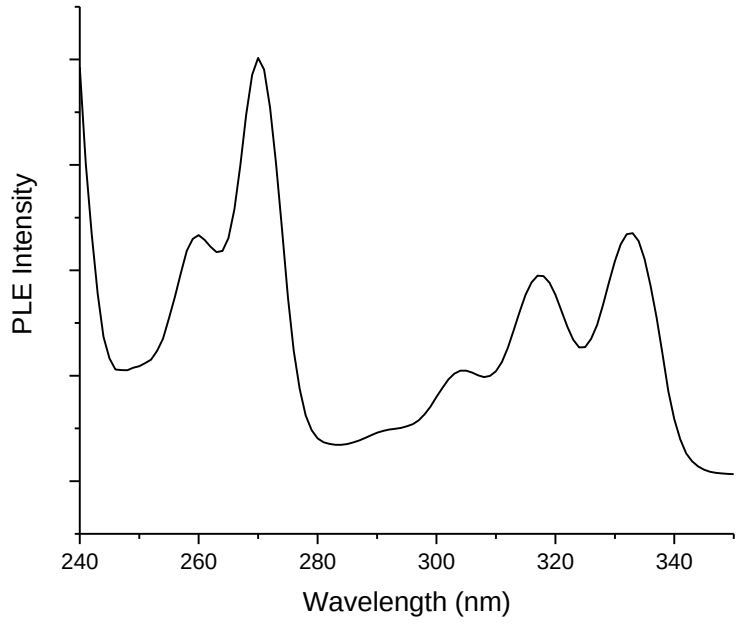

Figure 2.6: PLE spectrum for emission of the 373 nm peak in figure 2.5.

The PL and PLE measurements in this work were performed on a JY-Horiba FluoroLog 3-22 spectrometer. The excitation source is a 450 W xenon lamp with a range of 240-600 nm. The detector used is a room temperature R928P PMT. Double-grating monochromators are present for both excitation and emission. A diagram of the optics involved can be seen in figure 2.7 below.

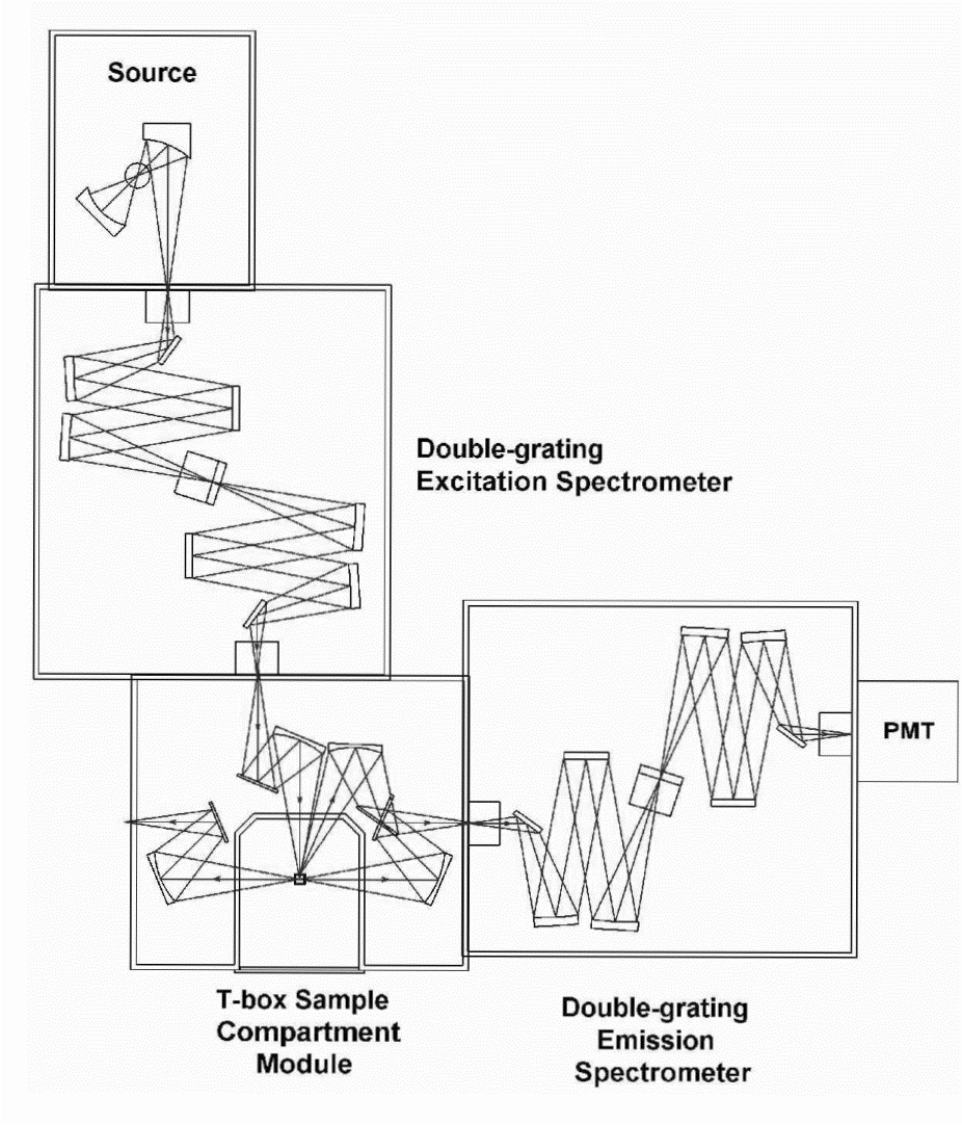

Figure 2.7: Horiba schematic for the optics of the Fluorolog 3-22.

2.3: Raman spectroscopy

Raman spectroscopy is an optical spectroscopy technique used to investigate the low-frequency modes of a material, like the vibrational modes of defects in a semiconductor. The process, called *Raman scattering*, is the inelastic scattering of light off the molecules of the sample. This covers cases both where the incoming photon loses energy by exciting a vibrational mode, called *Stokes* Raman scattering, or when the photon gains energy thermally, referred to as *anti-Stokes*.[7]

The setup for Raman spectroscopy is at the most basic level very similar to that of a PL experiment. It is often possible to acquire both spectra on the same system. A simplified diagram can be seen in figure 2.8. The excitation source (laser, monochromator filtered lamp, etc.) passes through a beam splitter and strikes the sample, exciting inelastically scattered photons. The scattered light, containing the vibrational information of the sample, passes back through the beam splitter and into a monochromator and detector, where the intensity can be plotted as a function of energy to convey vibrational modes. Because the energies observed in Raman are so low, a notch filter is placed between the splitter and the detector to block the excitation wavelength but allow nearby wavelengths.

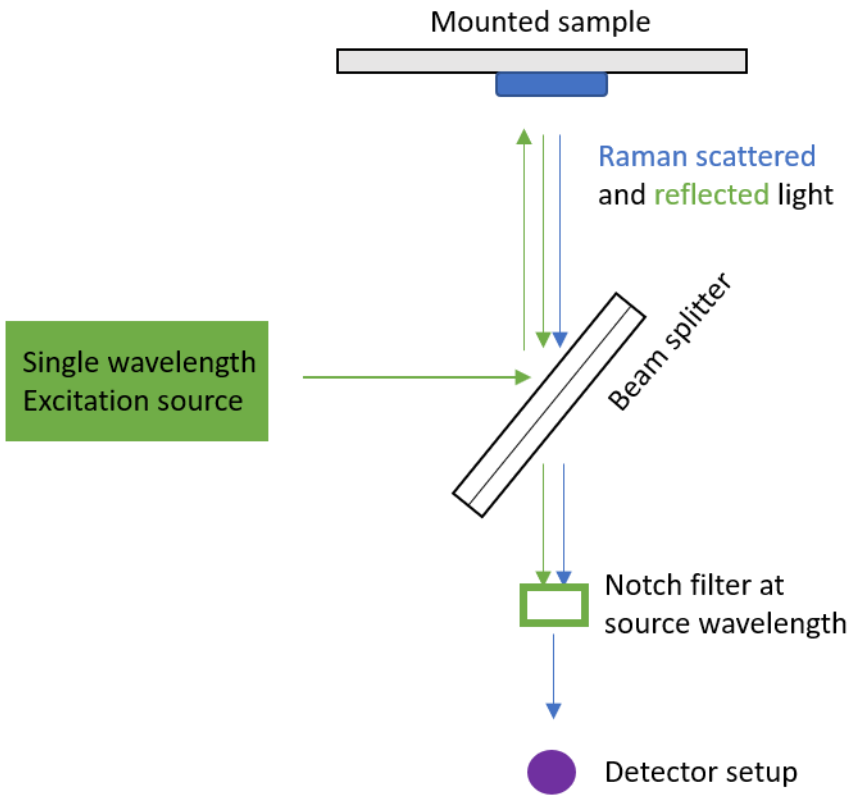

Figure 2.8: Generalized diagram of a basic Raman scattering setup.

While in practice both Raman and PL can be detected with the same setup, a Raman signal is much lower intensity when compared to the PL of any strongly luminescing sample. Figure 2.9 shows an example of Raman scattering for an MgZnO thin film where the Raman signal is present but swamped by the underlying PL signal of the material. One way to increase the strength of a Raman signal is through resonance. *Resonant* Raman is Raman scattering where the excitation wavelength is chosen to overlap with an electronic transition like UV absorption in the material being probed.

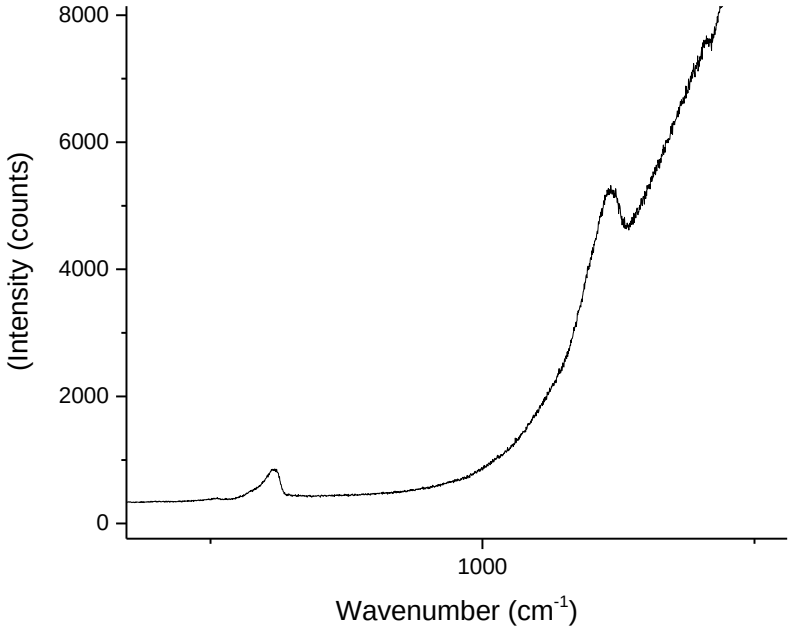

Figure 2.9: Raman signal for a MgZnO thin film. The Raman peaks are present, but the underlying PL is a much stronger process which can be inconvenient when it swamps the Raman.

2.4: UV/Vis spectroscopy

UV/Vis spectroscopy refers to absorption measurements taken in the ultraviolet and visible spectral regions. Light from a UV/visible wavelength source passes through a monochromator, strikes the sample, and the transmitted or reflected light is measured. The absorbed light, and therefore the transmitted light, is unique to the structure and defects of the sample. One of the most fundamental absorptions in a semiconductor is the energy needed to excite electrons from the valence band to the conduction band. In this, UV/Vis is a useful tool for observing the optical band gap of a material. As an example, diamond is experimentally known to have an indirect band gap of 5.47 eV.[31] Figure 2.10 shows a transmission spectrum

taken for optically pure diamond with an absorption threshold at ~5.5 eV. Other features of the absorption spectra can tell you more about a wide range of defects a material could contain.

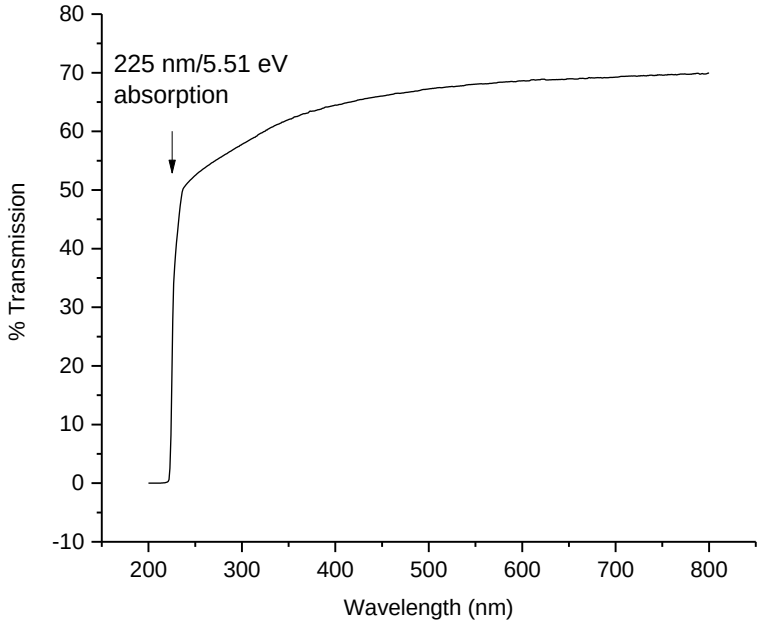

Figure 2.10: UV/Vis transmission spectrum of band-gap absorption in optically pure diamond.

UV/visible transmission spectra in our lab are collected using a Perkin Elmer Lambda 900 Series UV/VIS/NIR Spectrometer with a deuterium lamp source (Fig 2.11). All UV/visible transmission spectra were taken at room temperature.

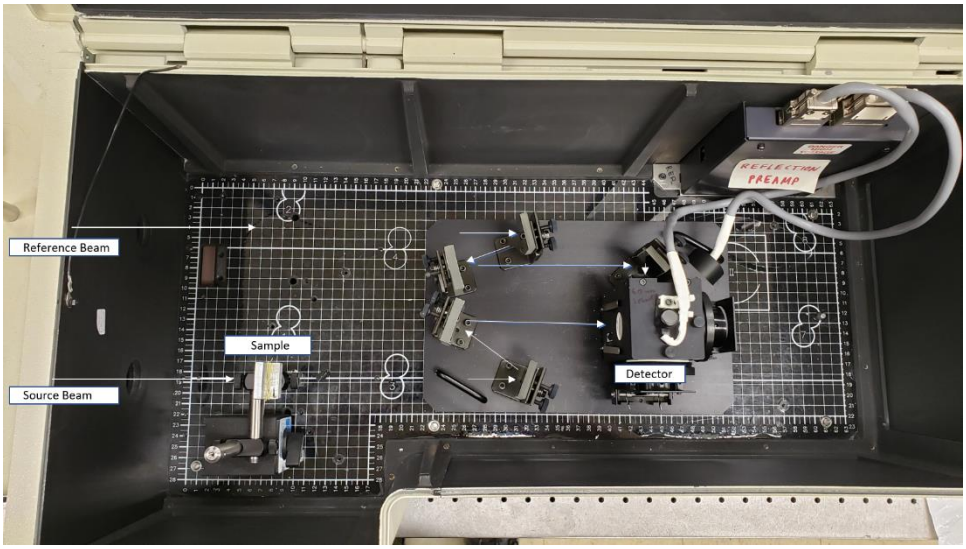

Figure 2.11: Picture of the Perkin Elmer Lambda UV/Vis system used in our experiments.

2.5: X-ray diffraction

X-ray diffraction (XRD) is a non-destructive tool used to analyze the structure of a crystal. Specifically, XRD is the scattering of x-rays by the atoms of a periodic lattice. Because crystals are structured such that interatomic distances within them are on the order of fractions of nm, irradiating semiconductors with x-rays with energy roughly equal to the atomic spacings will result in x-ray diffraction. When the x-rays scatter from the atoms at that scale at different layers of the crystal lattice, interference occurs. From the geometry of figure 2.12, where λ is the x-ray

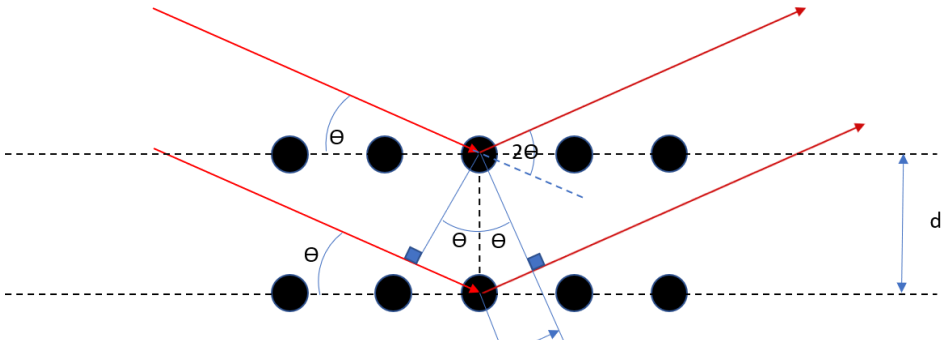

Figure 2.12: X-ray scattering geometry showing Bragg's law.

wavelength, d is the spacing between the planes, and Θ is the angle of incidence and reflection, the lower beam travels an extra 2d·sin(Θ).

Constructive interference occurs when that distance is an integer multiple of the x-ray wavelength. This condition is referred to as *Bragg's Law*:

$$n\lambda = 2d\ sin\theta. \tag{2.5}$$

Because the x-ray is incident at an angle Θ and also reflects at an angle Θ, the angle between the x-ray and the detector is 2Θ. This angle is the convention for measuring XRD peaks. When scanning along a range of angles, the sample will only diffract when the Bragg condition is met. By comparing this to known material databases, the resultant intensity vs. 2Θ spectrum can be used to identify the composition of unknown materials or used to identify the phase or orientation of single crystals. For example, a sample with a (100) oriented surface will diffract at different 2Θ values than a sample with a (010) surface. Gallium oxide in the beta-phase will have a different structure than the alpha-phase, and so diffract differently. An amorphously grown sample might have no diffraction patterns, while a randomly oriented powder will have many, often displayed in a ring format. An example of a single crystal (100) Ga_2O_3 2Θ graph is shown in figure 2.13. The diffraction patterns appear at specific orientations and are matched to a database to confirm that the surface we are viewing is in fact the (100) surface. Because the only planes that appear are the (400), (600), and (800), which are all multiples of the (100) plane, we can know our orientation.

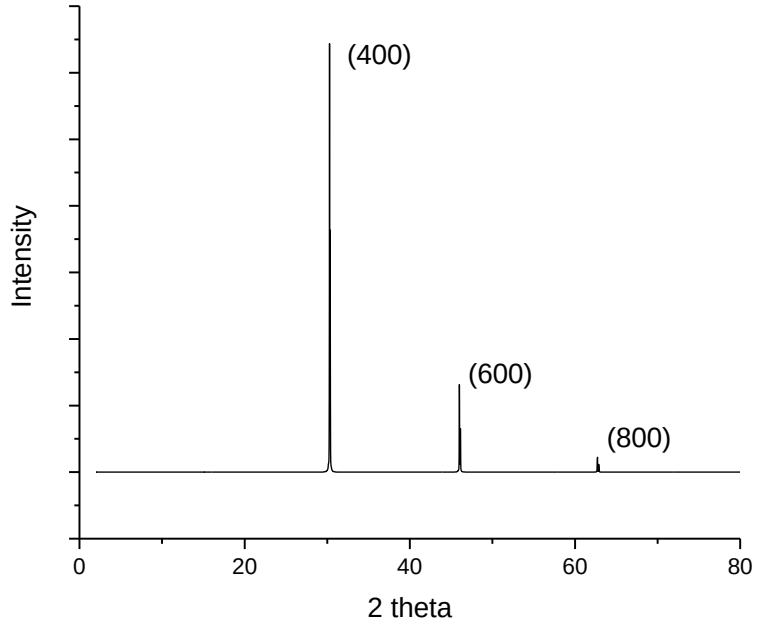

Figure 2.13: XRD of the (100) surface of a single crystal Ga_2O_3 sample. The diffraction peaks are compared against a database to help assign an orientation to the crystal.

All XRD spectra taken in this work were performed on the University of Idaho's XRD system at the U of I center for microscopy.

2.6: Other applicable techniques

The experimental techniques described here in brief are used in this body of work, but not within the resources of our lab. Often this involves sending a sample to another group or corporation for analysis.

2.6.1: Secondary ion mass spectrometry (SIMS)

SIMS is a destructive process used to analyze the atomic composition of a sample. When a solid sample is sputtered by primary ions of enough energy, some fraction of the particles

emitted from the sputtering are ionized. These secondary ions are analyzed with a mass spectrometer and contain information about the makeup of the target. SIMS is advantageous because it is the most sensitive elemental surface analysis technique, but it is also both complicated and expensive.

All SIMS analysis performed in this work was done by the Evans Analytical Group

2.6.2: X-ray photoelectron spectroscopy (XPS)

XPS is another surface analysis technique for quantitative atomic composition. The sample is irradiated with monochromatic x-rays, and the resulting electron emission contains energies characteristic to the material being sampled.

2.6.3: Rutherford backscattering spectrometry (RBS)

RBS is a technique useful for analyzing the elemental makeup and crystalline quality of a thin film. High energy alpha particles (He^{2+}) are scattered off the sample at an angle and then the backscattered energies are measured. The composition is gathered from this because each element has its own known backscattering cross section and profile dependent on the mass of the target atom.

CHAPTER THREE: SEMICONDUCTOR GROWTH

3.1: Bulk crystals vs. thin films

Just as there are many widely varied uses of semiconductors in modern research and technology, there are many techniques to grow a semiconducting material. No technique is without drawbacks, and for any given need there may be multiple growth methods available to meet it. This chapter will detail some of the most widespread approaches to crystal growth, including but not limited to the methods of growth for all the samples studied in this body of work.

Semiconductor growth can be divided into two types based on the volume and structure of the material produced. *Thin films* are semiconductors grown in a thin layer, usually on top of another material known as a *substrate*. Generally speaking, thin films can be as thick as tens of microns and as thin as a single molecular layer of a material, on the order of a nanometer.[32] Thin films can be grown to create devices, or to change or improve upon some quality of a bulk material's surface. *Bulk crystals* are, as the name suggests, grown in large quantities. These crystals are used actively in devices made from slices of bulk-grown material and passively as substrates for thin film devices.

For both thin films and bulk crystals, single crystal material is usually preferable to polycrystalline or amorphous equivalents. As such, many of the techniques covered in this chapter aim to grow as close to single crystals as possible. Each have their own strengths and weaknesses, including cost and speed of growth, size constraints, and quality of crystal structure.

3.2: Bulk crystal methods

3.2.1: Czochralski process (CZ growth)

The most common way to grow pure semiconducting materials is to do so using a *melt* growth technique. In any of these processes a melt, or liquid quantity of the material intended, is cooled in any number of ways until it solidifies into the intended crystal. The Czochralski (CZ) process is a fast growth method that is heavily used for semiconductors for optical and computing applications.[33] The largest use is for silicon, but at least 100 different materials are commercially grown using the CZ method. Additionally, the gallium oxide (Ga_2O_3) materials in this dissertation were CZ grown by the Institute for Materials Research at WSU, so this technique is of particular import to this work.

Some of the primary advantages of CZ growth are that it is fast, well understood, and produces the nearest to perfect and homogenous crystals. The downsides are that CZ is more expensive than many other growth techniques and can really only be easily applied to materials that melt fairly *congruently*.[34] Congruent melting is when the liquid and solid forms of a material stay compositionally the same while the sample melts.

The setup for CZ growth is fairly simple. The growth starts with a quantity of the basic material the crystal is going to be grown from, known as the *charge*. The solid charge is placed in the *crucible*, where it is heated to above the melting point. One of the limitations for crucible growth is that the crucible must be compatible with the melt being used. Then a *seed crystal*, a small, already perfect crystal of the same material with the desired orientation, is lowered to the surface of the melt on the end of a rotating rod. When the seed begins to melt, it is slowly pulled from the crucible. As the melted material pulls from the liquid, it cools into a solid. If the rod is

pulled/rotated at an appropriate rate, the freezing melt aligns with the structure of the seed crystal, extending the already existing lattice. The melt temperature is reduced, which increases the diameter of the pulled crystal as it freezes more quickly. Once the material is pulling at the desired diameter, it can simply be pulled at a controlled rate and temperature until the desired length is also reached. Then the crystal is cut off by pulling it out of the melt entirely or increasing the melt temperature until the crystal diameter becomes zero. A diagram of the CZ technique is shown in Fig. 3.1.

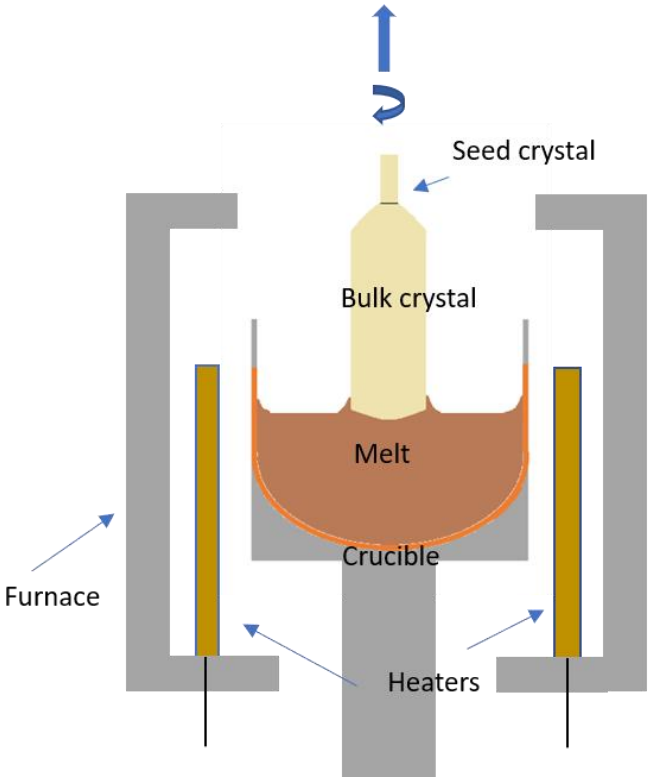

Figure 3.1: Diagram of CZ crystal growth.

For silicon growth the most common crucible material is silica, which over time dissolves into the melt and causes certain issues that must be managed. For oxide crystal growth higher temperatures are required, so precious metal crucibles like platinum or iridium are used. Growth

rates are typically a few mm per hour, so growths can last days to weeks. On the commercial scale, crystals are being grown with a 450 mm diameter from up to a 300 kg melt.[33] The Ga_2O_3 crystals studied in this work were grown on a much smaller scale than that. Fig. 3.2 shows a picture from the WSU lab of Ga_2O_3 being CZ grown taken through the viewport of the active furnace. The image shows the seed crystal attached to the top of the growing crystal being pulled from the melt.

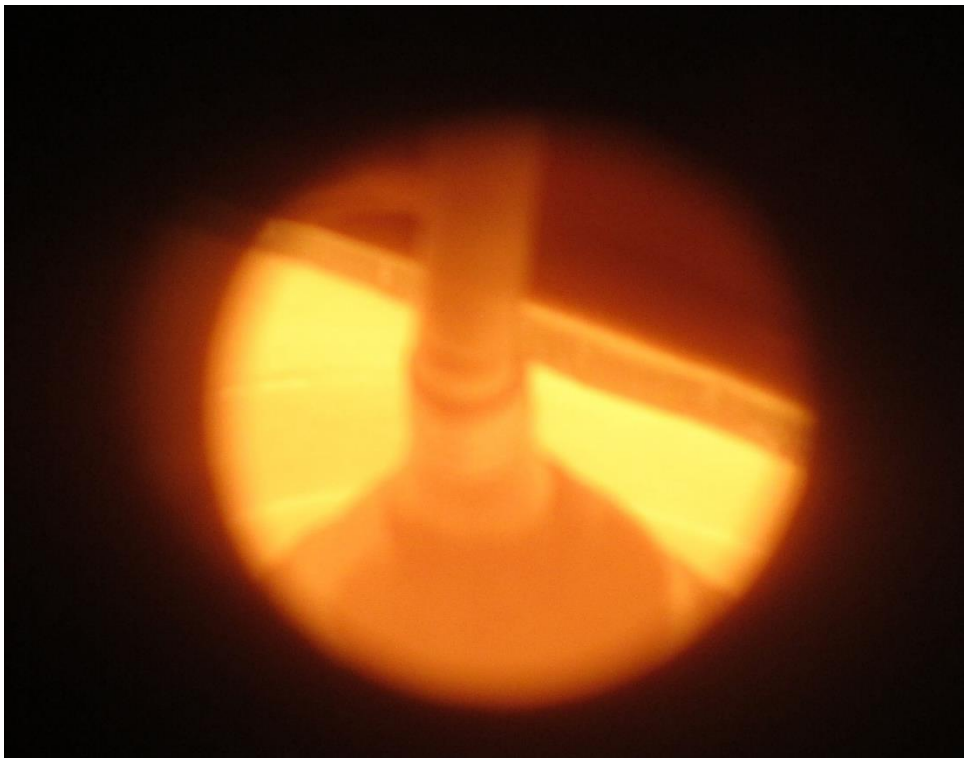

Figure 3.2: CZ growth of Ga_2O_3 being pulled in the WSU IMR furnace.

3.2.2: Verneuil growth

In addition to still having some practical applications today, Verneuil growth is historically significant for its role as the first technique to produce usable crystals on a large scale. Verneuil announced his flame-fusion process in 1902 as a way to create gem rubies.

Today, the Verneuil process is still relevant in its use to grow a number of materials with very high melting points, but the most common use is still sapphire (Al_2O_3), which can be doped to produce ruby. [33]

Fig. 3.3 shows a diagram of the Verneuil flame fusion setup. The powder charge is placed in a hopper at the top and vibrated to sift down over the oxy-hydrogen flame at a controlled rate. As it passes through the flame, the powder melts, and forms the melt surface on the seed below. The seed is rotated and lowered as the crystal grows, so a solid crystal forms but there is always a new liquid film on the top.

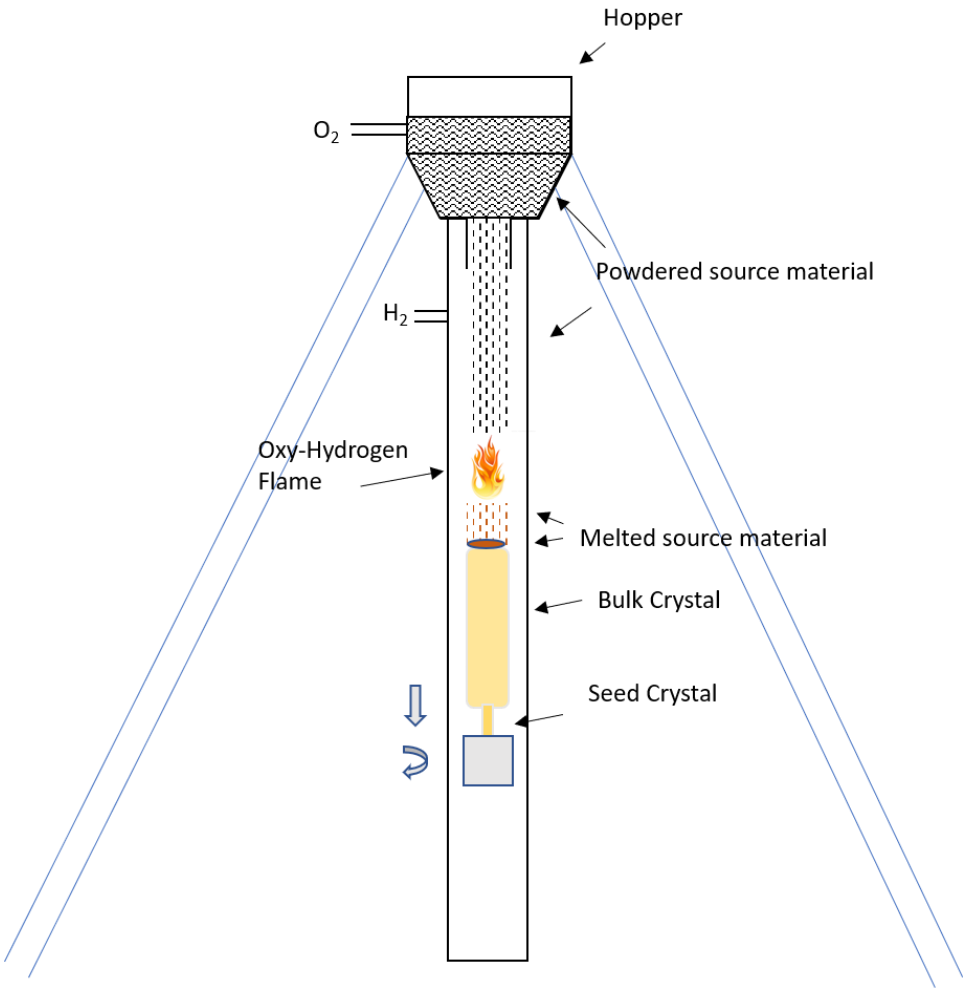

Figure 3.3: Simplified diagram of Verneuil flame fusion. Source material is typically Al_2O_3 for sapphire or ruby production.

One of the major drawbacks of this technique is that it creates a high concentration of *dislocation* defects. A dislocation defect is a line of atoms that are out of position within the crystal structure, a result of the imprecise nature of the way material is added to the crystal in this case. An upside is that the process uses no crucible, allowing it to avoid contamination and reach temperatures higher than most favorable crucible materials allow.

3.2.3: Float zone

Float zone crystal growth is a newer type of growth that also has the advantage of not using a crucible. A rod of polycrystalline material is placed against a pure single-crystal seed, as shown in Fig. 3.4. The entire production takes place under vacuum or in an inert gas. Then, a heating coil melts the seed and end of the polycrystalline rod. As the material melts, the heated zone inside is moved along the rod, melting the polycrystalline material and leaving a single crystal rod behind. Once the melted zone has traversed the entire length of the rod, all of the rod beneath the coil is then a single crystal. Because of the tendency for many impurities to prefer the melt to crystallization, this method is also used as a purification process, as those impurities can be swept to the end of the crystal.

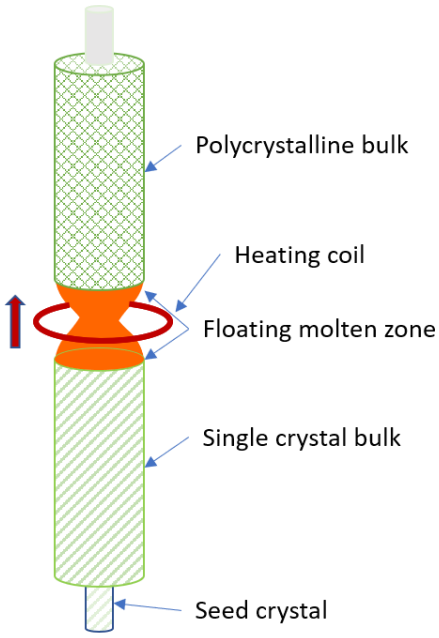

Figure 3.4: Diagram of the float zone crystal growth method.

The major problem with float zone crystal growth is that keeping the crystal from collapsing under its own weight around the melt constrains the size of crystal that can be grown.

The larger the crystal the greater the complications involved. The only material grown in large scale with float zone is silicon. The other common use is for high-purity, small crystal growth. There have been reports of successful β-Ga_2O_3 growth using the float zone technique.[21]

3.2.4: Edge-defined film-fed growth

In edge-defined film-fed growth (EFG), a die with a central slit is placed on the surface of a melt in a crucible (Fig. 3.5). Like the crucible itself, the die must be a material that is compatible with the material being grown, for similar reasons. Surface tension forces the melt up the slit through capillary action, and at the top of the slit a seed crystal meets the melt. The seed crystal is then pulled upward. Crystal quality suffers, but various shapes of crystals like tubes or sheets can be created depending on the die chosen. Although none of the materials in this body of work were grown with EFG, this method is discussed here for having recently been of use growing high quality gallium oxide samples.[22]

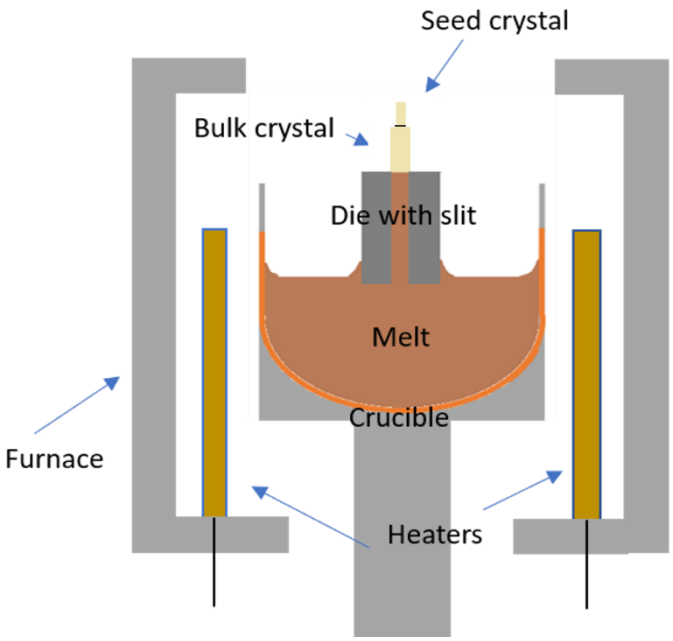

Figure 3.5: Diagram of edge-defined film-fed growth.

3.2.5: Bridgman growth

The Bridgman technique is another crucible melt growth, although it is simple enough that sometimes just an ampoule in a furnace is used. A seed crystal is placed at one end of the melt, then starting with the seeded side the entire crucible is gradually moved within the furnace to cooler temperatures (Fig. 3.6). The melt is frozen progressively from one end to the other. Benefits of this method include simplicity of implementation and good dimensional control. The major drawback is that the growing crystal remains in contact with the surface of the crucible as it cools, which can lead to impurity and strain problems.

The bulk ZnS samples used for pyrene substrates in chapter 7 and for comparison to ZnSO thin films in chapter 6 were commercially grown using the Bridgman method.

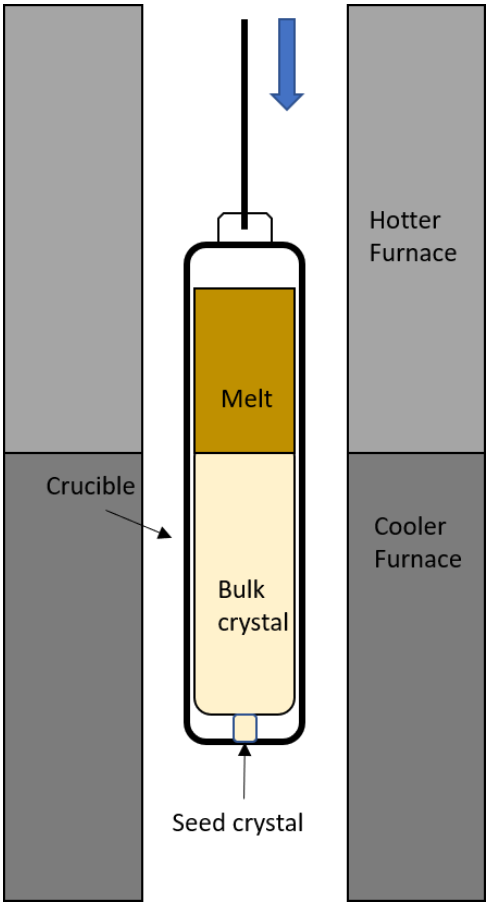

Figure 3.6: Diagram of Bridgman crystal growth.

3.3: Thin films

3.3.1: Physical vapor deposition (PVD) methods

Physical vapor deposition (PVD) is a general term used to describe the thin film creation process where vaporized solid material condenses on the surface of a substrate under partial vacuum. Every PVD technique needs 3 things to happen: the vapor-phase species must be created, it must be transported from the source to the substrate, and the transported atom or molecule must nucleate on the substrate and grow as a film. [32] These conditions can be met in

many ways, and so there are many types of PVD growth. In this work, two in particular are used in our experiments, sputtering and evaporation.

3.3.1.a: Sputtering

In a sputtering system, an anode and cathode are situated across the vacuum chamber from each other. A substrate to receive material is placed on the positively charged cathode, and a material to be sputtered is placed on the negatively charged cathode. Vacuum is pulled on the chamber, and then a *working gas* like argon is introduced. When an electric field is applied across the anode and cathode, the working gas is ionized, forming a plasma. The plasma strikes the target, aimed by the electric field, and knocks ions of the sputtering material off the target. Those atoms then travel to the substrate where they are deposited and form a thin coat of the target material. For a conductive target, a direct current (DC) power source is used. However, because an insulating (or semi-insulating) target cannot dissipate the current, charge will build up that eventually repels the plasma and sputtering cannot continue. To get around this, radio frequency (RF) sputtering is used instead, where the applied electric field is alternating. This results in half the rate of sputtering but is necessary for non-conductive materials.

Any sputtering performed in this body of work was performed on the Bergman lab sputtering system at the University of Idaho (Fig. 3.7). All of the sputtering performed for ZnSO alloys in chapter 6 were performed with RF sputtering.

Figure 3.7: Sputtering system in the Bergman lab at University of Idaho.

3.3.1.b: Evaporation

Thermal and vacuum evaporation are some of the simplest forms of PVD. The source material is vaporized by exposing it to a very high temperature, vacuum levels comparable to its partial vapor pressure, or both at once. The vaporized material is then transmitted through vacuum, where it condenses on the substrate.

The simplicity of the process leads to many variations on specific setups. The vacuum atmosphere transport has the added benefit of reducing contaminants but is mostly limited to a straight-line trajectory from source to sample.

Chapter 7 discusses pyrene deposited in a vacuum evaporation setup performed in an exceedingly simple variation. The pyrene molecule is partially vaporized from a powder source from vacuum pressure alone, and deposits on every surface of the chamber, including the desired substrate. The resulting deposition is a single layer of pyrene molecule, but longer exposure,

stronger vacuum, or added thermal conditions are all parameters that could have resulted in something approximating a more substantial film.

3.3.2: Chemical vapor deposition (CVD)

Chemical vapor deposition (CVD) is the general term for the creation of a thin film using chemical reactions. The material in the vapor phase reacts to a chemical process at the surface of the intended substrate and from this reaction a thin film is grown. Vapor phase epitaxy (VPE) is a widely used form of CVD in the electronics industry for the growth of semiconductors on silicon substrates.[35] A subset of VPE, metal-organic chemical vapor deposition (MOCVD), is relevant to this work in its applications in the growth of good III-V and II-VI compound semiconductors. Both VPE and MOCVD are detailed below.

3.3.2.a: Vapor phase epitaxy (VPE)

In VPE, epitaxial growth is achieved when gas molecules deliver atoms to the substrate. Reactant gases, or *precursors*, are pumped into the reaction chamber. When they reach the substrate surface, if the right conditions are present they react together or with the substrate material. The desired products of the reaction are deposited/adsorbed onto the surface. On the surface, further reactions or diffusion can serve to bring the atoms to their appropriate lattice sites as the film grows. The by-products of the gas reactions then desorb off the substrate and growing film. Then through convection and diffusion the by-products are carried away from the reaction zone.

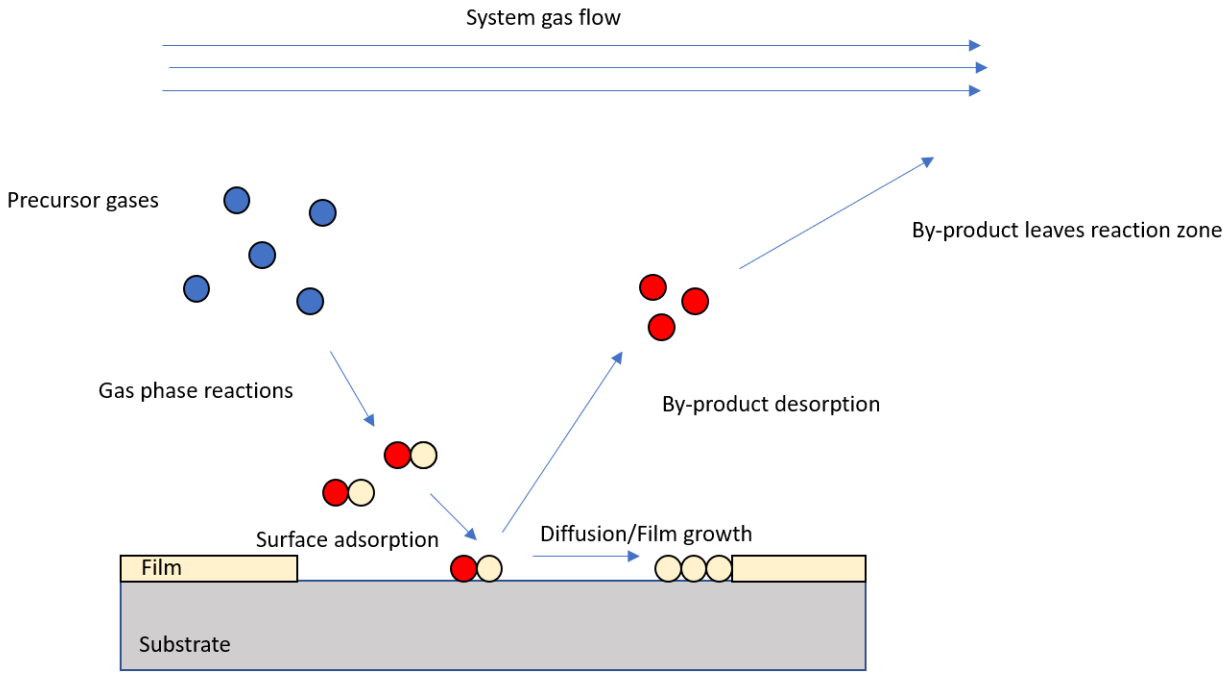

Figure 3.8: Simplified depiction of the steps in VPE growth.

CVD growth yields several tangible advantages. The precision of instrumentation makes it such that very fine control is achievable for many of the variables involved. It is useful for producing high quality uniform films for a wide range of compounds. Finally, the flow rates the precursors can be subjected to can lead to much faster deposition than PVD processes.

No growth system is perfect, however. Some of the disadvantages of CVD make PVD a better choice for many applications. CVD application temperatures, while much lower than bulk melt growth temperatures, can be over 1000°C, which might be too high when working with devices that are already on substrates. Also, many of the precursors involved in CVD can be both toxic and expensive, either of which are always a complication in an experiment.

3.3.2.b: Metal-organic chemical vapor deposition (MOCVD)

Metal-organic chemical vapor deposition (MOCVD) is also known as metal-organic vapor phase epitaxy (MOVPE). Despite the more complicated naming scheme, MOCVD is no more complicated than the VPE process already described, just more specific. In MOCVD, at least one precursor is *metal-organic*, which means compounds that contain both organic and metal ligands. These precursors are often in the liquid phase and introduced to the reactor by way of a carrier gas blown through a bubbler. The carrier gases are most commonly hydrogen (H_2) or nitrogen (N_2), but vary based on the material being grown. Because of the metals used, the products are most commonly type III-V semiconductors, although some II-VI materials are grown as well.

3.3.3: Thermal oxidation

Thermal oxidation is a chemical process primarily applied to silicon in which exposure to an oxygen atmosphere forms a layer of silicon dioxide (SiO_2) on the surface. This process occurs naturally on pure silicon even at room temperature in ambient air. The natural SiO_2 layer grows to about 1-2 nm thick because oxygen atoms don't have the energy to diffuse through the formed oxide layer at room temperature.

For deliberate oxidation, Si wafers are heated in a furnace around 1000° C while exposed to an oxygen heavy environment. When the environment is pure O_2 this is called *dry* thermal oxidation.[34] Another approach is to use water vapor as the oxidant. This produces *wet* thermal oxide. Dry thermal oxidation grows better quality SiO_2 but wet thermal oxidation grows the material much faster and thicker. Because of this, dry thermal oxide is often used in actual devices while wet thermal oxide is often used in a masking role for its easy insulating properties.

SiO_2 layers are used as both an insulator in devices and to mask against unwanted dopants. SiO_2 layers can be grown by deposition methods when thermal oxidation not an option, like cases where the wafer has thermal restrictions. Chapter 7 describes our experiment in which thermal oxide thin films are used as a substrate for another deposition.

CHAPTER FOUR: GALLIUM OXIDE

4.1: Publications

The information presented in this chapter has been published across several papers.

- "Compensation and Hydrogen Passivation of Magnesium acceptors in β-Ga_2O_3",
  J.R. Ritter, J. Huso, P.T. Dickens, J.B. Varley, K.G. Lynn, and M.D. McCluskey,
  Appl. Phys. Lett. **113**, 052101 (2018)
- "Hydrogen Passivation of Calcium and Magnesium Doped β-Ga_2O_3",
  J.R. Ritter, K.G. Lynn, and M.D. McCluskey,
  Proc SPIE 10919 (2019), https://doi.org/10.1117/12.2507187
- "Iridium-related complexes in Czochralski-grown β-Ga_2O_3",
  J.R. Ritter, K.G. Lynn, and M.D. McCluskey,
  J. Appl. Phys. (submitted)

Sections of the growth descriptions were written by Peter Dickens who grew the gallium oxide samples while working for the Institute for Materials Research at WSU. Joel Varley at Lawrence Livermore National Laboratory performed the calculations on Mg and Ir levels in gallium oxide and authored parts of the corresponding section reporting the results.

4.2: Material growth

Gallium oxide can be grown and synthesized with a wide range of techniques. Films can be sputtered, sublimated, deposited with chemical vapor deposition (CVD)[36] or molecular beam epitaxy (MBE),[37] or many other varied approaches.[12] As with most semiconducting materials, the most effective and most common approach for growing gallium oxide single crystals in bulk

is via the assorted methods of melt growth. Ga_2O_3 melts congruently at just over 1800 ºC,[12] and begins to show signs of decomposition into volatile oxides around 1200 ºC.[38] The liquid gallium metal that results from this decomposition is corrosive to most metals, and these decomposition effects are suppressed by adjustments made to the atmosphere of the growth.[21] For melt techniques that use a crucible, the corrosive nature of the melt and extremely high temperatures required greatly limit the material that can be used as a crucible. To this end, the crucible used for gallium oxide growth is almost always made of iridium. It is worth noting that crucible-free melt growth techniques exist; for example, float zone growth has been used to grow Ga_2O_3 single crystals.[21,37,39] However, all the gallium oxide grown and tested in this body of work was performed via crucible melt growth.

Ga_2O_3 boules were grown for our experiments by the Kelvin Lynn group with the Institute for Materials Research at WSU. The crystals were grown using the Czochralski (CZ) method described in chapter 3. The doping concentrations, pulling rate, and growth atmosphere are listed in Table 4.1. High purity powder of gallium oxide (99.999%) from GFI Advanced Technologies, Inc. was used for the raw material. The raw material and dopants were weighed with 10 mg precision (adjusting for inherent moisture content within the powders) to a target weight of 500 g, then ball milled using high purity (99.8%) alumina milling balls for 18 hours. After mixing, the powder was compressed in an isostatic press to ~20 kpsi to make the final charge.

The crystals were grown using an iridium crucible (86 mm Ø x 60 mm tall) with a radio-frequency induction coil operated at 20 kHz frequency. First, the 500 g charge was melted over the course of ~15 h and then cooled. After this, a second charge of 500 g was added to the

crucible to increase the melt volume to 1 kg for improved heat flow and to maintain stable flow patterns during growth.

For the growths, the crucible was generally rotated while the seed was not rotated. Figure 4.1 shows an image of grown Ga_2O_3 still in the iridium crucible. The spiraled shape of the pulled crystal is due to a complication in growth, and not found in every case. Different atmospheres were used for the growth of the boules to minimize gallium oxide evaporation from the melt. None of the used atmospheres eliminated gallium oxide evaporation though the higher content oxygen in nitrogen atmospheres were observed to reduce evaporation the most.

Dopant	**Atmosphere**	**Pressure**	**Seed Holder**	**Crucible Rotation**	**Pulling Rate**
Undoped	50/50 - 5000 ppm O_2 balanced N_2/CO_2	941 Torr	Ir strip	10 rpm	N/A - Kyropulos Style
0.15 at.% Mg	CO_2	941 Torr	Sapphire	6 rpm	3 mm/hr
0.25 at.% Mg	1% O_2 in N_2	870 Torr	Alumina	2 rpm	10 mm/hr

Table 4.1: Growth information for the crystals. Doping amount is with respect to gallium and in the form of the metal oxide.

Figure 4.1: Ga_2O_3 boule still in the iridium crucible.

Figure 4.2: Sample crystal of Mg-doped gallium oxide broken from the larger boule

4.3: Hydrogen and iridium in undoped Ga_2O_3

The role of hydrogen impurities in undoped Ga_2O_3 were studied by H-annealing the as-grown samples. The diffusion was performed by sealing the sample in a silica ampoule filled with ½ atm of hydrogen gas. The ampoule was then annealed in a furnace and water-quenched to room temperature. For these early samples, the annealing took place at 820 ºC for 2 hours. For later samples it was determined that 850 ºC for 3.5 hours was more effective, and all other H and D anneals were performed under these conditions except in cases where direct comparison to the original findings were required.

With hydrogen annealing, four new absorption peaks appeared in the IR at 3314, 3437, 3450, and 3500 cm^{-1} at 10 K (Fig 4.3). These peaks were assigned to O-H bond-stretching vibrational modes from the added interstitial hydrogen. A good test for this effect is to deuterate instead of hydrogenate the samples and look for the peaks to shift due to the change in mass. Sure enough, corresponding deuterium peaks were observed using the same annealing procedure with ½ atm D_2. The observed isotopic frequency ratio between the H and D complexes is ~1.35, in good agreement with O-H and O-D in other semiconductors.[40,41] The peak at 3437 cm^{-1} had been identified previously as a gallium vacancy decorated by two hydrogen atoms ($V_{Ga}2H$) by the Stavola group at Lehigh University.[42] The other three peaks hadn't been previously observed. Initially, we simply suggested they were due to hydrogen complexed with native defects or impurities.

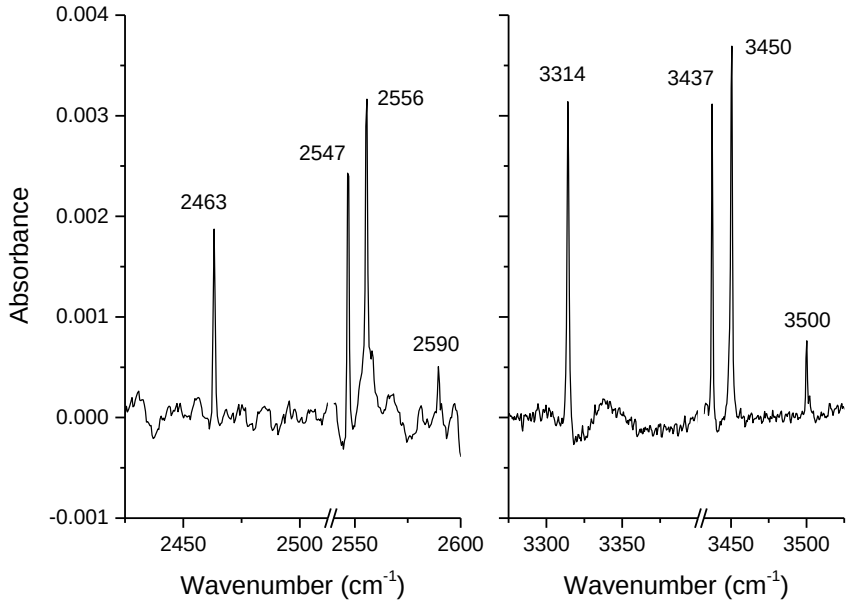

Figure 4.3: IR absorption of hydrogen (right) and deuterium (left) anneals of undoped Ga_2O_3.

Later, when we returned to the original batch of undoped Ga_2O_3 for a completely unrelated reason, we were surprised to discover that hydrogen annealing a sample from the same boule gave a noticeably different result. The $V_{Ga}2H$ peak was the same intensity, but the three unidentified peaks were much smaller (Fig 4.4). Further consultation on the growth conditions revealed that while the samples were broken from the same boule, the sample with the stronger unidentified trio of peaks was taken from closer to the center of the boule, and therefore closer to the iridium seed crystal holder. To confirm that iridium was the culprit, we needed to know the concentration of iridium present in both samples, and so they were sent off for secondary ion mass spectrometry (SIMS).

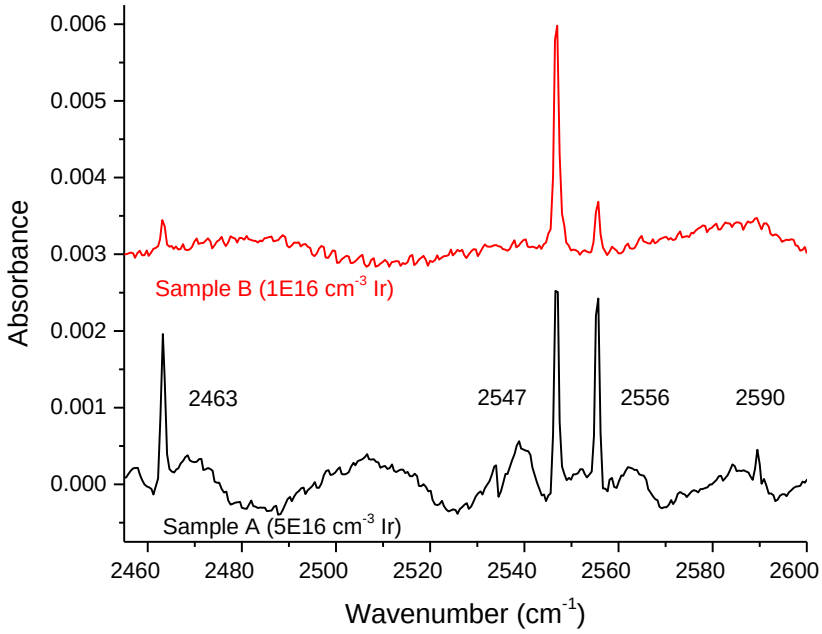

Figure 4.4: IR spectra of two samples of deuterium annealed, undoped gallium oxide. Both samples are from the same boule. Sample A has an Ir concentration roughly 4 times that of Sample B. Spectra are offset for clarity.

Our suspicions about the iridium concentration differences were correct. The crystal with the strong 3450/2456 cm^{-1} peak contained roughly four times more iridium than the sample with the weaker peak (Table 4.2). From this correlation we were able to tentatively assign the 3313, 3450, and 3500 cm^{-1} peaks to O-H stretching modes associated with iridium-hydrogen complexes. Table 4.2 contains a summary of the SIMS findings for all samples collected, both doped and undoped.

	D	Si	Ir	Mg	Ca
Detection limit	8.0×10^{14}	1.0×10^{15}	5.0×10^{15}	5.0×10^{14}	5.0×10^{13}
Undoped Ga_2O_3 (A)	1.8×10^{15}	5.1×10^{16}	4.6×10^{16}	1.9×10^{15}	-
Undoped Ga_2O_3 (B)	1.5×10^{15}	6.8×10^{16}	1.1×10^{16}	-	-
Mg-doped Ga_2O_3	1.4×10^{18}	1.7×10^{17}	7.1×10^{16}	7.4×10^{18}	-
Ca-doped Ga_2O_3	5.5×10^{15}	3.5×10^{16}	2.3×10^{17}	-	1.0×10^{16}

Table 4.2: SIMS analysis of impurity concentrations (cm^{-3}) for Mg-doped, Ca-doped, and unintentionally doped Ga_2O_3, all annealed in deuterium.

4.4: Magnesium incorporation

4.4.1: Calculated defect formation energies, Mg and Ir

To assess the effects of Ir contamination and Mg incorporation, we include the calculated formation energy diagrams for substitutional Ir and Mg-related defects in Fig. 4.5 for the O-rich and Ga-rich limits. Our results identify that Ir and Mg most favorably incorporate on the octahedral Ga(II) site. Similar to previous studies,[43] we find that $Mg_{Ga(II)}$ acts as a deep acceptor, with a calculated (0/–) charge-state transition level 1.06 eV above the valence-band maximum (VBM). Consistent with the work of Kananen *et al.*,[44] we find the hole most favorably localizes on an adjacent O(I) atom, while a hole localized on the O(II) atom is 0.16 eV higher in energy. Mg on the tetrahedral Ga(I) site is less favorable by 0.5 eV for both the neutral and negative configurations, yielding a slightly deeper acceptor level of 1.27 eV. Mg interstitials (Mg_i) are shallow donors that can be favorable for Fermi levels below mid-gap. However, O-rich conditions suppress the formation of this self-compensating species.

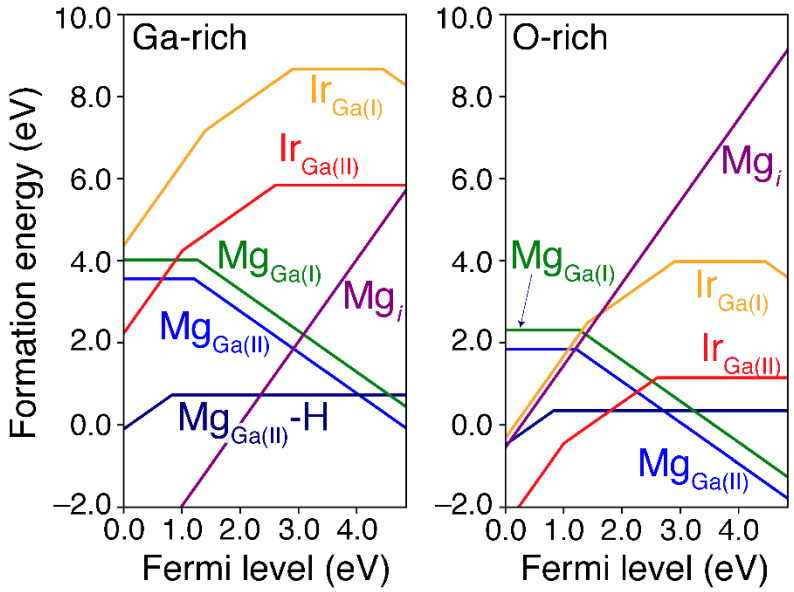

Figure 4.5: Formation energy diagrams for Mg-related defects in Ga_2O_3 shown for Ga-rich and O-rich limits. The results identify Mg_i as a shallow donor, while Mg_{Ga} is a deep acceptor most favorable in *n*-type conditions. Mg_{Ga} acceptors can also form complexes with H_i donors leading to their electrical passivation.

Conversely, $Ir_{Ga(II)}$ acts as a deep donor with two levels in the band gap, indicating Ir_{Ga} defects are electrically inactive in *n*-type Ga_2O_3. The (+/0) charge-state transition level corresponding to the Ir^{4+} oxidation states is calculated to be close to mid-gap, 2.60 eV above the VBM (2.25 eV below the conduction-band minimum, CBM). An additional (2+/+) charge-state transition level is calculated to be 1.01 eV above the VBM.

4.4.2: Ir^{4+} peak

Experimentally, the Mg-doped Ga_2O_3 samples exhibit a strong IR absorption peak at 5148 cm^{-1} (Fig. 4.6). Based on its similarity to absorption peaks from Ir^{4+} in other oxides,[45,46] we attribute it to Ir^{4+} impurities introduced by the iridium crucible.[22] The peak is assigned to a transition from the ground state to an excited *d*-orbital. Undoped Ga_2O_3 samples that have similar concentrations of iridium (Table 4.2) do not show evidence of these features, presumably

because the iridium is in the form of Ir^{3+}, which is not IR active for electronic transitions. Magnesium accepts an electron from the iridium donor, creating the IR-active Ir^{4+}. Further supporting this idea, the magnesium acceptors can be passivated to be neutral through hydrogen annealing.

In Fig. 4.5 we also included the formation energy of hydrogen complexes with Mg_{Ga} ($Mg_{Ga(II)}$-H), which we find to be favorable defects that render Mg_{Ga} acceptors electrically neutral. Relative to the isolated H_i^+ donors and $Mg_{Ga(II)}$ acceptors, we find the neutral complex is 0.6 eV more preferable, indicating a modest binding energy. Thus, hydrogen passivation of magnesium acceptors would no longer require them to be compensated by donors and lead to a Fermi level higher in the band gap. If the neutral complexes can no longer be compensated by iridium donors, the majority of iridium in the crystal must have the form of Ir^{3+}. As a result, hydrogen annealing Ga_2O_3:Mg greatly suppresses the Ir^{4+} peak (Fig. 4.6 & 4.7)

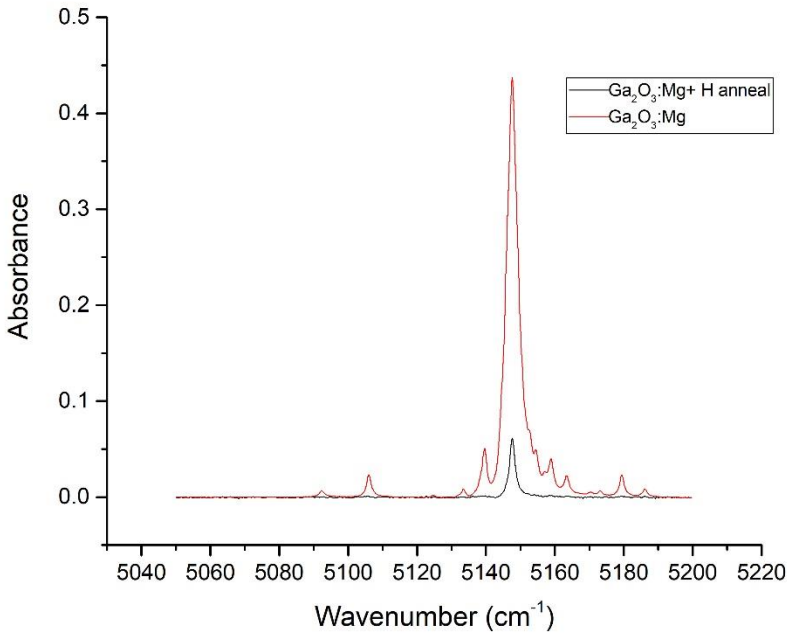

Figure 4.6: IR absorption spectrum of Ir^{4+} in Mg doped Ga_2O_3 before and after hydrogen annealing.

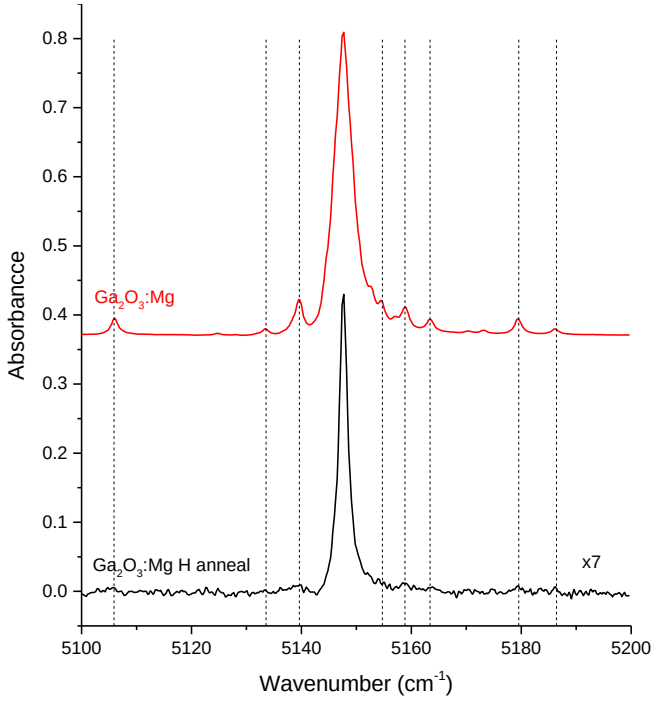

Figure 4.7: IR spectra of Mg-doped gallium oxide before and after hydrogen annealing for closer inspection of sideband features. The hydrogen annealed sample has been scaled for comparison. Spectra are offset for clarity.

UV/visible transmission spectra of the Mg-doped samples show an absorption threshold at 2.8 eV (Fig. 4.8). This absorption threshold is not observed in the spectra of undoped Ga_2O_3, nor in Ga_2O_3:Mg produced by float-zone crystal growth.[15] Because of this, we attribute the absorption to the excitation of a valence-band (VB) electron to the $Ir^{4+/3+}$ level, rather than an excitation to/from the Mg level. Like the 5148 cm^{-1} peak in figure 4.6, the absorption threshold at 2.8 eV in the transmission is also suppressed with hydrogen annealing. Note that there is a second threshold at 3.2 eV. This feature could be due to the transition of a VB electron to an Ir^{3+} excited state, similar to the case of Fe in GaAs.[47]

To assess optical transitions between $Ir_{Ga(II)}$ and the valence and conduction bands, we calculated the excitation energies in a configuration coordinate diagram analysis (Fig. 4.9). For the process of electron capture from the VBM to the $Ir_{Ga(II)}^{+}$ donor state, the calculations predict a zero-phonon line of 2.6 eV and an absorption peak of 3 eV, which closely match the features in the measured spectra (Fig. 4.8). We additionally predict transitions to the CBM from the filled state of the neutral $Ir_{Ga(II)}$ (Ir^{3+}/Ir^{4+}) with similar absorption peak of 2.8 eV and onset of 2.25 eV. However, these features are not observed in undoped Ga_2O_3 (Fig. 4.8). This is similar to GaAs:Fe, where the lack of an Fe-to-CBM absorption feature was attributed to a very low optical cross section for that particular transition.[47]

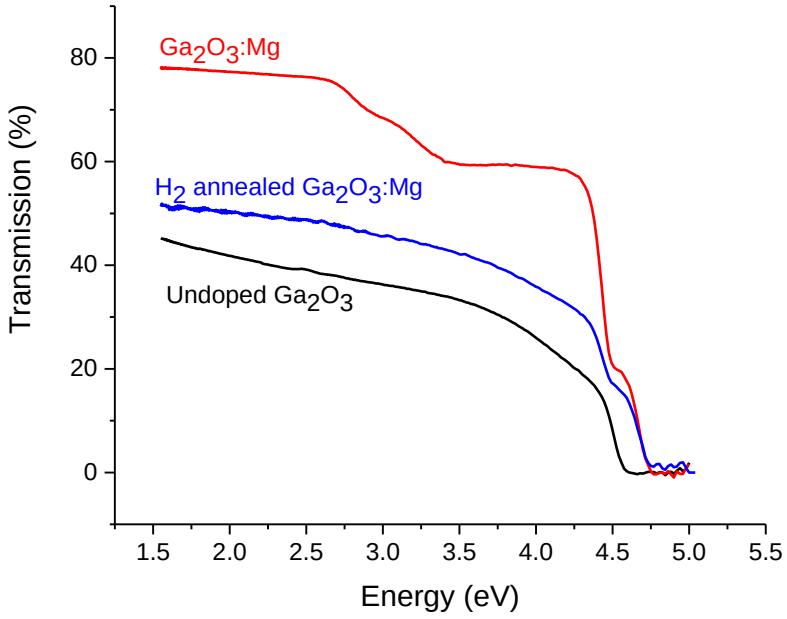

Figure 4.8: UV/visible transmission spectra of undoped Ga_2O_3, Mg-doped Ga_2O_3, and H_2 annealed Mg-doped Ga_2O_3. Only the Ga_2O_3:Mg sample shows an absorption threshold at 2.8 eV. Band-gap absorption is observed near 4.5 eV.

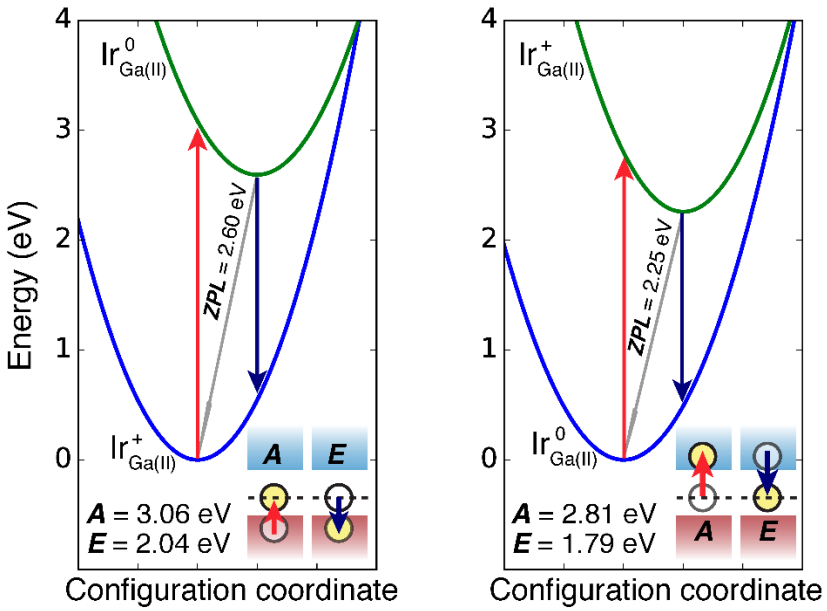

Figure 4.9: Calculated configuration coordinate diagram for optical excitations with $Ir_{Ga(II)}$ exchanging electrons with the VBM (left panel) and the CBM (right panel). The calculated absorption onset of 2.6-3 eV associated with an electron capture from the VBM by the $Ir_{Ga(II)}^{+}$ donor state agrees well with the measured absorption in Fig 4.8.

4.4.3: Magnesium-hydrogen complex

Neither the iridium-hydrogen complexes nor the $V_{Ga}2H$ peaks present in the undoped sample (Fig. 4.3) were observed in H-annealed Ga_2O_3:Mg. Instead, a new hydrogen-related peak appears in the IR spectrum at 3492 cm^{-1} (Fig. 4.10), attributed to the O-H bond-stretching mode of a MgH complex. The lack of IrH peaks could possibly be connected to the fact that in Ga_2O_3:Mg most of the iridium is Ir^{4+}, and thus repels electrons and won't pair with hydrogen.

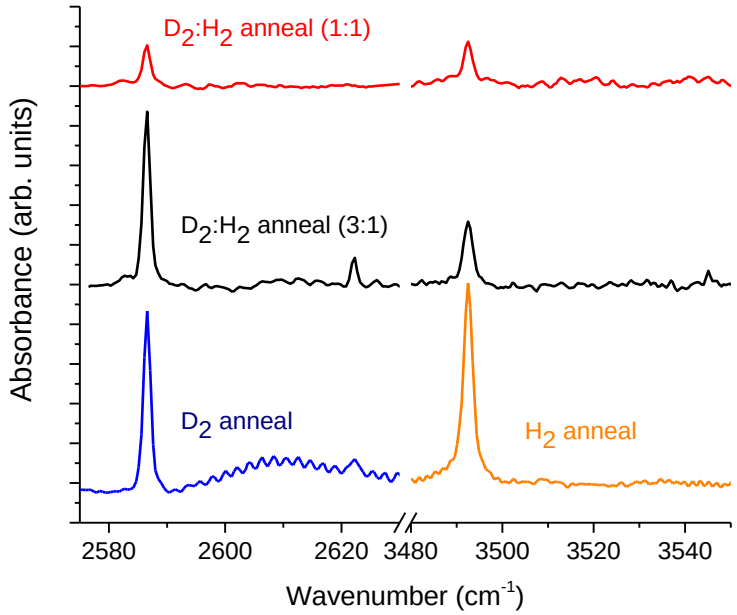

Figure 4.10: IR absorption spectra of Ga_2O_3:Mg annealed in D_2, H_2, and D_2:H_2 mixtures.

To confirm that the 3492 cm^{-1} feature is a hydrogen-related defect, Ga_2O_3:Mg was annealed in deuterium. The resulting peak was appropriately shifted to 2586 cm^{-1} (Fig. 4.11, top). To establish the number of passivating hydrogen atoms involved in the complex, we annealed a sample in a mixture of H_2 and D_2. If the O-H and O-D peaks were the result of a two

hydrogen center, "H-D" peaks would be expected to appear from centers that contained one H and one D.[48] As shown in Figure 4.10, varying ratios of hydrogen and deuterium changes the relative intensity of the O-H and O-D peaks but no H-D peaks were observed. From the lack of H-D peaks, we conclude that the magnesium-hydrogen center in Ga_2O_3 is a Mg_{Ga} acceptor passivated by one H atom. A weaker O-H (O-D) line was observed at 3545 cm^{-1} (2622 cm^{-1}), but its intensity varied from sample to sample. This line may be due to a different acceptor-hydrogen complex.

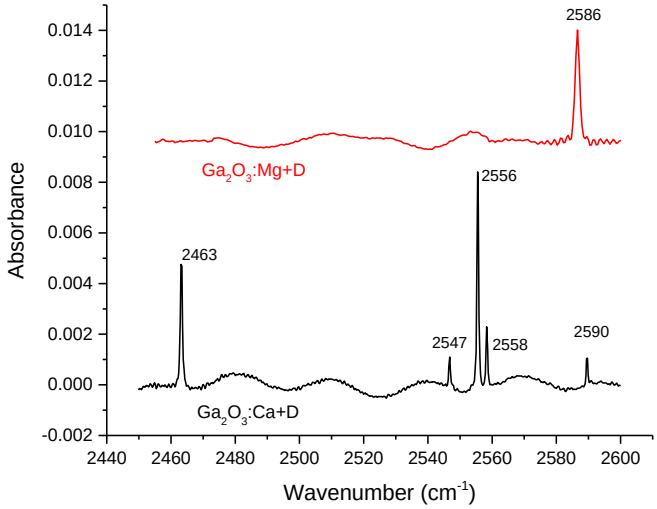

Figure 4.11: IR spectra of deuterated Ga_2O_3:Mg (red) and Ga_2O_3:Ca (black). 2586 cm^{-1} is a peak for a MgD O-D stretching mode in Ga_2O_3:Mg and 2558 cm^{-1} is a peak for a CaD complex in Ga_2O_3:Ca.

4.4.4 MgH Polarization

IR spectra of the H-annealed Ga_2O_3:Mg sample were taken at various angles with a linear polarizer to observe the relative strength of the 3492 cm^{-1} O-H peak (Fig. 4.12). The resulting

spectra show the hydrogen related peak strongest when **E**//**c** and not observable when **E**//**b**. From this we conclude the O-H dipole is oriented in the *a*-*c* plane.

To additionally confirm this assignment, we calculated the anharmonically-corrected vibrational frequencies associated with the $Mg_{Ga(II)}$-H complex ($\omega = \omega_0 - \Delta\omega$). Owing to the energetically preferable configuration of H bonded to an O(I) atom, the complex consists of the O-H bond oriented largely along the *a*-axis within the *a*-*c* plane adjacent to the $Mg_{Ga(II)}$ (Fig. 4.12, inset). Our calculated frequency is $\omega = 3617$ cm^{-1} ($\omega_0 = 3889$ cm^{-1} and $\Delta\omega = 272$ cm^{-1}), which is 125 cm^{-1} higher than the experimental frequency. A similar overestimate (181 cm^{-1}) was found for O-H complexes in SnO_2.[49,50] From the good agreement of this peak with the experimentally identified IR peak and the associated polarization dependence, the $Mg_{Ga(II)}$-H complex is a plausible candidate for the 3492 cm^{-1} peak. We additionally compute wag modes of 1203 cm^{-1} (within the *a*-*c* plane) and 717 cm^{-1} (within the *a*-*b* plane) within the harmonic approximation using linear response theory, but these were not measured due to strong two-phonon absorption in that spectral region.

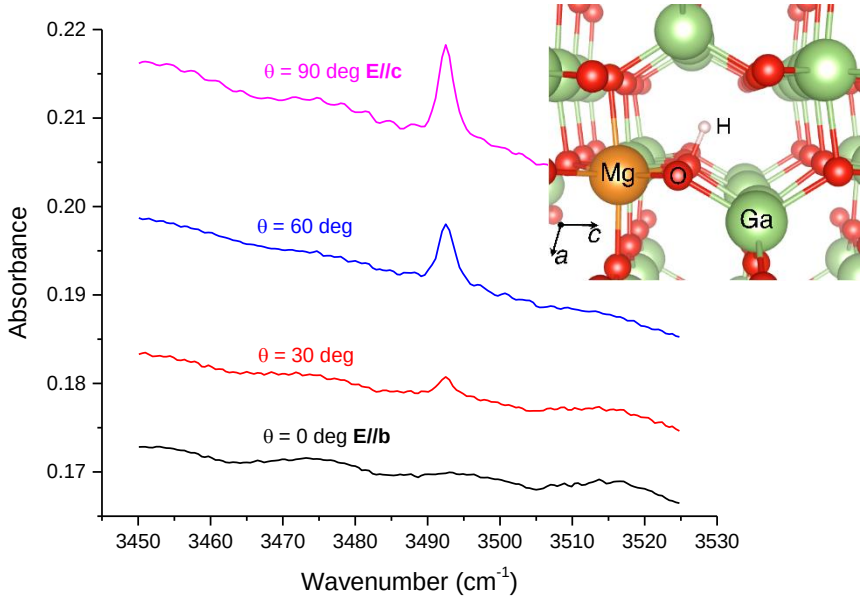

*Figure 4.12: IR absorption spectra of the primary hydrogen peak in H-annealed Ga_2O_3:Mg. $\theta = 0$ corresponds to polarization along the **b** axis. Spectra are displaced vertically for clarity. Inset: Calculated model of the Mg-H complex.*

4.5: Calcium incorporation

4.5.1: CaH complex

While hydrogen annealing a Mg-doped sample eliminated the IrH and $V_{Ga}2H$ peaks and gave rise to a single Mg-related O-H peak (Fig. 4.11), annealing a Ca-doped sample instead still presented the exact same four peaks while also giving rise to a new peak at 3441 cm^{-1} (Fig 4.13). A corresponding peak at an isotopic shift of 1.346 occurs with a deuterium anneal, confirming that the new peak is indeed a consequence of hydrogen incorporation.

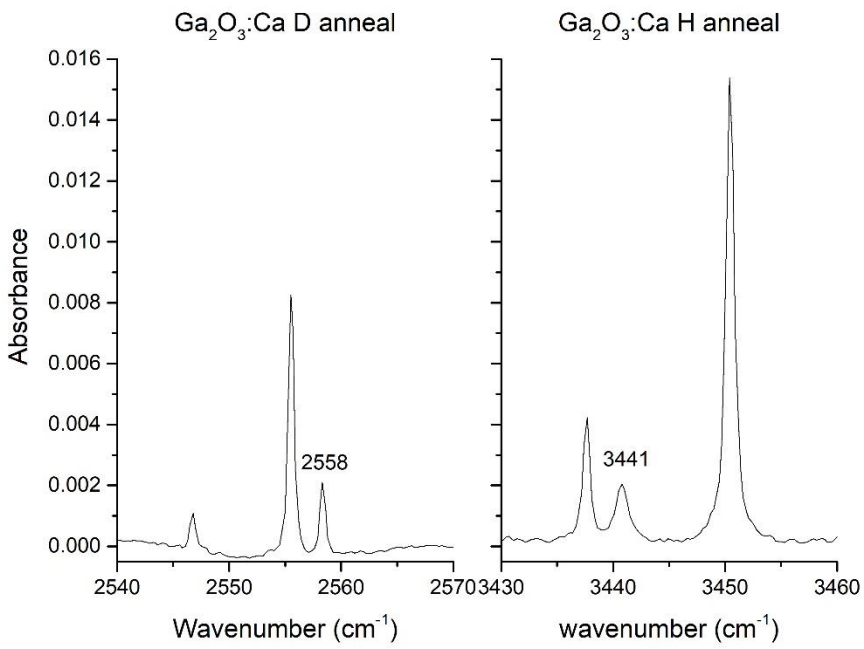

Figure 4.13: IR spectra of calcium-doped Ga_2O_3 annealed in deuterium (left) and hydrogen (right). All peaks from the undoped sample (Fig. 4.3) are present, but there is a new hydrogen-related peak at 3441 cm^{-1} and new deuterium-related peak at 2558 cm^{-1}.

As with the undoped and Mg-doped samples, in an attempt to learn more about the number of passivating atoms in this calcium-related complex we annealed our samples in a mix of H_2 and D_2. As shown in Fig. 4.14, the deuterium generated peak appears to split into an H-D mode with a peak at 2558 cm^{-1}, but no such splitting is immediately obvious in the hydrogen annealed spectrum. Furthermore, a previously unidentified peak at 3447 cm^{-1} becomes visible with an H+D mixture anneal. Because these findings are inconclusive, more work is needed to convincingly establish the number of hydrogens associated with this Ca-H structure. The V_{Ga}HD peaks provide a nice example of the H-D splitting in figure 4.14.

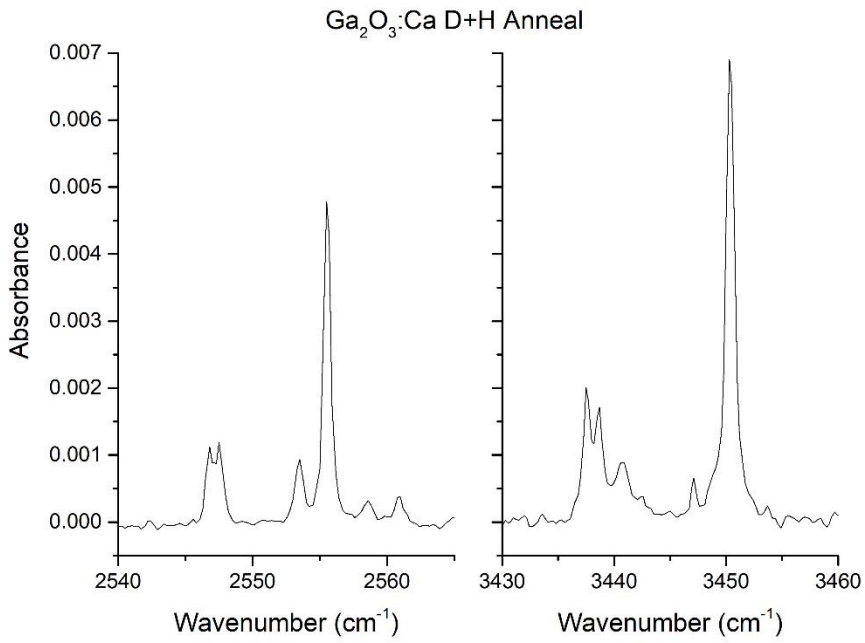

Figure 4.14: IR spectra of calcium-doped Ga_2O_3 annealed in a mix of H and D. This anneal also gives rise to an unknown peak at 3447 cm^{-1}.

In section 4.4.4 we used a combination of polarization experiments and calculation to identify that the O-H bond for the Mg defect lies within the *a*-*c* plane, close to the *a* axis. To aid with experimental positioning *within* the *a*-*c* plane the sample was rotated around the *b* (010) axis in increments while taking IR measurements, with the peak area showing a very clear angle dependence (Fig 4.15). Due to angle limitations within the instrumentation it was not possible to reach a positive maximum or minimum, limiting the ability to pin down an exact angle within the *a*-*c* plane for the bond direction using this method. Applying this same approach to a H annealed Ga_2O_3:Ca sample shows that the previously mentioned Ca-H related IR peak at 3441 cm^{-1} has the same behavior as the Mg peak did (Fig 4.15). The similar behavior between peaks suggests that calcium might be substituting in a similar way to magnesium, so it is possible but unconfirmed that the O-H bond may be similarly located for both defects.

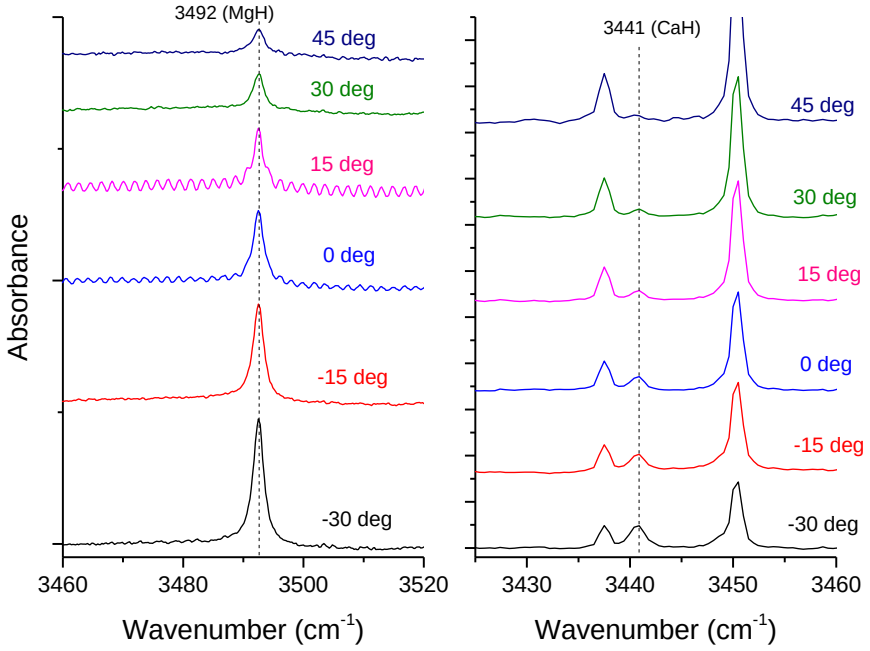

Figure 4.15: IR spectra of hydrogen annealed magnesium-doped Ga_2O_3 (left), and hydrogen-annealed calcium-doped Ga_2O_3 (right), shown through a series of rotations around the b *axis. 0 degrees indicates the (100) surface is normal to the incident light.*

Due to this correlation of bond angle, as well as the established relationship to hydrogen impurities, we tentatively assign the identified peaks in the Ga_2O_3:Ca structure to an O-H/O-D bond stretching mode adjacent to the $Ca_{Ga(II)}$.

4.5.2: Photon excitation of the Ir^{4+} peak

In section 4.4.2, first principles calculations assigned a 2.25 eV energy onset for the transition from the Ir_{Ga} level to the conduction band in Ga_2O_3:Mg. With that in mind, we exposed a hydrogen-annealed Ga_2O_3:Mg sample to incrementally shorter wavelength light emitting diodes (LEDs). Photon energies above 2.3 eV increase the Ir^{4+} peak area significantly, as the photon excites an electron from Ir^{3+} to the conduction band to create more Ir^{4+} (Fig. 4.16). When plotting the peak intensity vs excitation energy, the threshold of activation for this

transition falls between 2.2 and 2.3 eV (Fig. 4.17). This finding agrees with the calculated 2.25 eV energy onset.

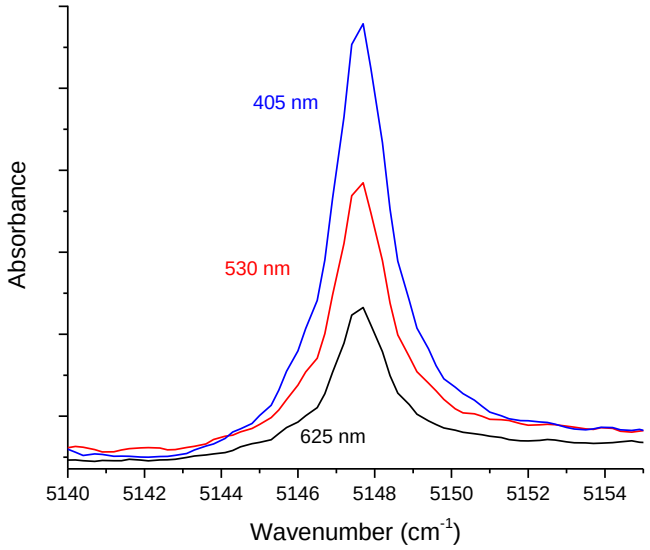

Figure 4.16: IR spectra of H-annealed Ga_2O_3:Mg. When exposed to photons of increasing energy, more iridium in the Ir^{3+} state is excited to Ir^{4+}, increasing the size of the 5148 cm^{-1} Ir^{4+} peak.

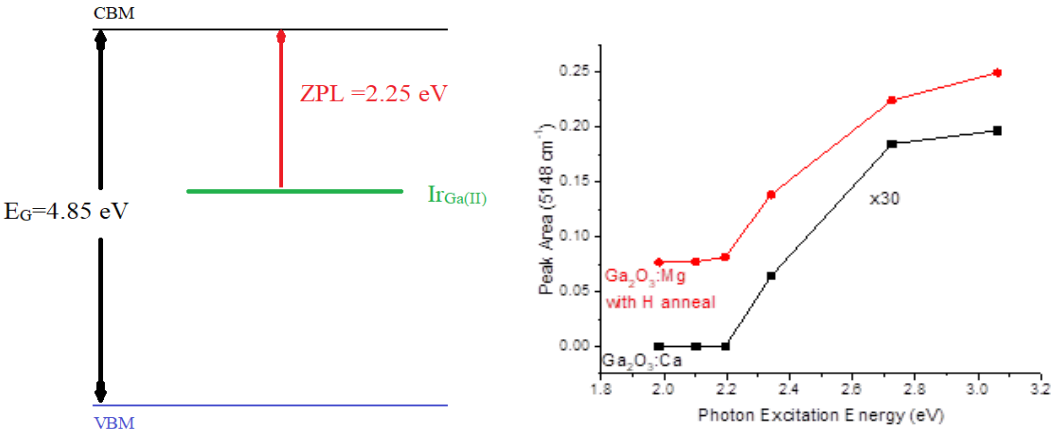

Figure 4.17: Plot of the 5148 cm^{-1} peak versus excitation photon energy for Ga_2O_3:Ca (squares) and H-annealed Ga_2O_3:Mg (circles). Sequential exposures of increasingly higher energy light show that the threshold for exciting an electron from the Ir^{3+} level to the conduction band minimum occurs between 2.2 and 2.3 eV.

We performed similar experiments on calcium-doped gallium oxide. Without excitation, Ca doped samples show no evidence whatsoever of an Ir^{4+} peak. Photon excitation causes the peak to appear, and the threshold for the Ir^{4+} peak to appear is very comparable to that of the hydrogen-annealed Ga_2O_3:Mg. (Fig. 4.17). This provides further evidence that that the energy level for iridium in Ga_2O_3 is 2.25 eV below the conduction band minimum, regardless of the dopant in this case.

For the Ga_2O_3:Mg samples that had not been annealed in hydrogen, exposure to the same light had no impact on peak intensity (Fig. 4.18). This is presumably because all of the iridium is already in the Ir^{4+} state and so there are no Ir^{3+} states to excite.

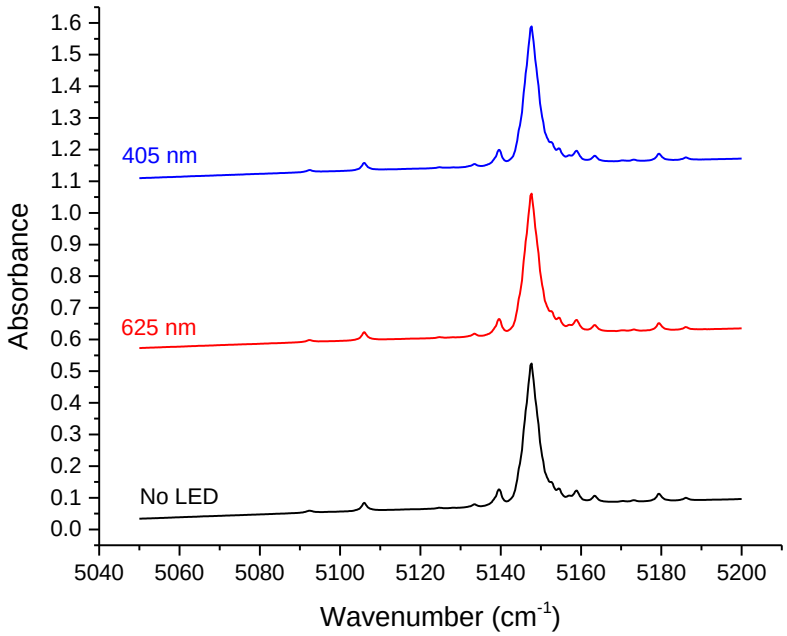

Figure 4.18: IR spectra of unannealed magnesium doped gallium oxide with and without external photon exposure. The photon excitation produces no visible change in the primary peak. Spectra are offset for clarity.

4.6: Ir^{4+} sidebands and polarization

4.6.1: Ga_2O_3:Fe peak

IR spectroscopy was also performed on a commercially grown Ga_2O_3:Fe sample with (010) surface orientation, to further investigate the Ir^{4+} feature. Much like H-annealed Ga_2O_3:Mg and Ga_2O_3:Ca, the 5148 cm^{-1} peak can be greatly enhanced with sufficient photon excitation (Fig. 4.19). Iron can act as a deep acceptor in Ga_2O_3, but because the iron level is not as deep as the Ir level, it is surprising to see evidence of the Ir^{4+} transition.[51] The Fe-doped sample presumably contains an acceptor complex with a level that lies below the $Ir^{3+/4+}$ donor level.

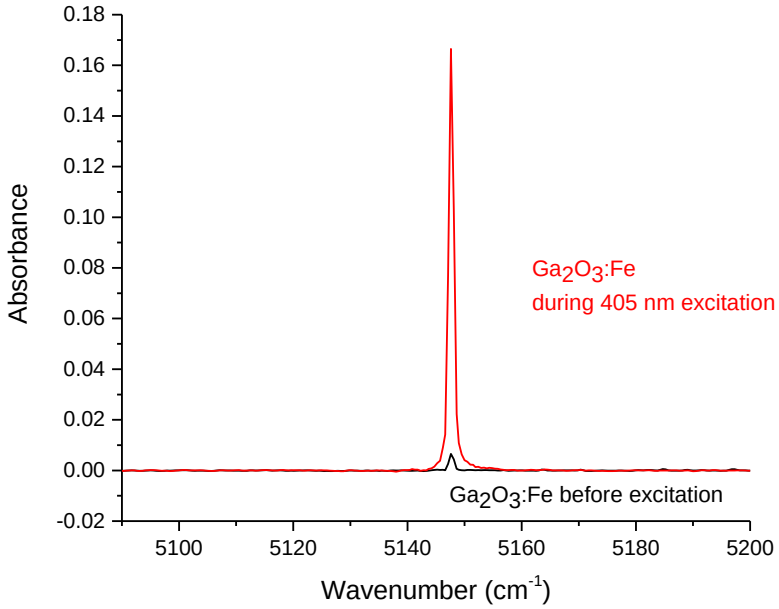

Figure 4.19: IR spectra of the 5148 cm^{-1} Ir^{4+} peak in Ga_2O_3:Fe before (black) and during (red) excitation with 405 nm light.

4.6.2: Ir^{4+} sidebands

There is an immediately noticeable difference between IR spectra for magnesium doped gallium oxide when compared to the calcium or iron doped materials. Mg-doped Ga_2O_3 samples

show a strong IR absorption peak at 5148 cm^{-1} and a large number of smaller neighboring peaks from 5090-5190 cm^{-1} (Fig. 4.7). The full list of sideband energies and intensity relative to the primary peak are given in table 4.3 below.

Ir^{4+} peak positions (cm^{-1})	Relative height
5092.4	0.015
5106.0	0.054
5124.6	0.005
5128.0	0.001
5133.5	0.021
5139.6	0.112
5147.6 (primary)	1.000
5152.6	0.020
5154.4	0.034
5157.2	0.018
5158.8	0.060
5163.4	0.040
5170.3	0.008
5173.2	0.010
5179.4	0.053
5185.2	0.018

Table 4.3: List of peak energies for Ir^{4+} in Ga_2O_3:Mg (see Fig. 4.7).

For calcium and iron doped samples, none of these sidebands are present, only the largest peak at 5148 cm^{-1} (Fig. 4.20). While the primary peak is present for all dopants and assigned to an Ir^{4+} transition, the lack of sidebands in any materials not doped with magnesium suggests that they potentially arise from more complicated defects. As shown in Fig. 4.18, when a Ga_2O_3:Mg sample was excited by a series of increasingly energetic photons, there was no change in the intensity of the 5148 cm^{-1} peak.

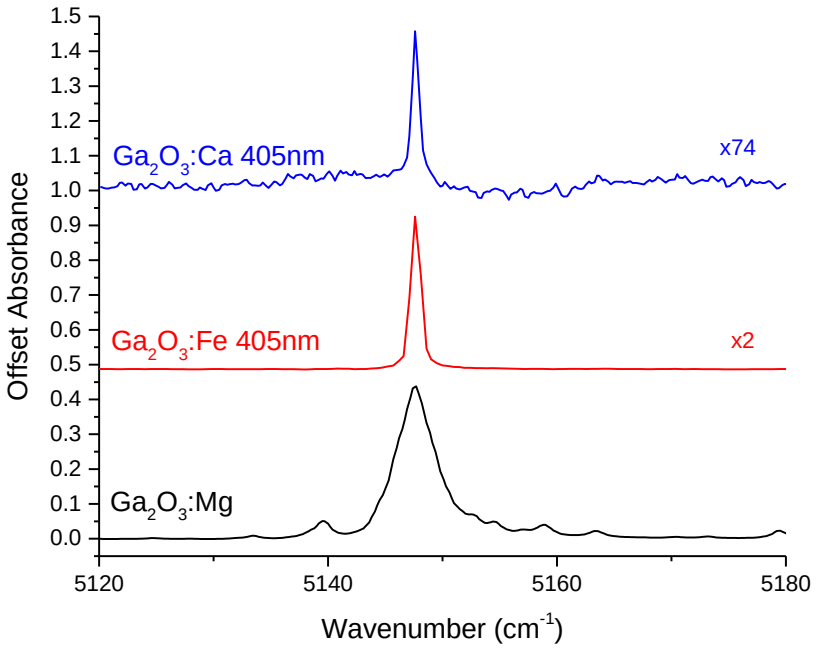

Figure 4.20: IR spectra of Ir^{4+} in Mg, Fe, and Ca doped gallium oxide. The Mg doped sample has sidebands that are not present in samples without Mg. The larger width of the Ga_2O_3:Mg Ir^{4+} peak is at least partially due to sidebands underneath the primary peak (Fig. 4.21). Spectra have been offset vertically and scaled for clarity.

However, a subtraction spectrum reveals that the sidebands decrease in absorbance with higher energy excitation photons, implying that the sidebands arise from different centers than the primary peak (Fig. 4.21). Combining this with the fact that the sidebands only arise in the presence of magnesium, we posit that the sideband peaks are due to iridium-magnesium pairs, where the Ir^{4+} transition is perturbed by a neighboring Mg^-. The slight decrease in absorbance suggests that the excitation puts some of the iridium into the Ir^{3+} state, perhaps by neutralizing a magnesium acceptor via charge transfer ($Ir^{4+}Mg^- \rightarrow Ir^{3+}Mg^0$).

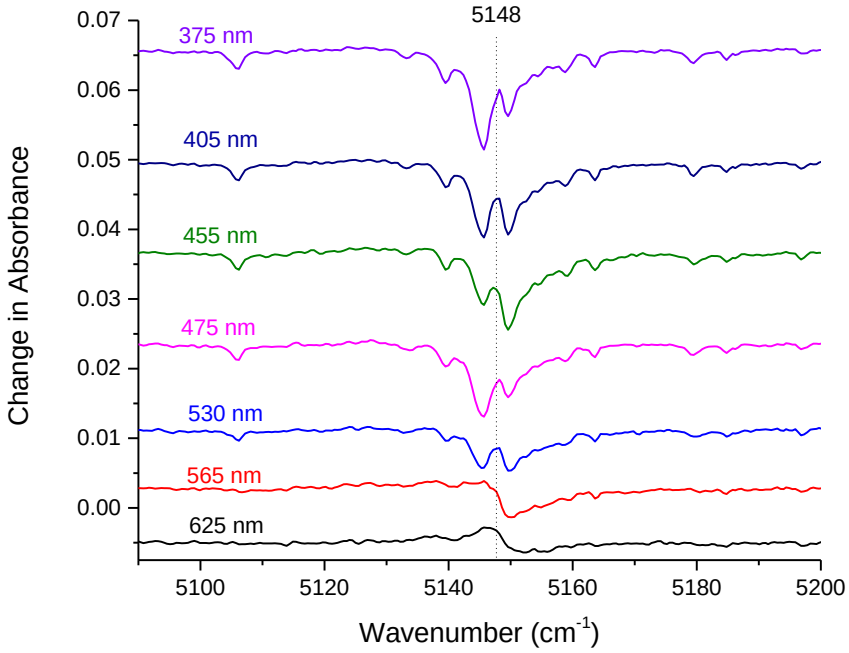

Figure 4.21: IR subtraction spectra of Ga_2O_3:Mg exposed to LEDs. Each spectrum is subtracted against an IR spectrum taken before the sample was exposed to light. Even though there was no change in the primary 5148 cm^{-1} peak, the subtraction spectra reveal that there are small changes in the absorbance of all of the sideband features, suggesting that the sidebands and primary peak come from different defects. Spectra are offset vertically for clarity.

4.6.2: Ir^{4+} polarization

Polarization experiments show that the Ir^{4+} peak and sidebands have preferred directions of excitation. For a (100) oriented Mg-doped sample a linear polarizer was inserted into the beam path such that $\Theta = 0^{o}$ corresponds to light polarized along the **b** axis. As shown in Fig. 4.22, the Ir^{4+} peak is strongest when the incident light is polarized along the **b** axis and weakest when polarized along the **c** axis. Similarly, for the Fe-doped (010) oriented sample, the peak is strongest with incident light polarized along the **a** axis and weakest along the **c** axis (Fig. 4.22). These results suggest that while the $Ir^{3+/4+}$ transition is significantly less probable along the **c** axis it is not disallowed entirely, in agreement with the findings of Lenyk *et al*.[52] More investigation is needed to understand the origin of this anisotropy.

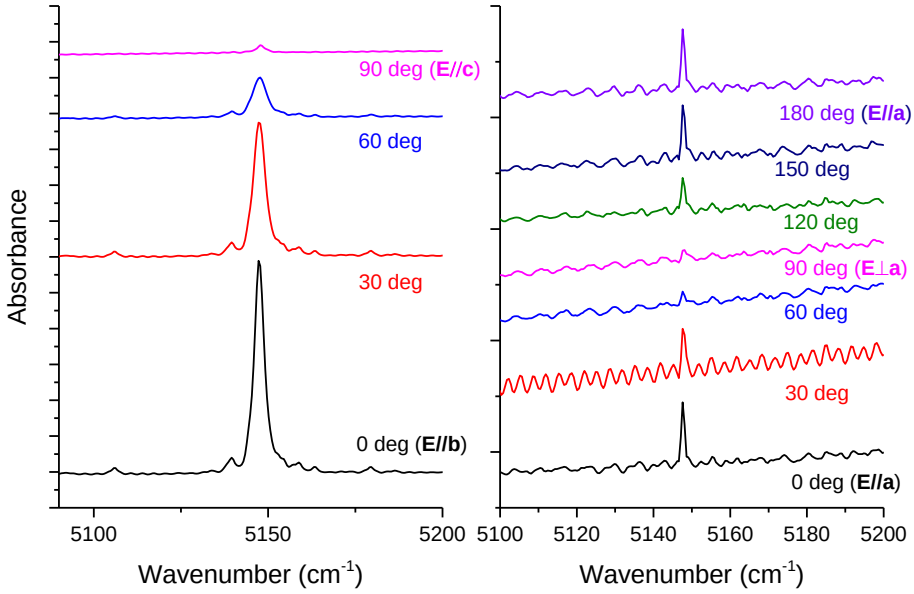

Figure 4.22: Polarized IR spectra for Ga_2O_3:Mg (left) and Ga_2O_3:Fe (right). For the Mg-doped spectrum light is incident to the (100) plane and for the Fe-doped spectrum light is incident to the (010) plane.

CHAPTER FIVE: Ga_2O_3 CONCLUSIONS AND FUTURE WORK

5.1: Conclusions

We have observed H and Ir defects in undoped, magnesium-doped, and calcium-doped β-Ga_2O_3. In both undoped and Ca-doped Ga_2O_3 annealed in hydrogen, O–H vibrational modes at 3313, 3450, and 3500 cm^{-1} were tentatively attributed to IrH complexes. Ga_2O_3:Mg annealed in hydrogen forms neutral MgH complexes with an O-H vibrational mode at 3492 cm^{-1}. Annealing Ga_2O_3:Ca in hydrogen forms a CaH complex with a vibrational mode at 3441 cm^{-1}. All of these modes have been confirmed as O-H modes by annealing in deuterium, the observed isotopic frequency shift from O-H to O-D modes agrees well with a similar shift observed in other materials. Polarization experiments agree with calculation that the O-H bond in Ga_2O_3:Mg is oriented within the *a*-*c* plane and lies close to the **a** direction.

In Mg-doped Ga_2O_3 there is an electronic transition related to Ir^{4+} at 5148 cm^{-1}, as well as numerous smaller transition peaks ranging from 5090-5190 cm^{-1}. This peak is weakened by hydrogen annealing, and once weakened can be enhanced by excitation from an external light source. A 5148 cm^{-1} peak can also be enhanced in the same way in Ca- and Fe-doped Ga_2O_3, although without excitation the peak is not visible for the Ca-doped samples. Our experimental results concur with first-principles calculations that place the Ir donor level 2.25 eV below the conduction-band minimum. Since smaller transition peaks can only be seen in Mg-doped Ga_2O_3, we assign them to iridium-magnesium pairs, each energetically different based on the specific site of the magnesium neighbor.

The Ir^{4+} peak also exhibits strong polarization effects, such that it is weakest for light polarized along the **c** axis. This is confirmed by other reports, but the mechanism is not yet well understood.

Pressed indium contacts were used for two-point resistance measurements. In undoped β-Ga_2O_3 we reported a resistance of ~10KΩ and magnesium doped β-Ga_2O_3 had a resistance of ~300GΩ, then hydrogen annealing reduces the resistance to the 10GΩ range. In short, magnesium incorporation makes Ga_2O_3 insulating, and hydrogen annealing it passivates some of the magnesium acceptors and reduces the insulating properties. Doping samples with Ca, on the other hand, only increases the resistance measurement to ~10MΩ. From this we understand Ca incorporation to be much less effective at making Ga_2O_3 insulating when compared to Mg incorporation. One possible reason for this could just be that much less calcium is incorporated. For elements of the same group, impurity doping can become less effective with increasing dopant radius.

SIMS shows that hydrogen is much more readily incorporated into the magnesium doped β-Ga_2O_3 than undoped (lightly *n*-type) material. This observation, along with resistance measurements, support the idea that Mg doping lowers the Fermi level significantly. Ir from crucible compensates the magnesium acceptors, along with Si impurities. However, the concentration of Mg is much higher than these compensating donors. While oxygen vacancies and Mg_i may compensate acceptors, O-rich growth conditions can suppress the formation of these defects and allow the Fermi level to be pushed below mid-gap.

5.2: Future work

The polarization and sideband effects of the Ir^{4+} peak are not yet fully understood. More work should be done to characterize the sidebands and fully confirm that they are indeed a result of Mg-Ir pairs. Before this connection was made, an attempt was made to model the gallium atom and its nearest oxygen neighbors to form a picture of the energies required to allow for the polarization effects displayed, where the transition goes nearly but not fully to 0 when E//**c**. A successful distribution of eigenvalues was never found, and it would be useful to have a working model that explained the polarization dependence of the Ir^{4+} that is easily demonstrated by experiment. These efforts are described in Appendix A

Kelvin Lynn's lab at the WSU Institute for Materials Research has also grown n-type Hf- and Zr- doped Ga_2O_3 samples. These will be characterized to further detail the effects of transition metals in Czochralski grown gallium oxide.

Preliminary work has begun creating gallium oxide targets in order to sputter thin films for characterization. This will make it possible to more precisely control dopant concentrations and make strides towards simple devices.

CHAPTER SIX: ZINC SULFIDE OXIDE ALLOYS ($ZnS_{1-x}O_x$)

6.1: Introduction and motivations

6.1.1: Zinc oxide (ZnO)

Zinc oxide (ZnO) is a wide band gap semiconductor with a wide range of optoelectronic uses. It has a band gap of 3.37 eV, a wurtzite crystal structure, and a high efficiency of UV emission.[53,54] ZnO is non-toxic, and cheaper to grow in single crystals than many of its semiconducting counterparts. Even in its current state of development, ZnO has uses from LEDs to solar cells to sunscreen. Unfortunately for some purposes, ZnO is intrinsically *n*-type, with many donors from oxygen vacancies, zinc interstitials, and lots of common impurities. Any *p*-type doping is a major challenge, because it is very difficult to introduce acceptors without them being dominated by compensating donors.[54]

6.1.2: Alloying with ZnS

A great many more useful and powerful ZnO based devices would be made possible if *p*-*n* junctions were available for the material, but as it stands there are no uncontroversial reports of good hole conduction in ZnO. To this end, efforts were made to create *p*-type alloys that could behave similarly enough to ZnO to create a *p*-*n* junction.

The interest in a ZnS_xO_{1-x} alloy comes from the reports by Persson *et al*. that the alloy exhibits a very strong valence band-offset bowing as a function of sulfur content (Fig. 6.1).[55] Even though the band gaps of ZnO and ZnS are not too far apart in energy (~3.3 and 3.6 respectively), because the valence and conduction bands do not move together it is possible to tune the band gap of the alloy to as low as 2.7-2.8 eV. In the same way, an acceptor that might

be unusably deep in ZnO might be much closer to the band and so much more effective at promoting *p*-type conductivity in a ZnSO alloy.

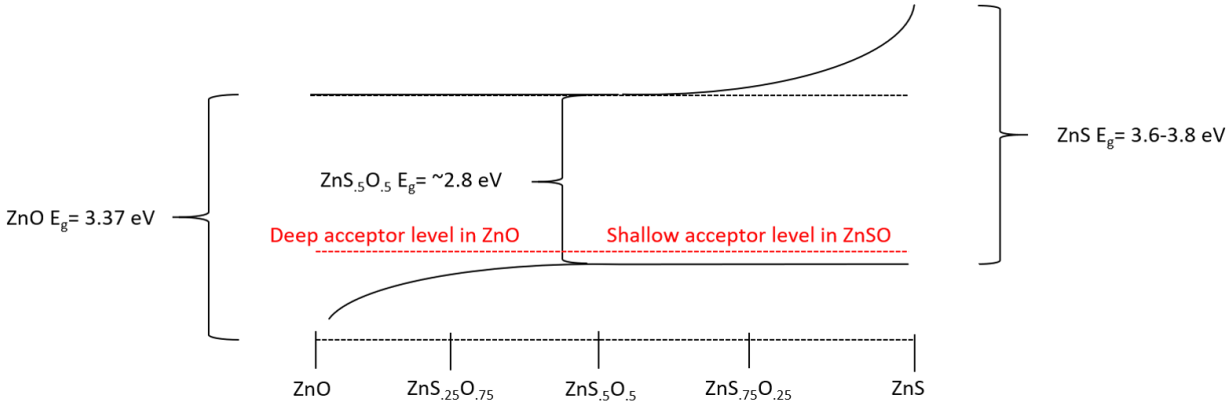

Figure 6.1: Simplified diagram of conduction and valence bands in a ZnS_xO_{1-x} alloy. The band gap energies can be smaller for an alloy than for either pure crystal. What might be a deep acceptor in ZnO can be shallow for an alloy.

6.1.3: Experimental research done

The majority of our work performed on this project involves the growth and characterization of ZnSO thin films with the intent of later acceptor-doping the films either during growth or with some method of implantation.

The films were grown using the (rf) sputtering method described in chapter 3. The sputtering target was a pressed ZnS powder, and oxygen was added to the growth as a reactive gas. XPS, XRD, and EBSD were utilized to check alloy concentration levels while learning appropriate parameters for growth. Resonant Raman scattering was used to investigate the local vibrational modes associated with the ZnSO alloy. This research resulted in the publication of the following two papers:

- "Oxygen Vibrational Modes in $ZnS_{1-x}O_x$ Alloys",

  J. Huso, J.R. Ritter, D. Thapa, K. Yu, L. Bergman, and M.D. McCluskey,

  J. Appl. Phys. **123**, 161537:1-5 (2017).

- "High Order Oxygen Local Vibrational Modes in $ZnS_{1-x}O_x$",

  J. Huso, J.R. Ritter, L. Bergman, M.D. McCluskey,

  Phys. Stat. Solidi B **2019**, 1800607:1-9 (2019).

The following two sections are reproductions in full of these two papers, which focus on Raman spectroscopy of the LVMs of these alloys with Jesse Huso as first author.

6.2: Oxygen Vibrational Modes in $ZnS_{1-x}O_x$ Alloys

Jesse Huso[1], Jacob R. Ritter[1], Dinesh Thapa[2], Kin Man Yu[3], Leah Bergman[2], Matthew D. McCluskey[1]

1. *Department of Physics and Astronomy, Washington State University, Pullman Washington 99164-2814*
2. *Department of Physics, University of Idaho, Moscow Idaho 83844-0903*
3. *Department of Physics, City University of Hong Kong, 83 Tat Chee Avenue, Hong Kong SAR, China*

ABSTRACT

$ZnS_{1-x}O_x$ alloy films were studied via resonant Raman spectroscopy. Films with low oxygen content exhibit ZnS longitudinal optical modes and additional modes attributed to O local vibrational modes (LVMs). The frequencies of these modes are explained by a simple mass-defect model. As the O content increases, pairs and larger clusters form, causing the O mode to transition from an LVM to a delocalized phonon. The composition dependence of the modes shows agreement with the modified random element isodisplacement model. Low-

temperature measurements show the O-related mode is composed of multiple features, attributed to zincblende and wurtzite structural regions.

6.2.1: Introduction

The oxide-chalcogenide alloy zinc oxysulfide ($ZnS_{1-x}O_x$) is a promising material for optoelectronic applications. This alloy system presents a number of interesting properties. In particular, the predicted large band gap bowing may enable engineering of the band gap from the UV to the blue/green region of the electromagnetic spectrum despite the band gaps of both endmembers being in the UV.[55–58] $ZnS_{1-x}O_x$ is composed of relatively inexpensive, earth-abundant elements. In addition to deliberate alloying, oxygen is also a common contaminant in ZnS crystals.[59]

First-principles calculations[55] have shown that by adding O to ZnS the conduction band shifts to lower energies while the valence band remains at a nearly fixed energy up to $x \sim 0.5$. Above $x \sim 0.5$, the valence band moves to lower energies while the conduction band remains largely fixed. Thus, a deep acceptor in ZnO may be a shallow acceptor in $ZnS_{1-x}O_x$ for the appropriate alloy composition. Consequently, by raising the valence band, band gap bowing may lead to successful *p*-type doping of ZnO-compatible materials. In addition, the $ZnS_{1-x}O_x$ alloy has attracted attention as a possible non-toxic alternative to CdS buffer layers in chalcopyrite based solar cells.[60,61] In this work, we report composition-dependent resonant Raman scattering measurements of $ZnS_{1-x}O_x$ films grown by reactive radio frequency (rf) magnetron sputtering.

Because O is lighter than S, substitutional O impurities are expected to have a local vibrational mode (LVM), an oscillation that is localized in frequency and real space.[62] An LVM

gives rise to sharp peaks in IR and Raman spectra and involves localized motion of the impurity atom and a only few neighbors. As the O concentration increases into the alloy regime, the vibration transitions from an LVM to an extended, phonon-like excitation. This is known as "two mode" behavior.[63] Other mixed crystal systems known to display two mode behavior include $Si_{1-x}Ge_x$,[64] $GaP_{1-x}As_x$,[65] and $CdS_{1-x}Se_x$.[66] The shift of the vibrational frequencies with composition is described by the modified random element isodisplacement (MREI) model.[67] The MREI model has been successfully applied to a large variety of mixed crystals including $Mg_xZn_{1-x}O$,[68] $Mo_{1-x}W_xS_2$,[69] $K_{1-x}Rb_xI$,[70] and $Ga_xAl_{1-x}N$.[71]

6.2.2: Experimental Methods

The films grown in this work were sputtered using a ZnS ceramic target (99.99%), a power density of 2.5-3.9 W/cm^2 and an rf frequency of 13.56 MHz. Ultra-high purity Ar and O_2 were the working and reactive gasses respectively and were controlled by MKS p4B mass flow controllers. The chamber was evacuated to a base pressure of < $5x10^{-6}$ Torr using a turbomolecular pump. The *c*-plane sapphire substrates were held at 150-200 °C using a custom PID type controller. Resonant Raman measurements were collected using a Horiba T64000 micro Raman/photoluminescence system with a CCD detector and 325 nm excitation. Low temperature measurements were performed using an Instec HCS621V cold stage customized for UV compatibility.

Figure 6.2 presents representative X-ray diffraction (XRD) spectra of the films. The lowest composition film agrees with literature data for ZnS as well as an XRD spectrum of commercial ZnS powder (not shown). The shift in peak position shows that alloying is occurring in the films, in agreement with the Raman results presented here. The XRD peaks of wurtzite

ZnS (002) and zincblende ZnS (111) closely overlap,[58] and the only peak observed is in this region, indicating the films are oriented. The longitudinal optical (LO) modes of both phases also coincide, thus leaving phase identification somewhat ambiguous. The comparatively low growth temperature and modeling results suggest that the films are in the zincblende structure. However, low temperature resonant Raman scattering results presented in Section 6.2.3.d suggest that the films may have a small wurtzite component. No ZnO phases were detected in XRD or Raman measurements.The composition of the films (S/Zn ratio) was determined by Rutherford backscattering spectrometry (RBS) and energy dispersive X-ray spectroscopy (EDS). RBS measurements were carried out using a 3.04 MeV He^{2+} beam at a backscattering angle of 165°. RBS data were analyzed using the SIMNRA software.[72] For consistency, presented spectra are labeled using compositions obtained by RBS. The sputtered films showed O concentrations of several percent, even when no oxygen was deliberately introduced. The lowest composition film, which was grown with a new ZnS target, showed a concentration of $x < 0.01$. We refer to this low-O content film as "ZnS." Samples grown with high O_2 flow (1% of the total) resulted in films with poor-quality XRD and Raman spectra, perhaps due to phase separation. From the difference between the RBS and EDS results (Table 6.1), we estimate the uncertainty in S/Zn to be ±0.03.

Sample label	$\omega_{\text{O-mode}}$ **(cm^{-1})**	**S/Zn by EDS**	**S/Zn by RBS**
ZnS	412	1.00	-
$ZnS_{0.98}O_{0.02}$	416	0.979	0.978
ZnS, low O	418	1.009	-
$ZnS_{0.98}O_{0.02}$ #2	418	0.905	0.979
$ZnS_{0.83}O_{0.17}$	440	0.878	0.828
$ZnS_{0.82}O_{0.18}$	448	0.755	0.820
$ZnS_{0.79}O_{0.21}$	455	0.702	0.792

Table 6.1: O-related mode frequencies with compositions measured by EDS and RBS. The sample labeled "ZnS, low O" is not plotted in Fig. 6.5

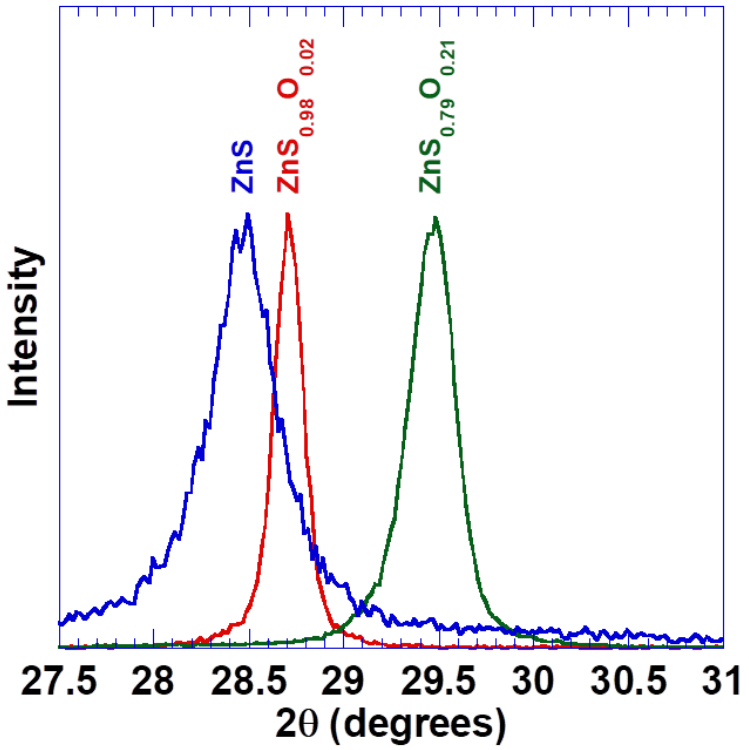

Figure 6.2: Representative XRD spectra of the films. The sample labeled ZnS has an estimated O concentration of x < 0.01 (Table 6.I).

6.2.3: Results

6.2.3.a: Room temperature Raman spectroscopy

Figure 6.3 shows a representative resonant Raman spectrum of ZnS and $ZnS_{0.98}O_{0.02}$ films at room temperature, with bulk single-crystal ZnS (Fairfield Crystal Technology) for comparison. The figure shows the harmonic LO modes of ZnS and a satellite mode near 412 and 416 cm^{-1} respectively. An additional set of satellite modes are observed 63-68 cm^{-1} above the higher order LO modes. The satellite modes are separated by the 1LO mode frequency. The satellite peaks do not appear in the bulk ZnS sample, indicating they are not intrinsic features.

Furthermore, while two-phonon modes may be present near 400 cm^{-1}, they cannot account for the higher frequency satellite bands near 761 and 1110 cm^{-1}. As discussed in the following section, the 412 cm^{-1} peak is attributed to an O-related mode.

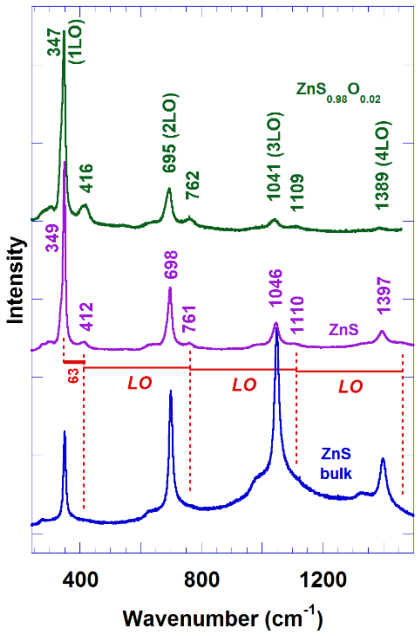

Figure 6.3: Resonant Raman spectrum of ZnS and $ZnS_{0.98}O_{0.02}$ films, with a bulk crystal for comparison. The films show the characteristic ZnS LO mode at 347 cm^{-1} and additional sidebands.

To understand the origin of the satellite bands at 761 and 1110 cm^{-1}, consider that the intensity of resonant Raman scattering is proportional to:[73]

$$I \propto \left[\sum_{i,j} \frac{1}{(E_i - \hbar\omega_l)(E_j - \hbar\omega_s)}\right]^2 \tag{6.1}$$

where the $E_{i,j}$ are electronic states and ω_l and ω_s are frequencies of the laser and scattered photons respectively. The satellite bands are observed to follow O-mode + *n*LO behavior (*n*=0,1,2). If the incoming photon ω_l scatters and excites the O-related mode, this scattered photon may still be in resonance with an electronic transition E_i.[72] For dilute O concentrations, the density of states for the LO mode is considerably larger than for the O-related mode.

Consequently, the photon will likely excite an LO mode. By energy conservation, this scattered photon will have an energy $\hbar\omega_{s2} = \hbar\omega_{l} - \hbar\omega_{O\text{-}mode} - \hbar\omega_{LO.}$ In other words, the observation of phonon replicas may be explained in terms of outgoing resonant behavior, where the scattered photon is itself in resonance with an electronic transition.[73,75]

6.2.3.b: Mass defect models

To understand the origin of the satellite bands, a mass-defect model was constructed. The ZnS crystal was modeled using a linear chain of 256 atoms with periodic boundary conditions.[7] The force constant was adjusted to reproduce the observed LO mode frequency of ZnS. Thereafter a single O was substituted onto an S site and the vibrational frequency was calculated. The model gives the LVM frequency of substitutional O in ZnS as 433 cm^{-1}, close to the observed satellite peak value of 412 cm^{-1} (Fig. 6.3). Since the mass defect model does not account for anharmonicity or changes in the force constants, the ~20 cm^{-1} discrepancy between theory and experiment is reasonable. This model suggests that the 412 cm^{-1} band should be identified as a vibrational mode of O substituting on S sites in $ZnS_{1-x}O_x$. Using a similar model for ZnO, we estimate the gap mode frequency of S substituting on an O site as 323 cm^{-1}.

To investigate the O-related mode further, the ZnS crystal was simulated by a 216-atom three-dimensional cubic cell with periodic boundary conditions. Nearest neighbors interacted via stretching and bending force constants.[54] These two force constants were adjusted to simulate the ZnS phonon dispersion determined from neutron scattering experiments.[76] As shown in Figure 6.4, this model qualitatively reproduces the phonon frequency bands. An isolated O mass defect results in a LVM frequency of 436 cm^{-1}. As more O atoms are added randomly, pairs of next-nearest neighbors, and larger clusters, begin to form. This clustering results in a broadening

of the vibrational band (Fig. 6.4), in agreement with experiment. The mass-defect model does not, however, account for the increase in the LO frequency due to the electronegativity of the O atoms. This effect is treated by the MREI model, discussed next.

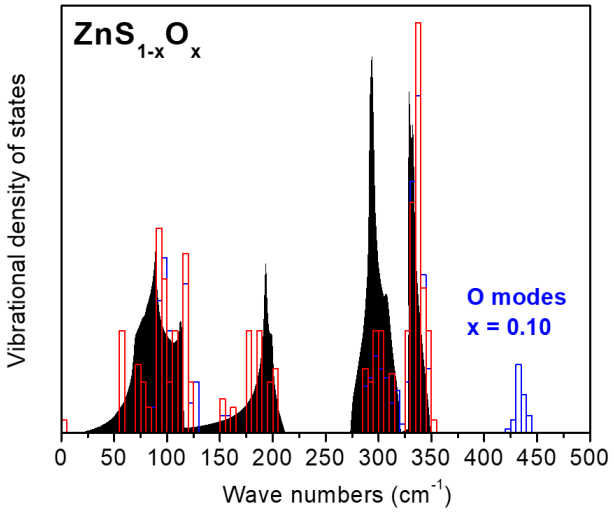

Figure 6.4: Vibrational density of states calculated for ZnS (red bars). The experimental phonon density of states is shown in black. The calculated O modes are shown for a crystal with 10% of the S atoms randomly replaced by O (mass defects).

6.2.3.c Composition dependence

Figure 6.5 presents resonant Raman spectra of $ZnS_{1-x}O_x$ films for various compositions. The O-related mode is observed to shift toward higher energy with increased O content of the films. The ZnS LO mode displays a shift to lower frequencies and decrease in intensity. The higher order ZnS LO and O-mode + *n*LO combination modes are rapidly suppressed with increasing O content.

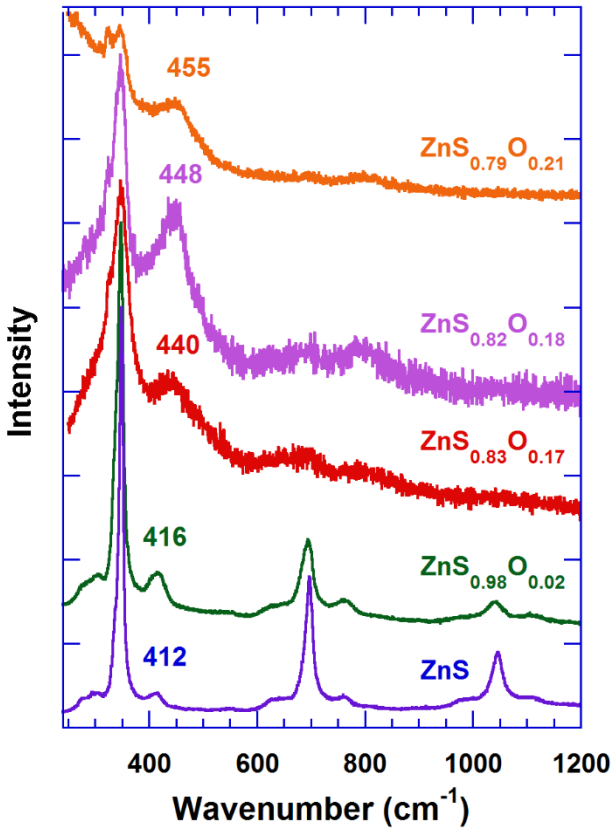

Figure 6.5: Representative resonant Raman spectra for $ZnS_{1-x}O_x$ alloy films at various compositions. The O-related mode is found to shift toward higher energies as predicted by the MREI model. The 1LO mode shows a shift to lower energies while broadening and decreasing in intensity. The sample labeled ZnS has an estimated O concentration of $x < 0.01$ (Table 6.1).

To understand the composition dependent behavior of the modes, we used the MREI model,[67] which gives a basic criterion for predicting the phonon behavior of alloy crystals. Consider an alloy AB_xC_{1-x} with masses m_A, m_B and m_C respectively, where $m_B < m_C$. Letting μ_{AC} be the reduced mass of elements A and C, then if:

$$m_B < \mu_{AC} \tag{6.2}$$

the alloy will follow "two mode" behavior, otherwise the alloy will display "one mode" behavior. If we let A = Zn, B = O and C = S, then we find that $ZnS_{1-x}O_x$ follows two mode behavior. Upon adding a small quantity of O to ZnS, an O related LVM forms. With increasing

O content, the LVM becomes delocalized and shifts in frequency until it reaches the LO mode of ZnO. In addition, the O mode splits into LO and TO modes, which shift toward their ZnO values with increased O content.

The MREI model requires knowledge of the high frequency dielectric constant ε_∞ for both end members. While the value of ε_∞ is known for ZnS,[77] there are no experimental reports for zincblende ZnO. The value has been calculated theoretically[78,79] but the density functional approach used underestimates the band gap and consequently overestimates ε_∞.[79] For the purposes of the model calculations, measured values of ε_∞ for wurtzite ZnO were compared to theoretical values and found to be overestimated by about 30%.[79] This overestimation was accounted for in the value of ε_∞ used for zincblende ZnO.

Table 6.2 presents the parameters used for the MREI model and relevant calculated parameters. The estimated value for ω_{gap} is reasonable as it falls in the predicted frequency gap for zincblende ZnO.[78] The force constants F and the interaction parameter θ were obtained by solving the following system of equations:[67]

$$\omega_{\mathrm{TO,AB}}^2 = \frac{F_{AB,0}}{\mu_{AB}} \tag{6.3}$$

$$\omega_{\mathrm{TO,AC}}^2 = \frac{F_{AC,0}}{\mu_{AC}}(1-\theta) \tag{6.4}$$

$$\omega_{\mathrm{gap}}^2 = \frac{F_{AC,0}+F_{BC,0}}{m_C} \tag{6.5}$$

$$\omega_{\mathrm{LVM}}^2 = \frac{F_{AB,0}+F_{BC,0}}{m_B}(1-\theta) \tag{6.6}$$

The oscillator strength $4\pi\rho_{\mathrm{AB}}$ was obtained using:

$$4\pi\rho_{AB} = \varepsilon_{\infty,AB}\left(\frac{\omega_{LO,AB}^2}{\omega_{TO,AB}^2} - 1\right) \tag{6.7}$$

with the equivalent expression for $4\pi\rho_{AC}$.

ZnO		**ZnS**		**Calculated**	
$\varepsilon_{\infty,AB}$	3.9	$\varepsilon_{\infty,AC}$	5.1	$F_{AB,0}$	219.25x10^4
$\omega_{LO,AB}$	568	$\omega_{LO,AC}$	347	$F_{AC,0}$	211.98x10^4
$\omega_{TO,AB}$	413	$\omega_{TO,AC}$	274	$F_{BC,0}$	137.20x10^4
ω_{gap}	330	ω_{LVM}	412	θ	0.23807
μ_{AB}	12.9	μ_{AC}	21.5	$4\pi\rho_{AB}$	3.477
				$4\pi\rho_{AC}$	3.075

Table 6.2: Parameters and calculated values used in the MREI model for zincblende $ZnS_{1-x}O_x$ presented in Figure 6.5. Notation convention follows that of reference 66, where AB is ZnO and AC is ZnS. Phonon frequency and dielectric constant values are based on references 75-77. The values of ω_{LVM} and ω_{gap} were estimated using the mass defect model and experimental data. The high frequency dielectric constant (ε_∞), phonon frequencies (ω_{LO}, ω_{TO}), reduced masses (μ), interatomic force constants (F), oscillator strengths ($4\pi\rho$) and interaction parameter (θ) are listed.

Figure 6.6 presents the phonon mode behavior obtained from the MREI model for zincblende $ZnS_{1-x}O_x$. The model reproduces the observed slight decrease in the ZnS LO mode and the shift in the O-related mode. The data points presented in Figure 6.6 show the composition for each sample as measured by RBS and EDS. No systematic differences between the measurement techniques were observed (Table 6.1).

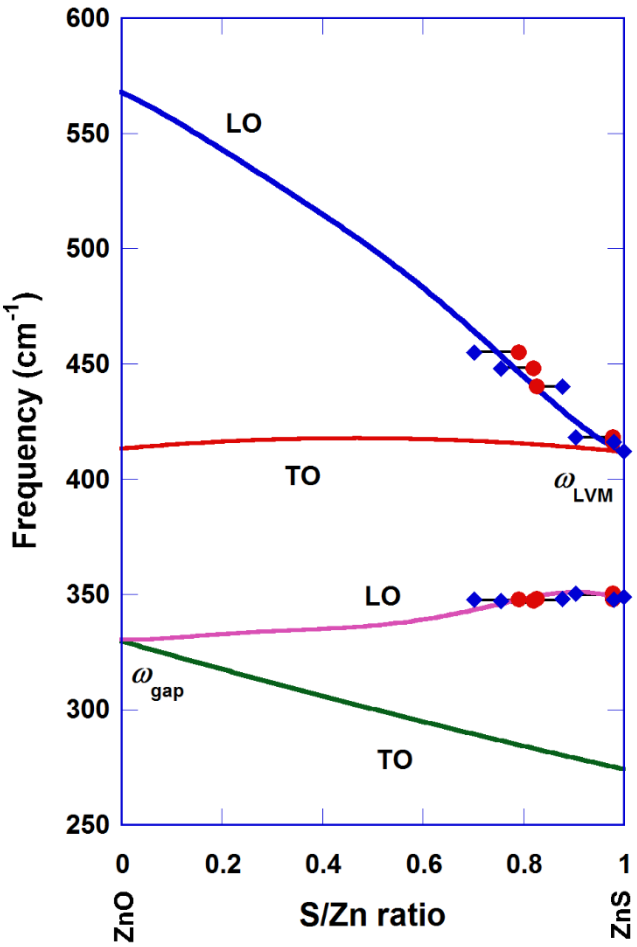

Figure 6.6: Phonon frequencies in zincblende $ZnS_{1-x}O_x$ as a function of the composition as predicted by the MREI model (solid lines). Diamonds and circles indicate the composition as measured by EDS and RBS, respectively. The bars indicate the estimated range of compositions for each sample.

Our results are different than those reported by Guc *et al.*, who found that the O-related mode shifts linearly with oxygen content[80] with an estimated frequency of 403 cm^{-1} at the dilute limit. One difference is that Guc *et al.* fit data over the entire composition range, which encompassed wurtzite and zincblende phases. Secondly, XPS is a surface sensitive measurement and may overestimate the bulk oxygen composition due to sulfur-poor surfaces.

6.2.3.d: Low temperature Raman spectroscopy

Low temperature Raman measurements were performed to further investigate the nature of the O-related mode. Figure 6.7 presents a representative Raman spectrum at 80 K. The vibrational band is found to be composed of two distinct modes at 405 and 416 cm^{-1} (406 and 420 cm^{-1}) for ZnS ($ZnS_{0.98}O_{0.02}$). At room temperature, thermal broadening obscures these features. Alloy broadening at high O compositions also washes out the features. The mode at 405 cm^{-1} is considerably lower energy than would be expected for the TO component (Fig. 6.6) and no reasonable model parameters are able to reproduce this frequency while still fitting the other data.

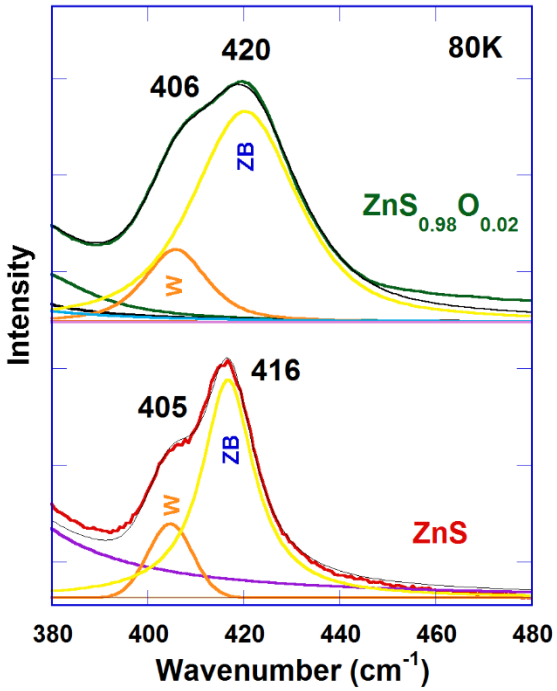

Figure 6.7: Low temperature Raman spectra of the O-related band for ZnS and $ZnS_{0.98}O_{0.02}$ films. The band is observed to be composed of two peaks. These peaks are attributed to modes associated with the wurtzite type and zincblende polytypes.

One possibility is that the mode at 405 cm^{-1} indicates the presence of a wurtzite component. Such detection is possible by resonant Raman scattering.[81–83] As can be seen from

Eqn. 6.1, if a material has regions with differing band gaps and the laser excitation is sufficiently near these electronic transitions, resonant Raman scattering may be observed from these regions even if the quantity of material is quite small. The band gap of zincblende ZnS is reported to be 3.7 eV[84,85] while wurtzite ZnS is reported slightly higher at 3.8-3.9 eV[85,86] and the laser excitation is 3.81 eV. The laser excitation is very close to resonance with both ZnS polytypes, and by Eqn. 6.1 both phases could be detectable simultaneously.

ZnS is known to exhibit polytypism similar to that of SiC with numerous degrees of hexagonality and the transition between polytypes occurring at stacking faults.[87,88] Furthermore studies of nanocrystalline $ZnS_{1-x}O_x$ have shown transitions between the zincblende and wurtzite structures[89] suggesting that both phases may coexist in the alloys to some degree. Thus, the 405 cm^{-1} mode may be attributable to O in a wurtzite type structure. Alternatively, this mode could arise from an O atom located at a stacking fault.

6.2.4: Conclusions

$ZnS_{1-x}O_x$ films were grown by reactive rf magnetron sputtering and studied via resonant Raman spectroscopy. Films with low O content were found to exhibit ZnS LO modes and additional modes attributed to an O-related mode and O-mode + *n*LO combination modes. The assignment of the modes was supported by mass-defect models. The $ZnS_{1-x}O_x$ alloy was modeled using the MREI model and it is found that $ZnS_{1-x}O_x$ follows two mode behavior, in agreement with experiment. The phonon frequencies predicted by the MREI model agree with experimental data. Low temperature resonant Raman measurements showed the O-related mode is composed of two features, which were attributed to zincblende and wurtzite type crystalline regions.

Acknowledgements

This work was supported by the US Department of Energy (DOE), Office of Science, Basic Energy Sciences (BES) under Award No. DE-FG02-07ER46386. KMY acknowledges the support of the General Research Fund of the Research Grants Council of Hong Kong SAR, China, under project number CityU 11303715. The authors thank John McCloy for providing the bulk ZnS sample.

6.3: High Order Oxygen Local Vibrational Modes in $ZnS_{1-x}O_x$

Jesse Huso[1], Jacob R. Ritter[1], Leah Bergman[2], Matthew D. McCluskey[1]

1. *Department of Physics and Astronomy, Washington State University, Pullman Washington 99164-2814*
2. *Department of Physics, University of Idaho, Moscow Idaho 83844-0903*

ABSTRACT

Substitution of O in the ZnS lattice is observed to result in a doublet consisting of two local vibrational modes (LVMs) and a second order harmonic of the LVMs. The first order doublet is attributed to vibrational modes of a defect with trigonal (C_{3v}) symmetry. The results of temperature dependent resonant Raman scattering and anti-Stokes scattering support this assignment. The substitution of O in the lattice also leads to the presence of LVM+LO combination modes, which are interpreted in terms of the cascade model and resonance effects.

6.3.1: Introduction

The oxide-chalcogenide alloy zinc oxysulfide ($ZnS_{1-x}O_x$) presents a number of properties of interest in optoelectronics. Both ZnS and ZnO have band gaps in the UV region, however the

alloy system displays large band gap bowing which may enable engineering of the band gap from the UV to the blue/green region of the electromagnetic spectrum.[55–58]

It has been shown that by adding O to ZnS the conduction band shifts to lower energies while the valence band remains at a nearly fixed energy up to about 50% O.[55] Above 50% O, the valence band shifts to lower energies while the conduction band remains at a nearly fixed energy. Consequently, a defect which is a deep acceptor in ZnO may be a shallow acceptor in ZnSxO1-x for some appropriate alloy composition. Thus, by raising the valence band, the alloy band gap bowing could lead to successful *p*-type doping of ZnO-compatible materials. In addition, the ZnS1-xOx alloy has been proposed as a possible alternative buffer layer in chalcopyrite based solar cells which removes the toxic Cd content.[90,91]

Aside from the properties of $ZnS_{1-x}O_x$ alloys, oxygen is also a common contaminant in ZnS crystals[59] and rapid detection of low levels of substitutional O is desirable. In this work, we report composition-dependent resonant Raman scattering measurements of $ZnS_{1-x}O_x$ films grown by reactive radio frequency (rf) magnetron sputtering and compare with ZnS bulk crystal implanted with oxygen. We also demonstrate that resonant Raman scattering can be a highly sensitive probe for the presence of substitutional oxygen in the ZnS lattice.

6.3.2: Experimental

Thin film samples were grown using rf magnetron sputtering on Al_2O_3 (0001) substrates. The details of the growth process and composition measurements have been reported elsewhere.[92] The bulk crystal is (111) oriented zincblende ZnS from Fairfield Crystal. A portion of the bulk sample was implanted with O^+ ions to study the impact of oxygen on the crystal lattice. To achieve a uniform O concentration three implantations were performed. The ion

fluences were $5x10^{14}$ cm^{-2} at 40 keV, $1x10^{15}$ cm^{-2} at 100 keV and $1x10^{15}$ cm^{-2} at 180 keV. To remove radiation damage the implanted crystal was sealed in a silica ampoule which had been repeatedly purged with argon and evacuated to a final pressure of ~10^{-4} Torr. The implanted crystal was then annealed at 200 °C for 2 hours.

The sample herein referred to as $ZnS_{0.99}O_{0.01}$ has a O content below the detection limit of Rutherford backscattering spectroscopy (RBS). To accurately determine the concentration of O in the low O content sample secondary ion mass spectroscopy (SIMS) was performed. The implanted ZnS bulk was used as a reference standard. The lowest O film was found by SIMS to have composition $ZnS_{0.99}O_{0.01}$ while the implanted crystal had an O content of ~0.24%. Further details are discussed in Section 6.6.5.

Resonant Raman scattering (RRS) measurements were performed using a Horiba T64000 micro Raman/PL system using 325 nm laser excitation. Temperature dependent measurements were performed using an Instec 621V temperature stage modified for UV measurements.

6.3.3: Structure of the thin films

A parameter of considerable importance in interpreting the Raman results below is determination of the structure of the thin films. ZnS has two main phases, the zincblende and wurtzite and the films may grow in either structure. While differentiating these structures is straightforward in principle there are a number of complications that make the present case difficult. In general, one could use Raman or X-ray diffraction measurements to determine the structure. In the case of Raman there is considerable overlap between the phonon modes of the wurtzite and zincblende structures, In addition the presence of second order modes and appearance of defect related modes can further complicate structure identification. In addition

alloy effects may shift mode positions from reference values calling peak assignments into question. Similar issues impact X-ray diffraction measurements. Due to the films being oriented, only a limited subset of diffraction peaks are available, all of which could be assigned to either the wurzite or zincblende structures. X-ray diffraction is also impacted by alloy effects further complicating structure identifcation. These factors all conspire to render phase identification of the films difficult.

For the present purposes, differentiating between the wurtzite and zincblende structures is the most important concern, and this distinction can be made by a close examination of the Raman spectra. There are a number of modes in the first order spectrum which could potentially belong to either polymorph. To differentiate the two structures, we first consider the frequency of the TO mode. One may use the Lyddane-Sachs-Teller relationship:[93]

$$\epsilon_0 = \epsilon_\infty \frac{\omega_{LO}^2}{\omega_{TO}^2} \tag{6.8}$$

to estimate the TO frequency. Using literature values for zincblende ZnS of ϵ_0 = 8.9 and ϵ_∞ = 5.7[94] and ω_{LO} = 351 cm^{-1} for $ZnS_{0.99}O_{0.01}$ we obtain $\omega_{TO} \approx 280$ cm^{-1}, very close to the mode observed at 278 cm^{-1}. A similar calculation for wurtzite ZnS (ϵ_0 = 9.6 and ϵ_∞ = 5.7)[95] yeilds $\omega_{TO} \approx 270$ cm^{-1} which is not particularly near any observed mode, though a very small peak could be present. We thus consider that the 278 cm^{-1} peak in $ZnS_{0.99}O_{0.01}$ should be identified with the TO mode of a zincblende film, similar to the values for pure zincblende ZnS from literature.[88,96] Besides the LO and TO modes, there are additional modes present in the film, particularly at 208 and 308 cm^{-1}. There is some disagreement in literature over the identities of these remaining modes but in general they should be considered as resulting from second order scattering processes.[88,96,97] In support of this identification we note that in general second order processes

have different temperaure dependence than first order processes.[97] In particular, the intensity of a first order process can have temperature dependence going as $(1+n_i)$, where $n_i = (exp(E_i/k_BT) - 1)^{-1}$ is the phonon occupation number and E_i is the energy of the created phonon and k_B and T are the Boltzmann constant and temperature respectively. A second order process will have different temperature dependence, such as $(1+n_i)(1+n_j)$ for sum modes and $(1+n_i)n_j$ for difference modes.[97] Thus, the temperature dependence of the different modes indicates their nature. In the present instance both the 208 and 308 cm^{-1} modes show different temperature dependence than the LO and TO modes, indicating that they result from second order processes. While it is not the focus of this work to conclusively identifiy the nature of these second order modes we note that the above discussion suggests the 208 and 308 cm^{-1}peaks are likely to be sum modes instead of difference modes due to their presence even at low temperatures. We may thus reasonably state that the films are predominantly zincblende.[88,98] However, due to the considerable overlap between the Raman modes and the known polytypism of ZnS,[87–89] a minimal wurtzite component cannot be completely ruled out.

6.3.4: Resonant Raman scattering

Figure 6.8 shows resonant Raman scattering of $ZnS_{1-x}O_x$ thin films at 80 K with a bulk zincblende ZnS crystal for comparison. All materials display *n*LO harmonic modes (*n*=1,2,3…). For $ZnS_{1-x}O_x$ additional peaks appear near ~412 cm^{-1} which are attributed to local vibrational modes (LVMs) caused by substitution of the O on the S site in the lattice.[92] Because O is lighter than S, substitutional O impurities (O_S) have a local vibrational mode (LVM), an oscillation that is localized in frequency and real space.[62] An LVM gives rise to sharp peaks in Raman spectra and involves localized motion of the impurity atom and a only few neighbors. Additional peaks

at energies given by LVM+*n*LO (*n*=1,2…) also appear. The origin of these peaks is discussed in Section 9.

Figure 6.8: Resonant Raman spectra of $ZnS_{1-x}O_x$ films with ZnS bulk for comparison. The substitution of O for S in the lattice leads to the appearance of a LVM. In addition, LVM+nLO (n=1,2…) combination modes appear as well. The origin of the combination modes is discussed in Section 7.

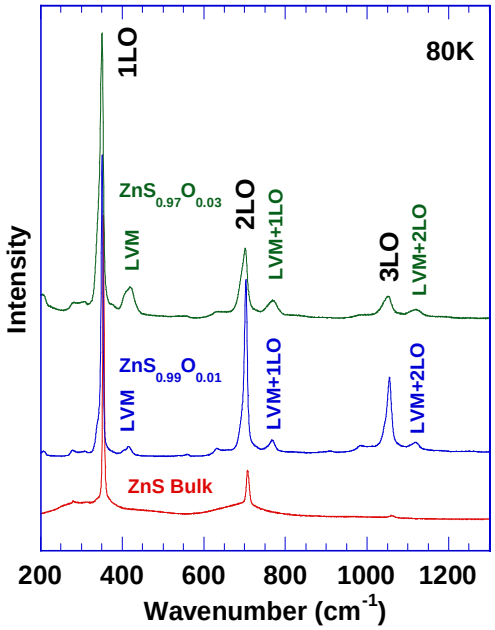

Figure 6.9a shows a detail of the $ZnS_{0.99}O_{0.01}$ sample at 80 K with the bulk for comparison. The LVM peak is actually composed of 2 overlapping peaks at 416 and 406 cm^{-1} (Figure 6.9b). These peaks are referred to as the LVM_{high} and LVM_{low}. In addition, a small peak at 822 cm^{-1} is observed as well as a weak peak at 1173 cm^{-1}, which is exactly 1LO above the 822 cm^{-1} line. Based on the peak positions, these peaks are assigned as the second harmonic of the LVM (2LVM) and 2LVM+1LO modes respectively. Further discussion of these modes is found in sections 6.3.6-6.3.8.

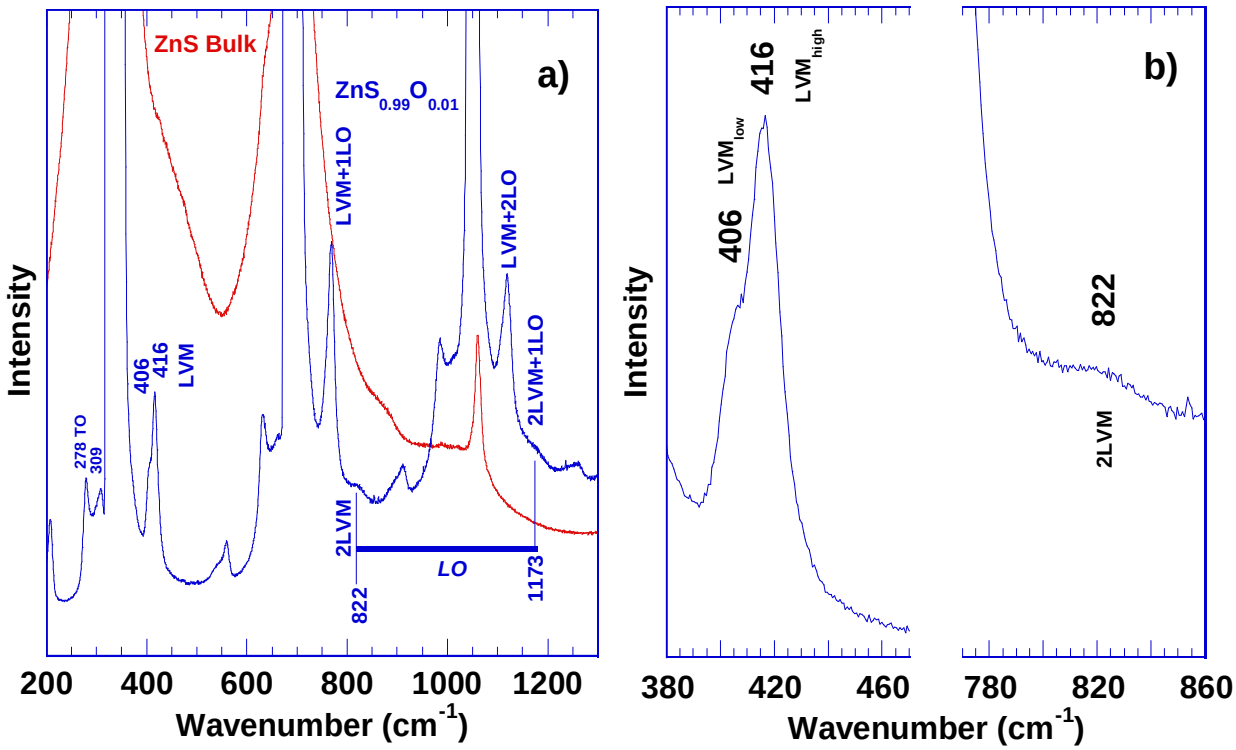

Figure 6.9: a) Raman spectra of the $ZnS_{0.99}O_{0.01}$ film at 80K with bulk ZnS for comparison. The LVM mode is observed to be composed of two peaks with LVM+nLO combination modes appearing at higher energies. In addition a small peak at 822 cm^{-1} appears at low O concentration. Significantly, this feature is not a result of a combination with an LO phonon since no feature appears near 472 cm^{-1} where such a peak would be expected. An additional weak feature at 1173 cm^{-1} corresponds closely with the energy expected for a 2LVM+1LO combination. No features equivalent to the LVM, LVM+nLO, 2LVM or 2LVM+1LO modes appear in the bulk crystal. b) Detail of the $ZnS_{0.99}O_{0.01}$ sample at 80K showing the 416 (LVM_{high}), 406 (LVM_{low}) and 822 cm^{-1} (2LVM) peaks.

6.3.5: Oxygen implantation

As noted in Section 6.3.2, the O content in the $ZnS_{0.99}O_{0.01}$ films is below the detection limit of RBS. For compostion reference a bulk ZnS crystal was implanted with a known amount of oxygen and annealed to remove radiation damage. The compositions of the implanted sample and the $ZnS_{0.99}O_{0.01}$ sample were measured using SIMS (Fig 6.10). The SIMS results indicate that the O-implanted region of the ZnS crystal contains ~0.24% O, and the film is $ZnS_{0.99}O_{0.01}$. The SIMS results indicate that the $ZnS_{0.99}O_{0.01}$ film should be considered ZnS with light O doping. Figure 6.11 shows Raman scattering measurements for implanted and sample compared

to $ZnS_{0.99}O_{0.01}$ film. It is clear that the introduction of O into the lattice of ZnS bulk creates an LVM closely corresponding to the $ZnS_{0.99}O_{0.01}$ film (Fig. 6.11 b,c). Furthermore, the LO modes of the implanted sample also shift to lower frequency relative to the unimplanted sample (Table 6.3) in accordance with the behavior expected for a "two mode" system (Section 6.3.6). The LVM+1LO mode is also observed in the implanted sample (Figure 6.11b), closely corresponding to the equivalent mode in the $ZnS_{0.99}O_{0.01}$ film. Thus, we can state positively that the LVM is due to oxygen impurities and that resonant Raman scattering is a highly sensitive probe for detecting the presence of O_S in the lattice.

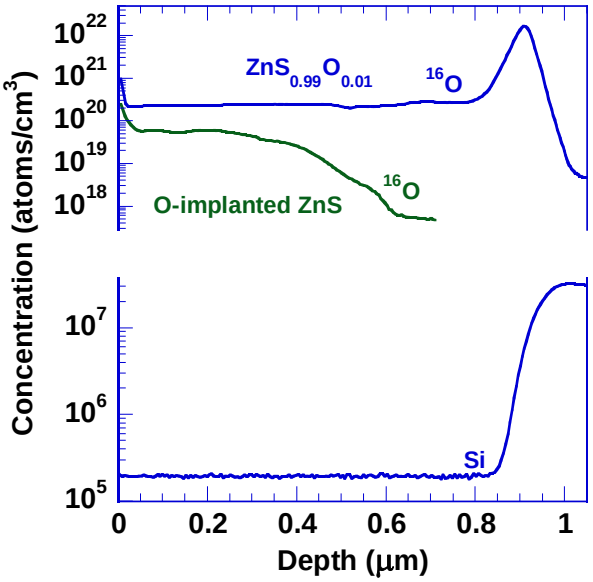

Figure 6.10: SIMS measurements of O-implanted ZnS bulk (green) and $ZnS_{0.99}O_{0.01}$ film on Si (blue). The implanted sample is found to have 0.24% O in the implanted region. The peak in O content for $ZnS_{0.99}O_{0.01}$ around 0.9 μm is attributed to an oxide surface layer. The raw Si count is included as a reference.

An additional small feature at 473 cm^{-1} appears in the implanted sample which has no analogue in any other sample. The feature is also not near any second order scattering peak in ZnS. We tentatively attribute this feature to an unidentified defect resulting from radiation damage.

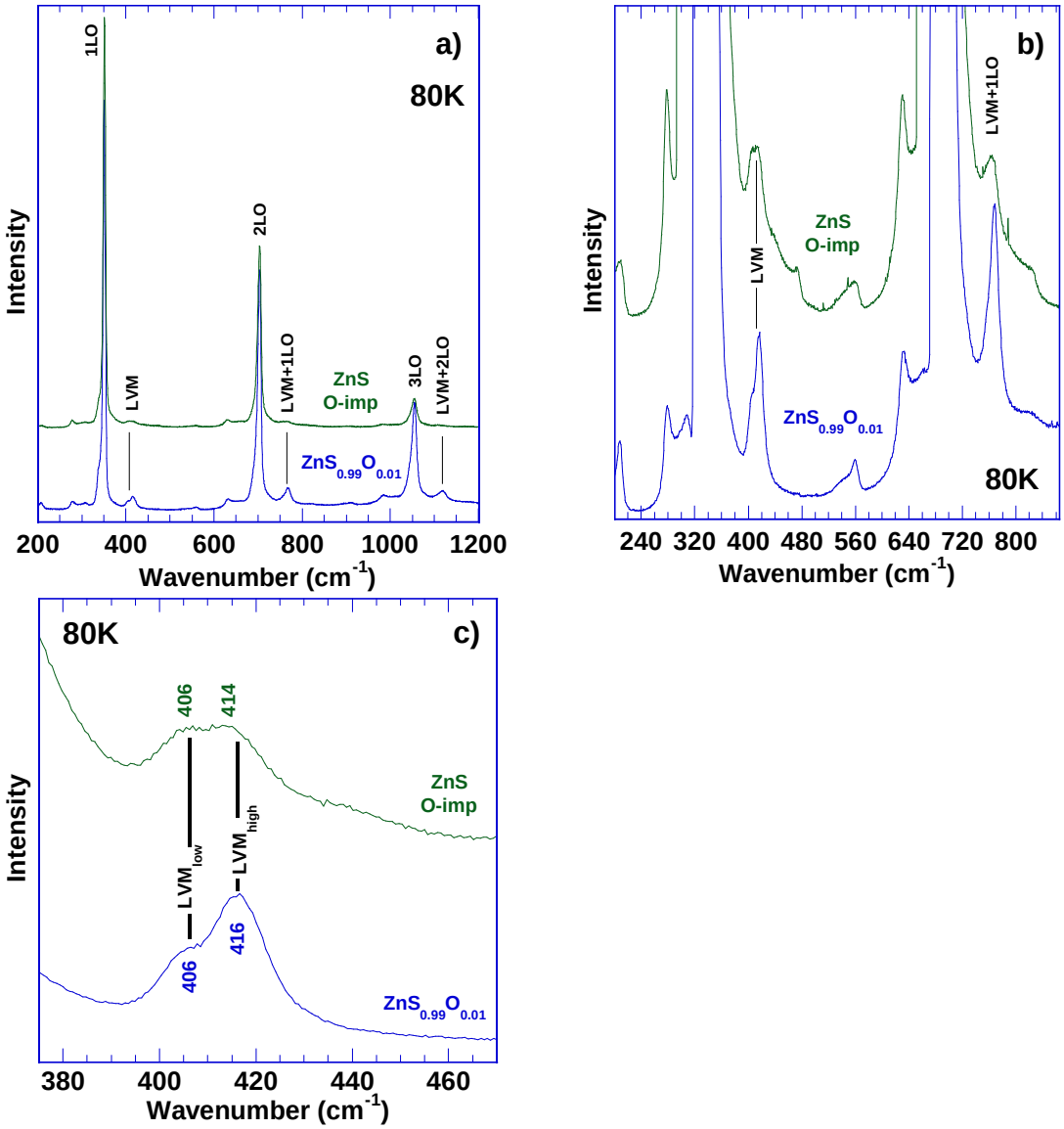

Figure 6.11: a) Resonant Raman spectra of O-implanted ZnS with $ZnS_{0.99}O_{0.01}$ film for comparison. b) Detail of the spectra from (a). c) Comparison of the LVM in the O-implanted ZnS and $ZnS_{0.99}O_{0.01}$. The implanted ZnS clearly shows the appearance of the LVM and LVM+LO modes which are not present in unmodified ZnS. These new peaks correspond closely to the LVM and related modes found in the $ZnS_{0.99}O_{0.01}$ film. The doublet observed in the LVM of $ZnS_{0.99}O_{0.01}$ is also present in the O-implanted ZnS with a small frequency shift consistent with the lower O content of the implanted crystal, though differing relative intensities. The O-implanted ZnS also shows a shift in the LO modes corresponding to the behavior expected for a "two mode" system in very close agreement with the results from thin films (Table 6.3).

Mode Assignment	**ZnS Bulk**	**ZnS imp.**	**$ZnS_{0.99}O_{0.01}$**	**$ZnS_{0.97}O_{0.03}$**
2TA[88]	-	209	208	205
TO[88,96]	280	278	278	280
TA+LA[88]	~313	307	308	307
LO[88,97]	354	351	351	350
LVM_{low}	-	406	406	410
LVM_{high}	-	414	416	420
Unknown	-	473	-	-
2TA+LO	-	559	560	555
TO+LO[97]	~638	631	632	635
2LO[88]	707	703	703	701
LVM_{low}+LO	-	~763	~758	~756
LVM_{high}+LO	-	~767	768	770
2LVM	-	824	822	830
2TA+2LO	-	908	911	~906
TO+2LO	~988	983	986	986
3LO	1061	1055	1055	1052
LVM_{low}+2LO	-	~1106	~1109	~1110
LVM_{high}+2LO	-	~1112	1120	1120
2LVM+LO	-	1173	1173	1185

Table 6.3: Mode assignment and frequencies observed in the samples discussed in this paper. The principle modes are listed in bold. All values are at 80 K. The increased number of modes seen in the films compared to the bulk is attributed to a breakdown of translational symmetry by doping combined with the effects of the exciton bound to the O_S site. The O-implanted ZnS bulk and $ZnS_{0.99}O_{0.01}$ film are very similar. All values are in wavenumbers.

6.3.6: Composition dependence

As shown above the $ZnS_{0.99}O_{0.01}$ sample has very low oxygen concentration it should be considered as exhibiting the true local vibrational mode for O_S in ZnS. That is, the behavior of

the LVM is nearly unencumbered by modifications due to next-nearest neighbor O atoms. However, with increasing O content the $ZnS_{1-x}O_x$ alloy system is predicted by the modified random element isodisplacement model to exhibit "two mode" behavior,[92,99] in agreement with experiment.[80,92] That is, the peak position of the LVM will shift to higher energies with increasing O content, similar to findings in other alloy systems.[66,92,100,101] In addition the LO phonon frequency will shift to lower energy, though at a different rate than the LVM. By examination of composition dependence of the films additional information regarding peak identities can be extracted.

Figure 6.12 shows RRS spectra of films with differing O contents. The LVM+*n*LO modes are still present, with the LO mode and overtones shifted according to predictions. In addition the $ZnS_{0.97}O_{0.03}$ film also shows the 2LVM and 2LVM+1LO modes, though weakly. The observed shift from the LVM of $ZnS_{0.99}O_{0.01}$ to $ZnS_{0.97}O_{0.03}$ is $\delta_{LVM} \approx 4$ cm^{-1}. The shift of the second harmonic is twice that of the first harmonic, $\delta_{2LVM} \approx 8$ cm$^{-1} = 2\delta_{LVM}$. This alloy shift strongly supports the identification of the 822 cm^{-1} peak in $ZnS_{0.99}O_{0.01}$ as the second harmonic of the LVM.

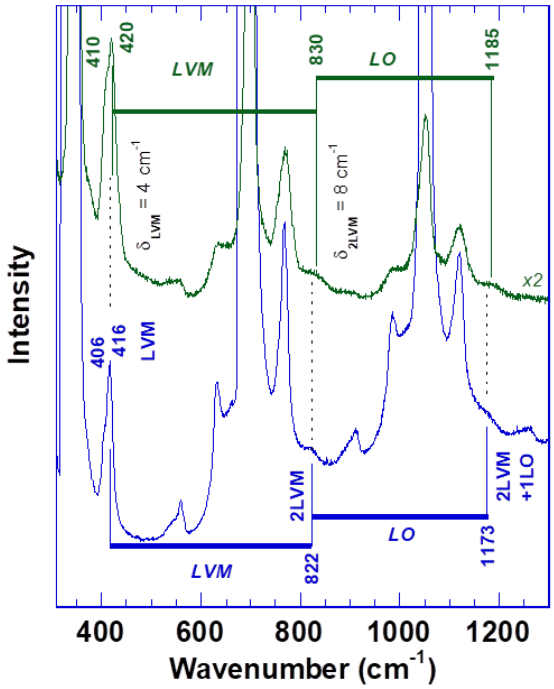

Figure 6.12: Detail of the resonant Raman spectra of $ZnS_{1-x}O_x$ films at 80K. The 2LVM peak is observed to shift with composition at a rate of twice that of the 1LVM mode ($\delta_{2LVM}=2\delta_{LVM}$). Accounting for the fact that the LO also shifts with composition, a weak additional peak appears 1LO above the 2LVM.

Furthermore, the 2LVM+1LO combination modes also exhibit the appropriate shift with composition after accounting for the change in LO frequency. Using the measured LO frequency for the sample leads to very close agreement on the observed peak position and expected energy for 2LVM+1LO modes as can be seen in Figure 6.12.

The case of O in ZnS is similar to the case of H interstitials in CaF_2[102] and closely analogous to C_{As} impurities in GaAs.[103] We note that because of the zincblende structure, the O atoms are tetrahedrally coordinated. Because the 2LVM mode is a transition from the ground state to the second excited state (0→2) one might expect to observe additional structure from transitions split by the point group symmetry of the defect.[102,103] In the present case no additional structure is observed, perhaps due to the low signal intensity of the 2LVM mode.

6.3.7: Local mode transitions

As noted above, Figure 6.9 demonstrates that the LVM is composed of 2 distinct modes at 416 (LVM_{high}) and 406 cm^{-1} (LVM_{low}) with an overtone at 822 cm^{-1} (2LVM). There is a relationship between these modes: specifically the energies are such that $2LVM-LVM_{high}=LVM_{low}$. This relationship holds even for increased oxygen concentration (Figure 6.12).

We consider three possible causes for the splitting of the LVM peak. First, LVM_{high} and LVM_{low} may be due to O_S in zincblende and wurtzite structures respectively. However, as noted in section 6.3.3, the data suggest that a wurtzite component, if present, is quite minimal. Thus it is not expected that the LVM_{low} would show such a comparatively strong intensity if it were due to O_S substitution within the wurtzite polymorph. In addition a peak corresponding to LVM_{low} also appears in the O-implanted zincblende ZnS which should not occur if LVM_{low} were due to a wurtzite component. A second possibility is the LVM_{low} may be due to a transition between the first and second excited state (i.e. $n=1 \rightarrow n=2$), with the LVM_{high} and 2LVM being the ground to first exicted state ($n=0 \rightarrow n=1$) and ground to second excited state ($n=0 \rightarrow n=2$) respectively. Transitions between the first and second excited state have been observed previously in for H interstitials in CaF_2[102] and C_{As} impurities in GaAs [103], and as noted above the present case could be considered as similar. A third possibility is that relaxation of O_S in the lattice results in a lowering of defect symmetry from T_d to C_{3v}. Such relaxation would lead to two distinct LVM frequencies, both 0→1 transitions. These last two possibilites will be discussed in the following section. Polarized resonant Raman measurements do not rule out either defect symmetry, and thus examination of the defects via temperature dependence is desirable.

6.3.8: Temperature dependence

6.3.8.a: Intensity ratios

To further understand the relationships of the LVM peaks, two types of temperature dependent measurements were performed. Firstly, the ratio of the integrated areas of the LVM_{low} and LVM_{high} peaks was determined as a function of temperature (Fig. 6.13). Fitting was performed using a Voigt profile and the ratio of the resulting areas was calculated. The fits were also manually verified to ensure validity, with satisfactory results. Secondly, anti-Stokes Raman scattering was performed and the anti-Stokes to Stokes intensity ratio was calculated. The anti-Stokes measurements are presented in Figure 6.14 and 6.15.

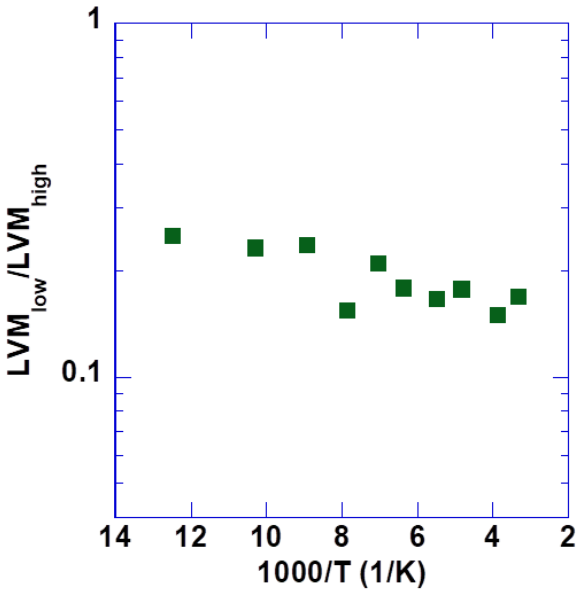

Figure 6.13: Arrhenius plot of the temperature dependence of the intensity of the 406 cm^{-1} peak (LVM_{low}) relative to the 416 cm^{-1} peak (LVM_{high}). It is clear from that the intensity ratio does not follow an expression like that of Equation 2 and thus LVM_{low} cannot be described solely in terms of thermally activated processes. It is also clear from that the intensity ratio is largely independent of temperature, with no obvious activation energy involved.

Figure 6.13 presents the results of the LVM_{low}/LVM_{high} intensity ratio as a function of temperature. If the LVM_{low} peak were due to a 1→2 transition it would be expected to be thermally activated and hence the intensity ratio should follow a function of the form:[103]

$$\frac{I(LVM_{low})}{I(LVM_{high})} = Ae^{-E_a/k_BT} \tag{6.9}$$

However, it is clear from Figure 6.13 that the intensities do *not* follow such a function. In light of these results, it is unlikely that the LVM_{low} peak is due to a 1→2 transition.

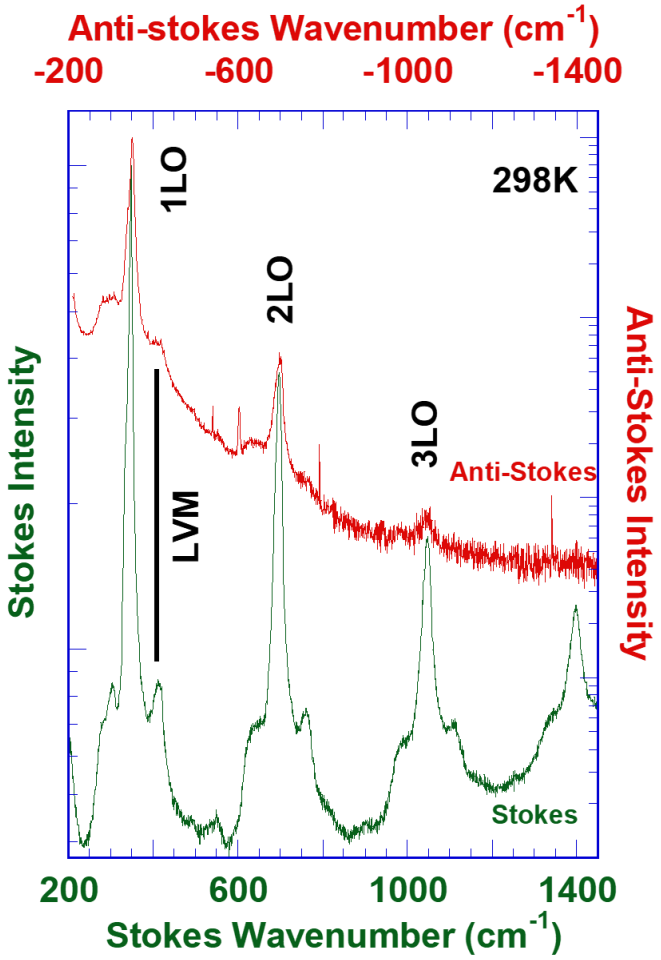

Figure 6.14: Representative Stokes and anti-Stokes resonant Raman spectra for $ZnS_{0.99}O_{0.01}$. The LVM is clearly visible as well as the 2LO and 3LO harmonics.

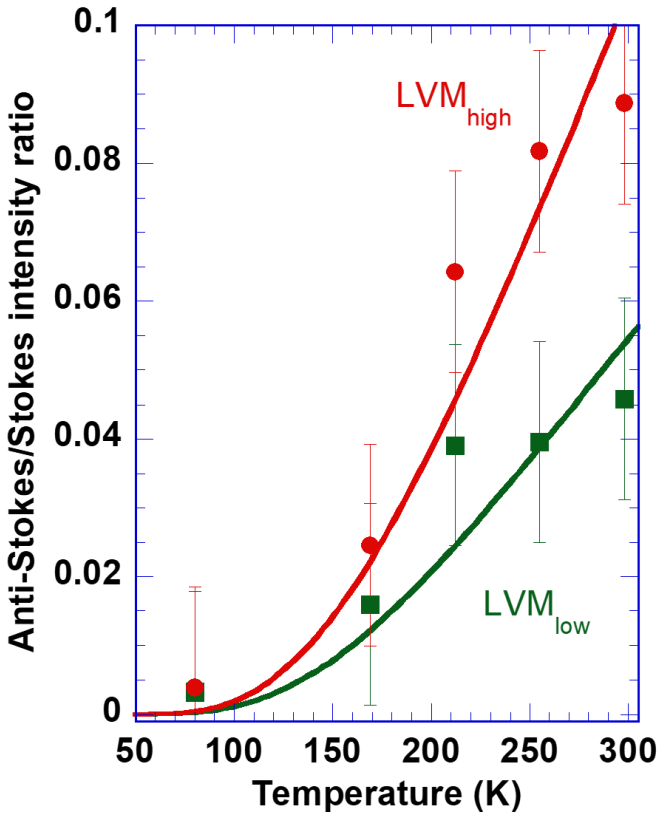

Figure 6.15: Anti-Stokes/Stokes intensity ratio for the LVM_{high} and LVM_{low} bands as a function of temperature. A fit to Equation 3 is included using the observed phonon energies. The LVM_{high} and LVM_{low} peaks follow the same trend, suggesting that both modes are 0→1 transitions rather than 1→2 transitions.

6.3.8.b: Anti-Stokes results

Our second set of temperature dependent measurements involve anti-Stokes scattering. Anti-Stokes scattering is desirable in this situation because the intensity of the anti-Stokes lines is directly related to the phonon population regardless of the source. Representative Stokes and anti-Stokes spectra are presented in Figure 6.14. Using a procedure similar to that described in Section 6.3.8.a, we simultaneously fit the $LVM_{low}^{anti\text{-}Stokes}$ and $LVM_{high}^{anti\text{-}Stokes}$ and LVM_{low}^{Stokes} and LVM_{high}^{Stokes} peaks as a function of temperature.

The anti-Stokes/Stokes intensity ratio follows a function of the form:[104]

$$\frac{I^{anti-Stokes}}{I^{Stokes}} = \frac{g_{ex}}{g_0} e^{-E_\omega/k_B T} \quad (6.10)$$

where g_0 and g_{ex} are the degeneracy of the ground state and excited states respectively and E_ω is the energy of the vibrational mode. To perform the fit, the observed vibrational mode energy was used for E_ω while g_0 and g_{ex} were free parameters. For the LVM_{high} peak it was found that $g_{ex}/g_0 \approx 1:1$ while for LVM_{low} $g_{ex}/g_0 \approx 1:3$. While there is considerable error in the data of Figure 6.14 due to the low intensities of some of the peaks, it is clear that both the LVM_{high} and LVM_{low} modes follow the same type of behavior. These results suggest that LVM_{high} and LVM_{low} should be considered as being separate vibrational modes with differing bond energies. This lends support to the hypothesis that both peaks arise from 0→1 transitions. Thus the observed 10 cm^{-1} splitting of the LVM suggests that the oxygen is not substitutional but rather off-center. Such a lowering of the symmetry would lift the degeneracy of the vibrational frequencies. If, for example, oxygen relaxes along a <111> direction then the symmetry goes from T_d to C_{3v}. In C_{3v} symmetry, the nondegenerate LVMs correspond to vibrations parallel and perpendicular to the <111> axis.

6.3.9: LO overtone generation

As can be seen from Figs. 6.8-6.11,6.14 numerous modes are observed in the films and nearly all the observed modes have replica overtones. Most of modes are not observed in bulk crystals under the same excitation conditions (Table 6.3). While the identity of the LVM+*n*LO modes is clear enough, the mechanism for generation of such overtones is not immediately obvious. Extensive examination of literature has revealed only one similar case in resonant scattering: that of CdS:Cl where the local mode and LO overtones were observed.[105] In our previous work[92] we found that the composition dependence of the LO and LVM modes can be

modeled using the modifed random element isodisplacement (MREI) model, but the origin of the LVM+*n*LO combinations was not explored beyond showing that they result from outgoing resonance. In addition the presence of the 2LVM+LO modes was not reported or explored. As will be shown though all of these modes can be explained within a single physical model.

The observation of the LVM modes and the LO overtones may be divided into two parts: first, why the LVM modes, and normally unobserved modes, appear at all even at very low O concentrations. Second, the mechanism for generating the LO overtones observed for nearly all modes.

To understand the observation of the modes not observed in bulk ZnS we first consider the scattering intensity of phonon modes under resonant conditions. As noted by Yu, for resonant conditions the scattering intensity P_{ph} may be written as:[74,106]

$$P_{ph} \approx \left(\frac{2\pi}{\hbar}\right)\left|\sum_{n,n'} \frac{\langle 0|\mathcal{H}_{eR}(\omega_i)|n\rangle\langle n|\mathcal{H}_{e-ion}|n'\rangle\langle n'|\mathcal{H}_{eR}(\omega_s)|0\rangle}{(E_n-\hbar\omega_i-i\Gamma_n)(E_{n'}-\hbar\omega_s-i\Gamma_{n'})}\right|^2 \tag{6.11}$$

where E_n is the energy of the n^{th} electronic transition, Γ_n is the damping of the n^{th} state, $\hbar\omega_i$ and $\hbar\omega_s$ are the energies of the incoming and scattered photons respectively, and $\mathcal{H}_{eR}$ and $\mathcal{H}_{e-ion}$ are the electron-radiation and electron-phonon Hamiltonians respectively. The above expression is derived using the observation that the interaction between an electron-hole pair (e.g. an exciton) strongly influences the scattering intensity. Thus, when the exciting laser energy is near an electronic transition, e.g. the band gap, the scattering intensity increases significantly. This is known as incoming resonance. Likewise, the scattered photon energy may also be near that of an electronic transition and also generate a large increase in scattering intensity, known as outgoing

resonance. It is important to note that Equation 4 *does not* assume interaction with any particular phonon mode, e.g. LO, TO etc.

In the case of an exciton bound at an impurity site, Equation 6.11 becomes:[74,107]

$$P_{ph} \approx \left(\frac{2\pi}{\hbar^2}\right)\left|\frac{\langle 0|\mathcal{H}_{eR}(\omega_i)|b\rangle\langle b|\mathcal{H}_{e-ion}|b\rangle\langle b|\mathcal{H}_{eR}(\omega_s)|0\rangle}{(E_b-\hbar\omega_i-i\Gamma_b)(E_b-\hbar\omega_s-i\Gamma_0)}\right|^2 \quad (6.12)$$

where E_b is the energy of the bound exciton, Γ_b the damping of the exciton, ($\Gamma_b \ll E_b$) and $|b\rangle$ is the state of the bound exciton, assumed to be in the 1*s* state. Similarly to Equation 6.11, if either the incoming or scattered photon has energy near the energy of the bound exciton, a large increase in scattering intensity will result. This phenomenon is the physical reason that the LVM can be detected in ZnS even at low O concentrations. RRS is therefore highly sensitive probe for the presence of O in ZnS, similar to the case of CdS:Cl.[74,107]

We also note that several phonon modes are observed in $ZnS_{1-x}O_x$ but not in bulk ZnS. The introduction of impurities in semiconductor alloys may nullify the one-phonon selection rules by disruption of translational symmetry. Thus, modes that would normally be forbidden can be observed. Such observation of normally forbidden first order modes has been previously seen for MgO,[108] metal impurities in NaCl[109–111] and potassium halides[112], and thermally induced defects in NaCl.[113] We thus attribute the presence of the modes seen in the $ZnS_{1-x}O_x$ films but not found in the ZnS bulk to the breakdown of translational symmetry of the crystal by introduction of O_S.

We now turn our attention to the existence of the *n*LO and LVM+*n*LO combinations. There are several possibilities for a physical model of the resonant spectrum observed in Figs 6.8-6.11. In particular, one could consider sequential scattering events where an incident photon

undergoes scattering, the scattered photon then undergoes scattering again, *etc*. A second possibility is that a single incident photon may excite *n* phonons in a single event. However, neither of these possibilities can reproduce the observed intensity patterns[114] seen in many semiconductors. A different model was proposed by Martin and Varma,[114] known as the cascade model. The model was later examined theoretically by Zeyher.[115] We here consider the observed spectra in terms of the cascade model.

In the cascade model, an exciton is created in an excited state by absorption of the incoming photon.[74,114,115] This creation process requires emission of a phonon to conserve wavevector (LO in the case of a free exciton). This exciton relaxes through emission of LO phonons until the electron and hole recombine and emit a photon. Importantly, due to the different physics involved in the creation process compared to the relaxation process, the inital vibrational mode need not be the same type as the phonons emitted during relaxation.

We thus propose that the presence of the LVM+*n*LO and 2LVM+1LO modes are due to creation of an exciton bound to an oxygen impurity. The virtual state decays by an LVM mode rather than an LO phonon (Fig. 6.16). This process is particularly relevant when the electron interacts strongly with the impurity, such as the case of O in ZnS, where O is considerably more electronegative than Zn or S. Impurity modes can have 'giant oscillator strength',[74] which results in significant increase in the scattering cross section.[115] This results in strong peaks even for low impurity concentrations.

Thus we note that the LVM modes are the result of the virtual state interaction during the creation of the exciton (Fig. 6.16), with the comparatively strong intensity caused by the resonance condition described in Equation 6.12. Furthermore even under resonant conditions one

typically does not observe more than 2nd or 3rd order peaks when there is no cascade process involved.[74,115] Thus, we should also identify the presence of the 2LVM mode as a result of the same processes but under resonant conditions. Consequently we propose that the LVM_{high}, LVM_{low} and 2LVM peaks should be identified as due to the inital vibrational mode excited during creation of a bound exciton, and the LVM+*n*LO and 2LVM+1LO overtones as resulting from the relaxation of the exciton through LO phonon emission (Fig. 6.16).

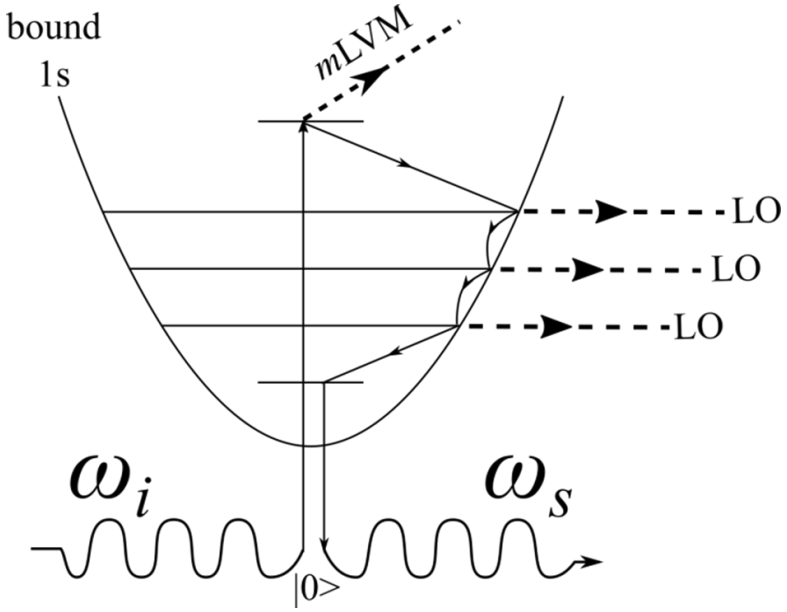

Figure 6.16: Diagram of the proposed cascade process for an impurity bound exciton. An incoming photon ω_i excites an exciton bound to an impurity and an LVM via scattering from virtual states. The exciton relaxes from an exited state via LO phonon emission as in the conventional cascade process, eventually recombining and emitting a photon $\omega_s = \omega_i$–mLVM-nLO, m = 1,2, n=1,2…

6.3.10: Conclusions

In light of the above results of intensity ratios between LVM_{low} and LVM_{high} combined with the anti-Stokes scattering results, we attribute the LVM_{high} and LVM_{low} to the O_S having C_{3v} symmetry. The observation of the second order LVM of O_S in ZnS has been reported for the first

time and its identity confirmed through composition dependence, the presence of LO overtones and peak position. The existence of the LO overtones of the LVM modes can be understood through detailed examination of the cascade model and resonant scattering effects.

Acknowledgements

This work was supported by the US Department of Energy (DOE), Office of Science, Basic Energy Sciences (BES), Division of Materials Science and Engineering under Award No. DE-FG02-07ER46386. The authors thank John McCloy for providing the bulk ZnS sample and Jeff Beeman for ion implantation.

CHAPTER SEVEN: PYRENE SURFACE EFFECTS

7.1: Mystery PL peaks: Pyrene

In the process of investigating the PL spectra for ZnS and ZnS_xO_{1-x} thin films, we discovered an interesting but problematic phenomenon. Our low temperature PL spectra were producing a signal that wasn't present in the room-temperature PL before, but sometimes showed up at room temperature afterwards. The spectra presented as a series of peaks from 373 nm to 405 nm. In an unfortunate coincidence the band gap for ZnO is ~370 nm, which misled me into believing that the mystery peaks were related to the sample we were growing for some time. Initial experiments taking PL scans from room temperature to 10 K strengthened the peak (Fig. 7.1), leading us to believe that our material potentially had some luminescent feature with a temperature dependence. Shortly we discovered that leaving the sample in vacuum for long periods of time would even more drastically give this feature (Fig. 7.2). In other words, it wasn't the temperature that was causing it but rather the amount of time the sample spent in vacuum.

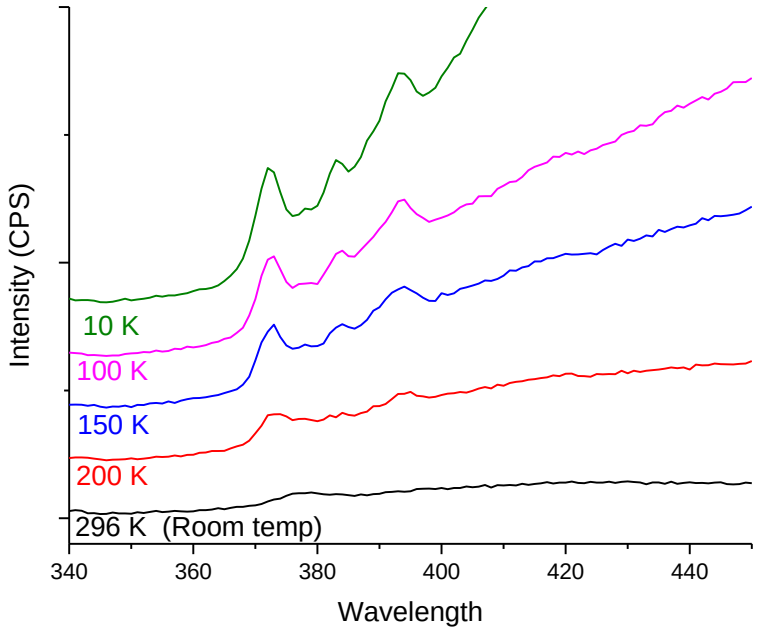

Figure 7.1: PL spectra with 325 nm excitation for the mystery peak (later found to be a pyrene monomer) on a $ZnS_{.99}O_{.01}$ sputtered thin film under a range of temperatures.

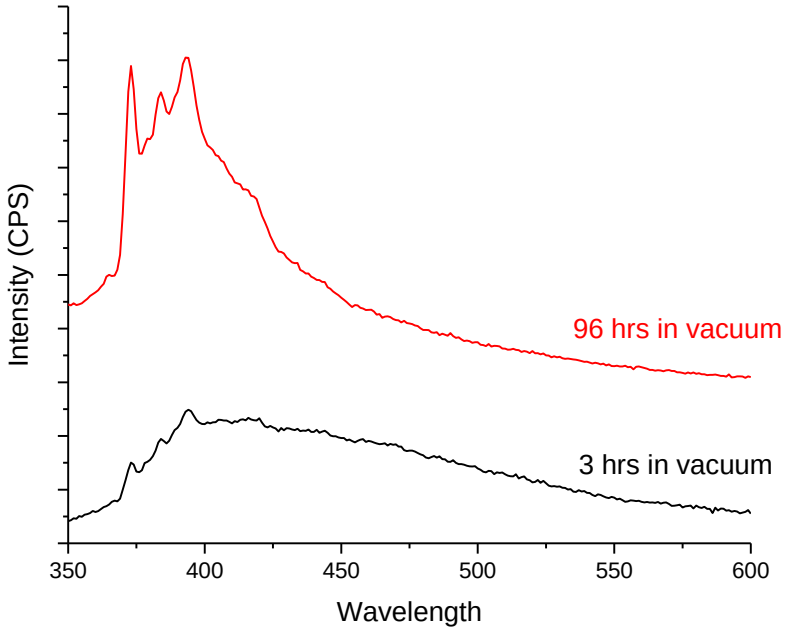

Figure 7.2: PL spectra with 325 nm excitation for the mystery peak (later found to be a pyrene monomer) on a $ZnS_{.99}O_{.01}$ sputtered thin film after first reaching 10 K (black) and left at 10 K for 96 hours in vacuum (red)

Eventually, after we were unable to convincingly connect this feature to any facet of our grown ZnS and ZnO materials, we decided the luminescence must come from something else. Searching the literature for similar spectra, we discovered that this spectrum, while not familiar to us, was well known in the field of organic chemistry. What we were seeing was a perfect match for the spectrum of pyrene (Fig. 7.3). A detailed explanation of the pyrene molecule and its luminescent characteristics are discussed in the second half of this chapter.

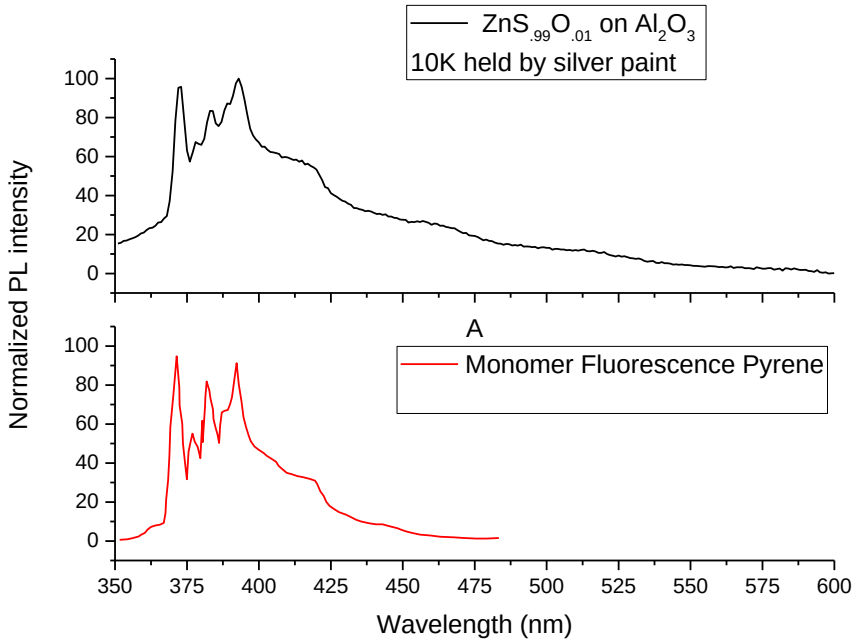

Figure 7.3: Comparison of PL spectra for our $ZnS_{.99}O_{.01}$ sample and the luminescence of pyrene as given by Uddin et. al.[116]

So where was the pyrene coming from? Up to this point we had been mounting our samples by adhering them to the brass holder with a silver paint from Structure Probe, Inc (SPI). Neither the paint nor the holder has any luminescence in the energy range under investigation and were not in the direct path of the excitation, so we did not anticipate any problems from the setup. As it turns out, a binding agent in silver paint outgasses the pyrene molecule in significant

quantities under strong enough (10^{-5} mbar) vacuum. This was demonstrated by placing several different material substrates in a vacuum chamber, placing a silicon wafer with dried silver paint on the other side of the chamber several inches away, and pulling vacuum. The vacuum causes the silver paint to outgas pyrene, which condenses on all of the surfaces in the chamber, and results in pyrene PL emission on every surface (Fig. 7.4).

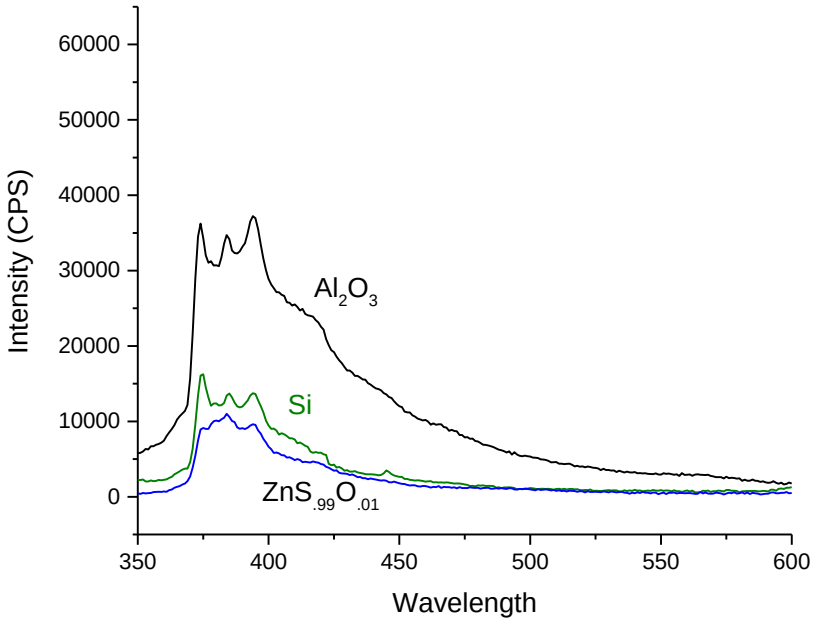

Figure 7.4: 325 nm excitation PL spectra for $ZnS_{.99}O_{.01}$, Si, and Al_2O_3 that have been vacuum exposed to dried silver paint for 80 hrs.

This final confirmation served two roles. First, for future research it is important to know the flaws associated with exposing silver paint to vacuum, and to use different methods for mounting low temperature samples in the PL system. Second, we observed that the luminescence spectra of pyrene when deposited on solid samples shows substrate dependence in

the PL and the absorption, the latter of which will be covered in depth in the remainder of the chapter.

7.2: Publication from Pyrene Findings

The following section is a paper in progress titled "Surface Effects on Pyrene Luminescence Excitation" that will not yet be submitted by the time of publication of this dissertation. Theoretical calculations in this paper and the corresponding sections were performed and written by collaborators Marilia J. Caldas and Tales J. da Silva at the University of Sao Paulo, Brazil and Arrigo Calzolari at the CNR-NANO Istituto Nanoscienze Centro in Italy.

Surface Effects on Pyrene Luminescence Excitation

Jacob R. Ritter,[1] Marilia J. Caldas,[2] , Tales J. da Silva[2], Arrigo Calzolari[3], and Matthew D. McCluskey[1]

[1]*Dept. of Physics and Astronomy, Washington State University, Pullman, WA 99164-2814*

[2]*Instituto de Física, Universidade de São Paulo, 05508-900 São Paulo, SP, Brazil*

[3] *CNR-NANO Istituto Nanoscienze Centro S3, I-41125 Modena, Italia*

ABSTRACT

Monomer pyrene absorption is sensitive to the surface on which it is deposited. Photoluminescence excitation (PLE) of pyrene's monomer emission shows that the ratio of the two absorption triplets in the UV is tied to the properties of the substrate. Calculations for pyrene on zinc sulfide (ZnS) and diamond substrates suggest this connection arises from the

position of the pyrene electronic levels relative to the valence band of the substrate. The absorption feature at 272 nm is shown to depend on the HOMO-1→LUMO orbital contribution and the feature at 335 nm depends upon the HOMO→LUMO transition. When the HOMO-1 level falls inside the substrate valence band, the 272 nm absorption feature is enhanced. Photoluminescence (PL) experiments also show a connection between emission strength and substrate selection.

7.2.1 Introduction

Pyrene ($C_{16}H_{10}$) is a polycyclic aromatic hydrocarbon (PAH) commonly created during the combustion of organic compounds.[117] Pyrene has unique absorption and emission characteristics that make it a useful fluorescent probe[118–120] and a building block for optoelectronic organic devices.[121–123] Pyrene luminescence consists of both excimer and monomer luminescence. In diluted solutions without excimers, pyrene presents a strong solution-dependent fluorescence. Monomer emission consists of 5 distinct peaks at 373, 378, 384, 389, and 393 nm. The highest energy of these is observed in polar solvents, while the third peak is solvent insensitive.[124,125] In this manner pyrene fluorescence is used to probe the polarity of solvents.[126,127]

In more concentrated solutions there is also an excimer emission; the ground-state dimer formation leads to a large band emission around 480 nm.[124,128,129] Figure 7.5 shows the effects of increasing pyrene concentration in an alcohol solution. Below 2×10^{-2} g/L there are no excimer emissions.

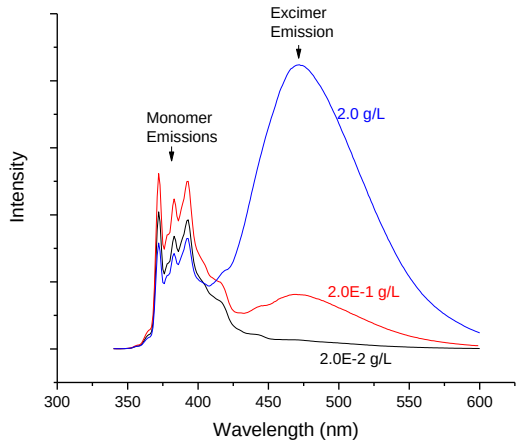

Figure 7.5: 325 nm excitation PL spectra for increasing concentrations of pyrene diluted in alcohol.

This work studies the absorption features that cause the leading monomer emission feature. To that end, pyrene is deposited in significantly low enough quantities in this work that excimers are not formed and no excimer emission is present.

7.2.2 Experimental methods

Pyrene powder (>99%) from Sigma Aldrich was deposited on a range of substrates using physical vapor deposition (PVD). The substrates were placed 2 cm from 0.1 g of pyrene powder and exposed to vacuum (10^{-5} mbar) for 4 hours. The full list of substrates investigated are shown in Table 7.1. Solutions of pyrene diluted in alcohol at concentrations between $2x10^{-2}$ g/L to $2x10^{-8}$ g/L were created to study the isolated pyrene case.

Substrate	272/335 nm
Al_2O_3	1.18
$SrTiO_3$	1.18
Diamond (optically pure)	1.24
Diamond (defective)	0.60
UV Fused Silica	1.14

Quartz	1.27
Glass (defective)	0.39
InSb	1.32
ZnS	1.64
Si	1.95
Thermal Oxide (1μm)	1.39
Thermal Oxide (300 nm)	1.70
Thermal Oxide (70 nm)	1.87

Table 7.1: Substrates for pyrene deposition and the ratio between absorbance peaks in PLE.

Photoluminescence (PL) and photoluminescence excitation (PLE) spectra were taken on a Horiba Jobin Yavon FluoroLog spectrometer. The source was a xenon lamp with excitation wavelengths 240-600 nm selected by passing the light through a monochromator. PL intensities were normalized to the excitation intensity, grating, and photomultiplier tube response. Samples were masked to a 3×3 mm hole to ensure similar levels of exposure. While PL spectra show emission across a range of wavelengths for a specific excitation, the PLE process observes light emitted for a specified wavelength and plots the intensity of this emission versus a range of excitation wavelengths. In this work we are studying the absorption features of the first peak in the pyrene monomer emission spectra shown in Fig. 7.5, i.e., the emission wavelength for PLE spectra in this paper is 373 nm.

7.2.3 Results (PL)

For the deposition conditions detailed in this work, pyrene is deposited in sufficiently low volume that only monomer emissions are present from all substrates. Analysis of PL for each substrate shows a strong intensity dependence on substrate (Fig. 7.6). With the same pyrene deposition conditions the PL intensity can vary by an order of magnitude depending on the substrate. These intensity variations do not align with the PLE absorption ratio variations and so presumably arise from another mechanism. It is possible that different substrates attract more or

less of the pyrene to the surface during vacuum deposition. In order to control for such variations, in the following sections the ratios of emission strengths are studied rather than absolute intensities.

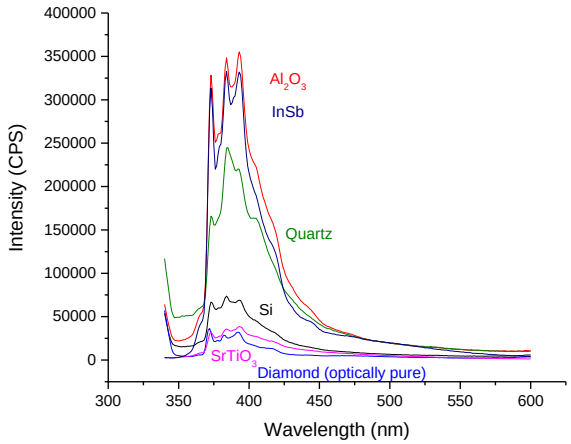

Figure 7.6: PL spectra for 325 nm excitation of pyrene deposited on the surface of a range of substrates.

7.2.4 Results (PLE)

Pyrene presents absorption peaks at 272 and 335 nm in the UV that are connected to the monomer emissions at 370-400 nm. In a diluted liquid phase, the ratio of those peaks is approximately 1:1 (Fig. 7.7).

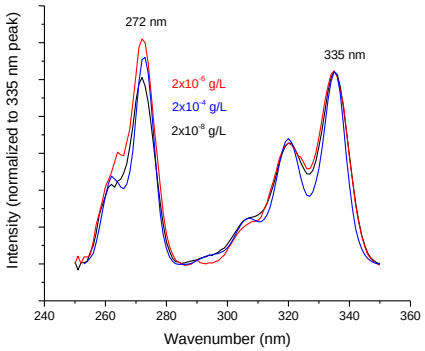

Figure 7.7: PLE spectrum at 373 nm for pyrene diluted in at alcohol concentrations of 10^{-8}, 10^{-6}, and 10^{-4} g/L, normalized at the 335 nm peak for clarity.

When the same measurement is performed on a range of substrates, the ratio between the 272 and 335 nm peak heights varies widely (Fig. 7.8). When comparing the 272/335 nm peak ratio across all of our selected substrates, we see that there are three distinct categories (Fig. 7.9). For most of the substrates tested, the peak ratio fell between 1.0 and 1.3, similar to isolated pyrene in alcohol. Two of our substrates, glass and a natural diamond anvil, had a ratio of less than 0.6, the only cases where the 272 nm peak was smaller than the 335 nm peak. These samples had a high density of optically active defects. The defect absorption at 272 nm was stronger than at 335 nm, which may have reduced the effective absorption of the 272 nm line of the pyrene. The mechanism for this is not understood. The other substrates in the series were optically pure.

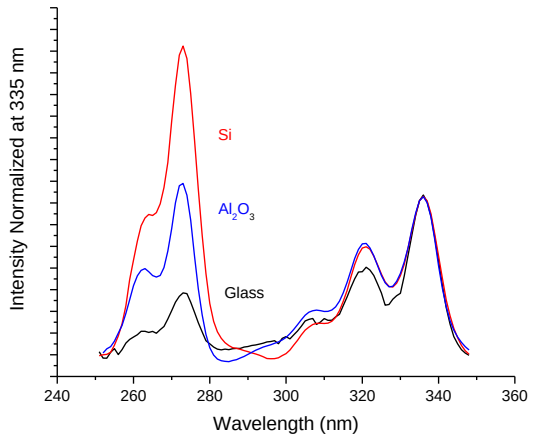

Figure 7.8: PLE spectrum of 373 nm emission for silicon, sapphire (Al_2O_3), and glass substrates, normalized to the peak intensity at 335 nm.

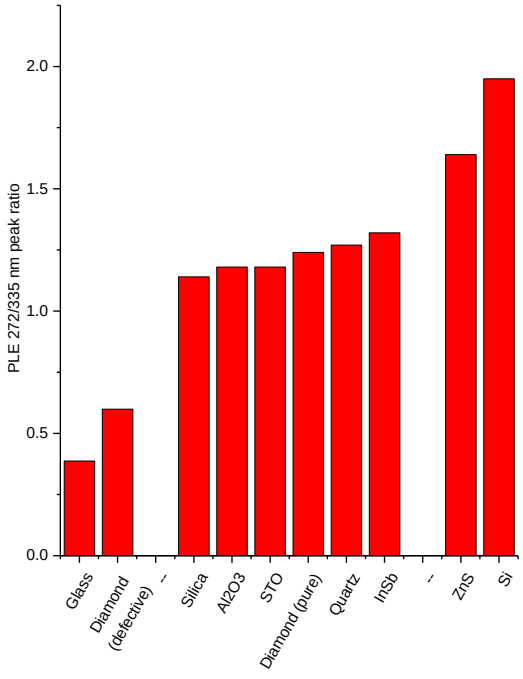

Figure 7.9: Ratio of 272/335 nm peaks for PLE 373 nm for all substrates.

ZnS and Si were the outliers in the other direction, with a ratio greater than 1.6. These ratios do not appear to depend on the amount of pyrene deposited. PVD was performed on ZnS

for 4 and 24 hr periods. Based on much stronger intensity of the PLE spectra (Fig. 7.10) and difference in deposition times, it is obvious much more pyrene is present in the 24 hr exposed sample. Despite the difference in quantity, the ratio for the 272/335 peaks remains the same.

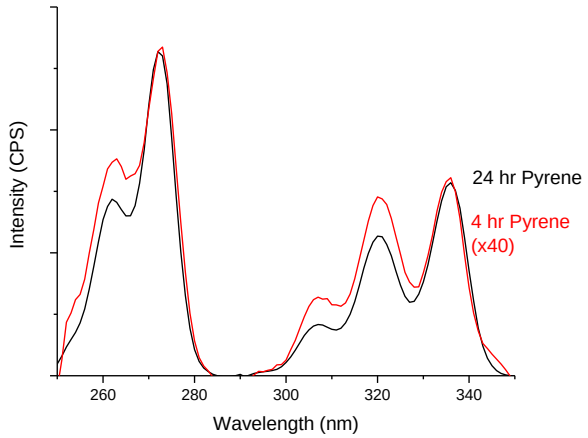

Figure 7.10: PLE spectra at 373 nm for ZnS surfaces with 24 hr and 4 hr pyrene deposition under the same conditions. The 4 hr pyrene spectrum has been scaled by a factor of 40 for comparison.

7.2.5 Calculated interfaces

In order to understand the substrate dependence of the absorption peaks of the deposited pyrene molecule, calculations were performed modeling the electronic structure of surface deposited pyrene. Diamond was chosen to represent the middle range of substrates with ratios approaching the 1:1 of isolated pyrene, and ZnS was chosen for its higher 272/335 nm ratio.

The theoretical calculations are based on ab-initio density functional theory (DFT).[130] We studied different model systems, isolated pyrene, pyrene deposited on a ZnS (110) surface, (pyrene-ZnS) and deposited on the (100) oxygenated diamond surface (pyrene-diamond). Steady state properties such as optimal structural configurations and full electronic structure were

obtained for all cases, while for the optical properties the calculations could be done only for the isolated pyrene molecule. Further details are given in the supplemental material.

The electronic and optical properties of the isolated pyrene molecule are summarized in Figs. 7.11 and 8. Figure 7.11 shows the electron density representation of the Kohn-Sham frontier orbitals mostly involved in the first (lower energy) excitations. Figure 7.12(b) displays the density of states (DOS) calculated at the generalized gradient approximation (GGA) level using both plain PBE[131] and hybrid exchange correlation functionals indicated as PBE0.[132] The electron distribution for the frontier levels (close to HOMO and LUMO) does not show significant differences when moving from bare to hybrid PBE, nor the ordering of levels in that region. Fig. 7.12(c) shows the optical absorption spectra obtained through time-dependent DFT (TDDFT)[133] in the same approximations as in Fig. 7.12(b). The first three peaks are the most relevant for comparison with experimental results. We see that the degree of exact-exchange included in the ground-state calculations is important for the actual value obtained for the excitation energy. Not surprisingly, PBE gives a poor agreement with the experimental values,[134] while the insertion of exact-exchange contribution at the PBE0 level (α=0.25) mostly corrects the problem.

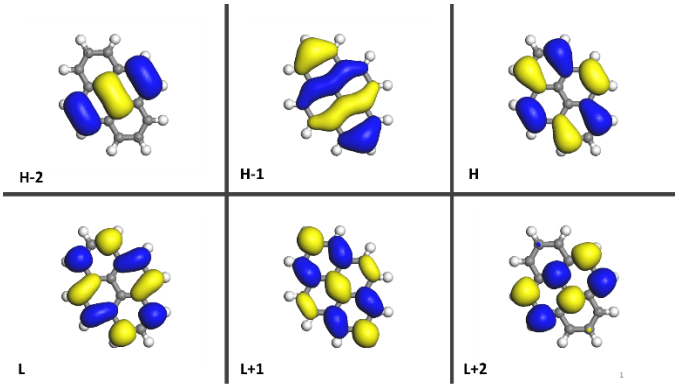

Figure 7.11: Electron density representation of the frontier orbitals in the lowest energy excitations for the isolated pyrene molecule.

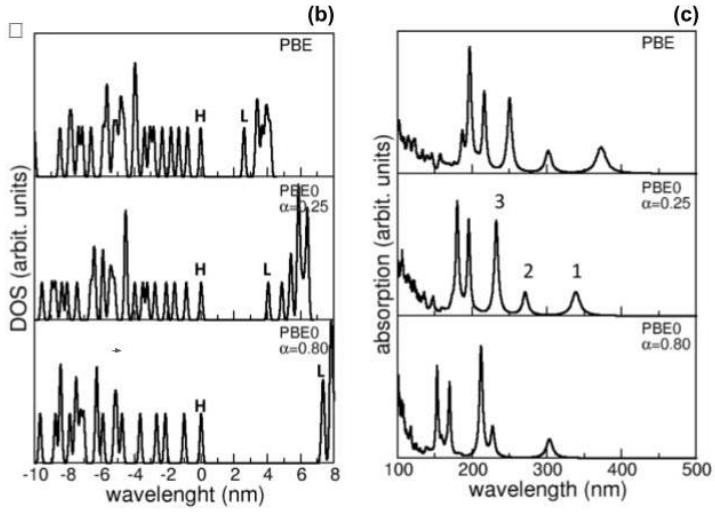

Figure 7.12: DFT calculation results for isolated pyrene. (a) the frontier orbitals electron distributions (HOMO {H}; HOMO-1 {H-1}; HOMO-2 {H-2}: LUMO {L}; LUMO+1 {L+1}; LUMO+2 {L+2}). DOS (b) and TDDFT absorption spectra (c) obtained within the GGA approximation for PBE and PBE0 (α = 0.25 and α = 0.80).

Table 2 details the analysis of the main absorption peaks for the isolated pyrene molecule. The lowest energy peak, referred to as peak 1, occurs at 340 nm, corresponding to the experimentally observed peak at 335 nm (Fig. 7.5). The orbital contribution to peak 1 is mostly a HOMO-LUMO transition. In the identified higher energy peaks, the lower occupied and higher unoccupied states (HOMO-1, LUMO+1) contribute strongly.

Excitation	Orbital contribution	Energy (eV/nm)	Oscillator strength
1	H→L (76%) H-1→L+1 (24%)	3.65/340	0.34
F1	H-1→L (50%) H→L+1 (50%)	3.72/333	0
F2	H-2→L (30%) H→L+1 (50%)	4.31/288	0
2	H-1→L (30%) H→L+1 (47%)	4.56/272	0.27
3	H-1→L+1 (60%) H→L (20%) H-2→L+1 (20%)	5.32/233	0.71

Table 7.2: Excitation analysis showing the orbital contributions for each peak in Fig. 12© obtained through TDDFT calculations for the isolated pyrene at PBE0 (α = 0.25) The forbidden singlet transition is included, labeled as F.

For pyrene on ZnS at the PBE0 α=0.25 level the DOS is calculated for the complete system (Fig. 7.13). The black curve is the total DOS, while the red curve is the DOS for the pyrene molecule at the surface. The DOS calculated in Fig. 7.12(b) is included for comparison. The lowest energy electronic state of pyrene is aligned in order to have a common energy reference. For ZnS, the LUMO of pyrene lies in the conduction band, the HOMO of the molecule is in the gap, and the HOMO-1 lies inside the valence band.

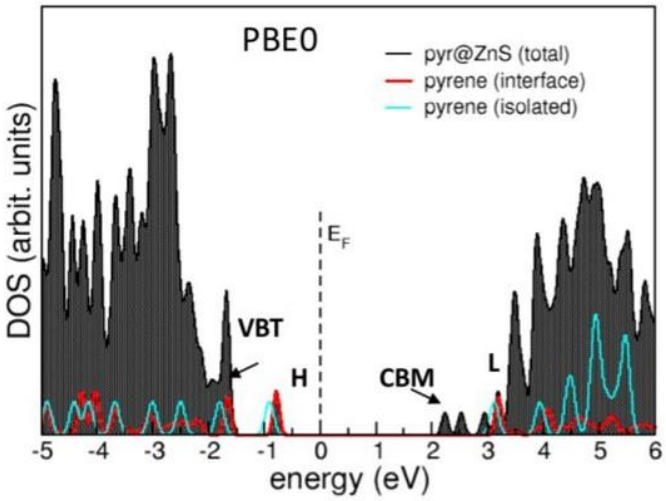

Figure 7.13: Results obtained for pyrene-ZnS: DOS for the total system, deposited interface, and isolated pyrene molecule. VBT = valence band top, CBM = conduction band minimum.

The electronic structure for pyrene on diamond was obtained through PBE calculations (Fig. 7.14). Because the molecular HOMO is too close to the CBM of the diamond, the hybrid calculation cannot be done for the complete model. As a result, Fig. 7.14(b) and 7.14(c) show the DOS calculated for the isolated molecule and isolated diamond surface using PBE and PBE0, respectively, estimating the effect of inclusion of the α=0.25 exchange.

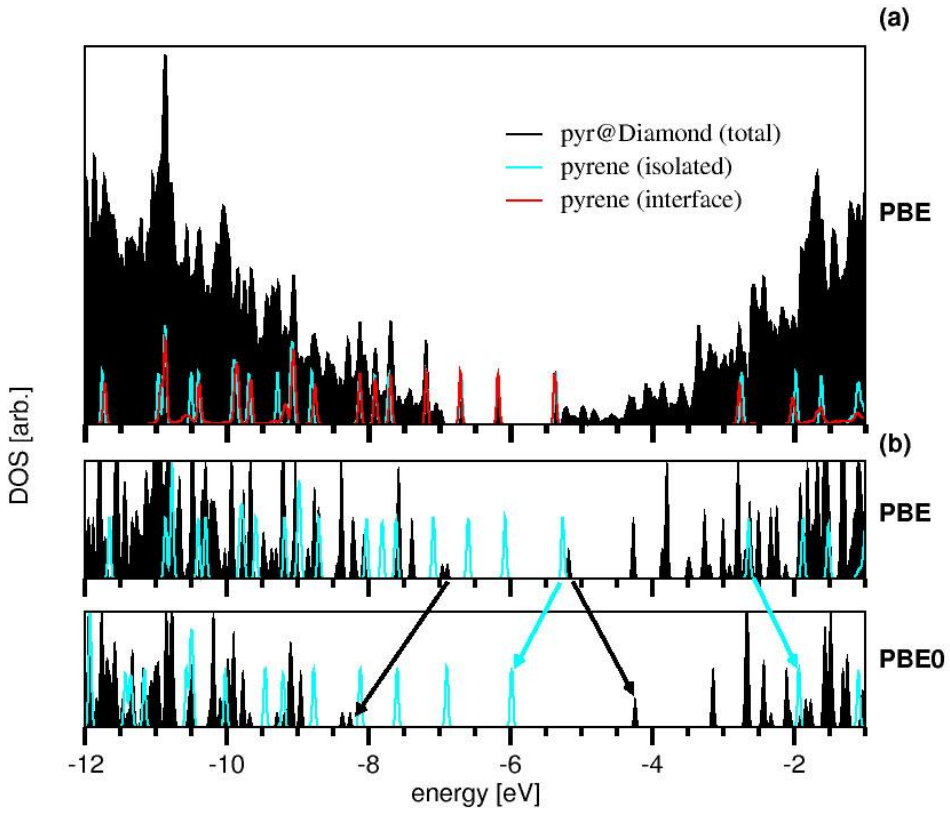

Figure 7.14: Results obtained for pyrene-diamond: (a) DOS for the complete system, isolated pyrene molecule, and selected pyrene states of the molecule on surface systems; (b) superimposed DOS's for the isolated systems at the PBE and PBE0 (α = 0.25) levels.

Similar to pyrene on the ZnS surface, the LUMO of pyrene lies inside the conduction band for the diamond gap and the HOMO of the molecule falls within the gap. The important difference is that for ZnS the HOMO-1 is inside the valence band but for the diamond interface the HOMO-1 falls inside the gap. Referring to our findings in table 7.2, a connection can be drawn between the intensity of the absorption peaks and the position of the pyrene's frontier orbital levels relative to the bands of the substrate material. When the pyrene is isolated (suspended in liquid), the ratio of peak 2 to peak 1 is ~1:1. When both contributing transitions (HOMO→LUMO and HOMO-1→LUMO) start within the gap, as with diamond, the ratio is still

close to 1. When the HOMO is in the gap but the HOMO-1 is not, as with ZnS, peak 2 is enhanced such that the ratio increases to over 1.6 (Fig. 7.15).

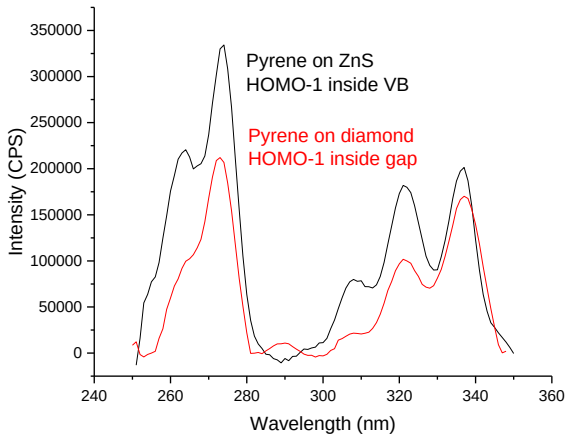

Figure 7.15: PLE 373 nm spectra for pyrene on ZnS and diamond surfaces.

7.2.6 Thermal oxide on Si

Because of the differences between PLE ratios for UV silica and silicon, thermal oxide (silicon with SiO_2 coating) was used to study the range of the effect of the substrate surface on the pyrene spectra. Using the same methodology as before, pyrene was deposited on the surface of thermal oxide wafers with SiO_2 layers 1 µm, 300 nm, and 70 nm thick. Resultant PLE spectra reveal that the effects causing the absorption differences have a depth dependence (Fig. 7.16).

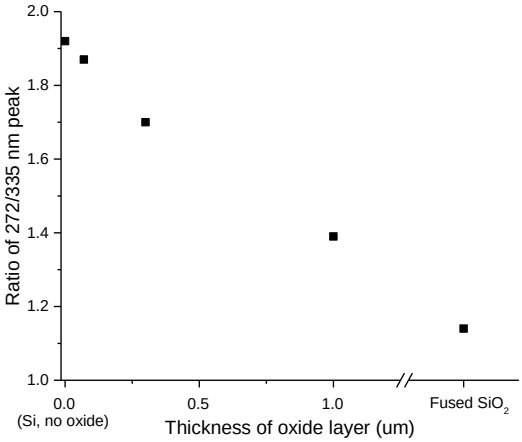

Figure 7.16: Ratio of the 272 nm absorption peaks and 335 nm absorption peaks from the PLE spectra of fused silica and thermal oxide layers of 3 different thicknesses.

For the fused silica sample the substrate is effectively an infinitely thick thermal oxide layer and the 272 nm absorption peak, which has a HOMO-1→LUMO contribution, is unenhanced. When the thermal oxide layer is thin, as with the 70 nm sample, the effects of the underlying Si still contribute in such a way that the 272 nm absorption is enhanced. As the thermal oxide layer thickens the effects of the underlying material are reduced.

7.2.7 Conclusions

In conclusion, the absorption spectrum of pyrene has a dependence upon the substrate it is deposited on. The first absorption peak at ~335 nm is shown to depend mostly upon the HOMO→LUMO transition, while the second feature at ~272 nm has a contribution from the HOMO-1→LUMO transition. When the HOMO-1 falls within the valence band of the substrate, peak 2 is enhanced in the PLE spectrum. Experiments with different thicknesses of thermal oxide layers suggest that the interaction between pyrene and the substrate has a μm-scale range. This special scale is on the order of the wavelength of the light, implying electromagnetic

coupling. Regardless of the exact mechanism, this interaction could be utilized as a material-specific contrast in microscope images.

This research was supported by the U.S. Department of Energy, Office of Basic Energy Sciences, Division of Materials Science and Engineering under Award No. DE-FG02-07ER46386.

APPENDIX A: Ir^{4+} MATRIX

A1: Introduction

This appendix details work performed during my graduate studies in an attempt to justify the polarizability of the Ir^{4+} transition peak discussed in detail in Chapter 4. Most of this was performed before the revelation that the sideband features were only present with the presence of Mg-Ir pairs. This work attempted to simplify the system and just compare the largest, closest in energy sideband, as if it was part of the normal Ir^{4+} transition, with the intent of seeing what kind of perturbations would be necessary to create the much smaller peak shifted slightly lower in energy. To that end, I selected a single Ga(II) atom and its nearest oxygen neighbors, used cartesian coordinate hydrogen wavefunctions from literature[135] to approximate wavefunctions for this 7 atom system, and applied these wavefunctions to a matrix in order to integrate for matrix elements and then solve for the eigenvalues and eigenvectors for the system.

Using the parameters that will be further described in this appendix, I was never able to use my model to generate eigenvalues and eigenvectors that would justify either my polarization dependence or even the presence of a single tiny shifted peak. Rather, my best parameter estimates with this model would suggest that if two split peaks existed they should be close in intensity, when the observable reality has the largest sideband at only a small percent of the primary peak. What's more, the model was obviously flawed once we took into account the realization that the magnesium is playing a role. As such, and as mentioned in the future work section of Chapter 5, we still do not know what causes the polarization dependent effects in the 5148 cm^{-1} peak.

Despite the flaws in the model and lack of conclusive results, the calculations involved are included here for reference. The positioning of the atoms and wavefunction integrations might be of use to any future graduate students in the McCluskey lab who hope to pursue this further.

A2: Atomic positions

The atomic positions for a Ga(II) atom were taken from the Materials Project, an online database that complies material information to aid researchers. The specific gallium oxide data page on the site is attributed to the Persson group at Lawrence Berkeley National Labs.[136] Using this data, I selected a gallium atom and its neighboring oxygen atoms (labeled O1-O6 below) located at the given coordinates relative to the corner of the unit cell:

	X (Å)	Y (Å)	Z (Å)
Gallium	9.5264	1.5415	3.9162
O1	9.1778	0	5.0873
O2	9.6851	0	2.4876
O3	9.6851	3.083	2.4876
O4	9.1778	3.083	5.0873
O5	7.6035	1.5415	3.2218
O6	11.4696	1.5415	4.245

Table A1: Atomic positions of the selected gallium and oxygen atoms in the unit cell before adjustment.

To make this easier to work with in our model, I translated the system so that the gallium atom was the center of the coordinate system at (0,0,0), and then rotated the system 13.7 degrees around the y axis to account for the 103.7 degree angle between the **a** and **c** axes of the cell. The end result is such that the **z** axis of the new system is the same as the **c** axis for the crystal cell, and the **y** axis is the same as the **b** axis for the monoclinic cell. The **x** axis is then comparable but not aligned exactly with the **a** axis of the monoclinic cell. Figure A1 shows an image of the isolated atoms and table A2 contains the shifted and rotated coordinates.

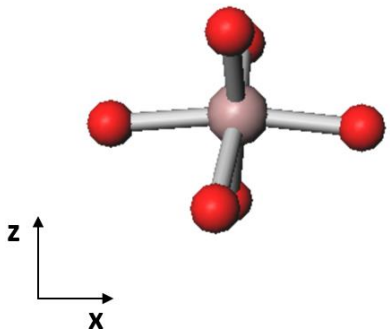

Figure A1: Model of the gallium atom and nearest six oxygen neighbors.

	X (Å)	Y (Å)	Z (Å)
Gallium	0	0	3.9162
O1	-0.061748	-1.5415	1.220321408
O2	-0.183663	-1.5415	-1.425605676
O3	-0.183663	1.5415	-1.425605676
O4	-0.061748	1.5415	1.220321408
O5	-2.032575	0	-0.219939271

O6	1.9658358	0	-0.140090289

Table A2: Atomic positions of the selected gallium and oxygen atoms in the unit cell after translation and rotation.

A3: The wavefunction matrix

The thought was to use a matrix to represent the energies acting on the Ir^{4+} transition from the ground state to an excited d orbital and incorporate the distances/positions involved for each neighbor. The process started with a matrix that looked like this:

	Y	**Z**	**X**	**YX**	**YZ**	**XZ**
Y	**E_p**	**Z`Y**	**X`Y**	**YX`Y**	**YZ`Y**	**XZ`Y**
Z	**Y`Z**	**E_p**	**X`Z**	**YX`Z**	**YZ`Z**	**XZ`Z**
X	**Y`X**	**Z`X**	**E_p**	**YX`X**	**YZ`X**	**XZ`X**
YX	**Y`YX**	**Z`YX**	**X`YX**	**E_1**	**YZ`YX**	**XZ`YX**
YZ	**Y`YZ**	**Z`YZ**	**X`YZ**	**YX`YZ**	**E_1**	**XZ`YZ**
XZ	**Y`XZ**	**Z`XZ**	**X`XZ**	**YX`XZ**	**YZ`XZ**	**0**

Table A3: Generic form of the matrix used with energies on the diagonal

where the diagonal terms are the unperturbed energies of the system. E_p are our excited states >> the energies of our peaks E_1 (5148 cm^{-1}) and our unexcited ground state is set to 0. Our perturbing wavefunctions are represented by **Y,Z,X,YX,YZ,** and **XZ** and will be explained in the next section. The off-diagonal terms are the perturbations and represent an integral of the wavefunctions acting on that particular term. For example, **Y`Z** is a shorthand denoting the integral

$$\sum_{1}^{6} \langle \boldsymbol{Y} | dV_n | \boldsymbol{Z} \rangle$$

which can be written as

$$\int \boldsymbol{YZ} * d(x - x_n, y - y_n, z - z_n)$$

The wavefunctions **Y** and **Z** will be further explored in the next section and include the calculated distances y_n and z_n for each oxygen atom from table A2, such that $y_1z_1+y_2z_2+\ldots$can be pulled in front of the remaining integral.

A4: The wavefunctions

Ogilvie used partial separation of variables to solve the time independent Schrödinger's equation for the hydrogen atom in cartesian coordinates.[135] They give the total amplitude function, incompletely normalized, as

$$\Psi_{x,y,z} = \sqrt{\frac{(k+2l+2)!\,(k+2l+2)}{k!\,a_\mu}}\, Q_{l,m}(x,y,z)\boldsymbol{e}^{\left(-\sqrt{\boldsymbol{x^2+y^2+\frac{z^2}{a_\mu(k+l+1)}}}\right)} *$$

$$LaguerreL(k, 2l+1, \frac{\sqrt{x^2+y^2+z^2}}{a_\mu(k+l+1)}) / ((-1)^l (2+2l)!\,(k+l+1)!$$

Where $Q_{l,m}$ are a series of functions given in table 1 of Oglilvie for all necessary values of *l* and *m*. I used Linear combinations of Q values for plus and minus *m* to isolate the xyz components of the Q. For our masses a_μ can be approximated as the bohr radius. Also from Ogilvie, when

n=3, l=2 and k=0, and when n=2, l=1 and k = 0. The **X,Y,Z** terms act on the excited P orbitals, so k=0 and l=1 and the **YX, YZ, XZ** terms are on the d orbitals so k=0 and l=2.

Inserting the appropriate l and m values and solving the LaguerreL polynomial, the following are the wavefunctions used on the matrix:

$$\boldsymbol{Z} = \frac{1}{\sqrt{6a_0}} ze^{-\frac{\sqrt{x^2+y^2+z^2}}{2a_0}}$$

$$\boldsymbol{Y} = \frac{i}{\sqrt{12a_0}} ye^{-\frac{\sqrt{x^2+y^2+z^2}}{2a_0}}$$

$$\boldsymbol{X} = \frac{-1}{\sqrt{12a_0}} xe^{-\frac{\sqrt{x^2+y^2+z^2}}{2a_0}}$$

$$\boldsymbol{XZ} = \frac{1}{3\sqrt{15a_0}} xze^{-\frac{\sqrt{x^2+y^2+z^2}}{3a_0}}$$

$$\boldsymbol{YX} = \frac{i}{6\sqrt{15a_0}} yxe^{-\frac{\sqrt{x^2+y^2+z^2}}{3a_0}}$$

$$\boldsymbol{YZ} = \frac{-i}{3\sqrt{15a_0}} yze^{-\frac{\sqrt{x^2+y^2+z^2}}{3a_0}}$$

From there each off diagonal piece can be individually integrated for. The following section shows the results of each solved integral as it was entered into Mathematica for calculation. Each value of $x_n y_n, z_n$ correspond to the atomic coordinates for each oxygen atom 1-6 given in table A2.

$$\mathbf{Y`Z} = \left(-i/\left(6\sqrt{(2)} * \mathrm{a0}\right)\right)$$

$$* \left(\left(\mathrm{y1} * \mathrm{z1} * e^{-\sqrt{(\mathrm{x1}^2+\mathrm{y1}^2+\mathrm{z1}^2)}/\mathrm{a0}}\right) + \left(\mathrm{y2} * \mathrm{z2} * e^{-\sqrt{(\mathrm{x2}^2+\mathrm{y2}^2+\mathrm{z2}^2)}/\mathrm{a0}}\right)\right.$$

$$+ \left(\mathrm{y3} * \mathrm{z3} * e^{-\sqrt{(\mathrm{x3}^2+\mathrm{y3}^2+\mathrm{z3}^2)}/\mathrm{a0}}\right) + \left(\mathrm{y4} * \mathrm{z4} * e^{-\sqrt{(\mathrm{x4}^2+\mathrm{y4}^2+\mathrm{z4}^2)}/\mathrm{a0}}\right)$$

$$\left. + \left(\mathrm{y5} * \mathrm{z5} * e^{-\sqrt{(\mathrm{x5}^2+\mathrm{y5}^2+\mathrm{z5}^2)}/\mathrm{a0}}\right) + \left(\mathrm{y6} * \mathrm{z6} * e^{-\sqrt{(\mathrm{x6}^2+\mathrm{y6}^2+\mathrm{z6}^2)}/\mathrm{a0}}\right)\right)$$

=0+0i

$$\mathbf{Z`Y} = \left(i/\left(6\sqrt{(2)} * \mathrm{a0}\right)\right)$$

$$* \left(\left(\mathrm{y1} * \mathrm{z1} * e^{-\sqrt{(\mathrm{x1}^2+\mathrm{y1}^2+\mathrm{z1}^2)}/\mathrm{a0}}\right) + \left(\mathrm{y2} * \mathrm{z2} * e^{-\sqrt{(\mathrm{x2}^2+\mathrm{y2}^2+\mathrm{z2}^2)}/\mathrm{a0}}\right)\right.$$

$$+ \left(\mathrm{y3} * \mathrm{z3} * e^{-\sqrt{(\mathrm{x3}^2+\mathrm{y3}^2+\mathrm{z3}^2)}/\mathrm{a0}}\right) + \left(\mathrm{y4} * \mathrm{z4} * e^{-\sqrt{(\mathrm{x4}^2+\mathrm{y4}^2+\mathrm{z4}^2)}/\mathrm{a0}}\right)$$

$$\left. + \left(\mathrm{y5} * \mathrm{z5} * e^{-\sqrt{(\mathrm{x5}^2+\mathrm{y5}^2+\mathrm{z5}^2)}/\mathrm{a0}}\right) + \left(\mathrm{y6} * \mathrm{z6} * e^{-\sqrt{(\mathrm{x6}^2+\mathrm{y6}^2+\mathrm{z6}^2)}/\mathrm{a0}}\right)\right)$$

=0+0i

$$\mathbf{X`Z} = \mathbf{Z`X} = \left(-1/\left(6\sqrt{(2)} * \mathrm{a0}\right)\right)$$

$$* \left(\left(\mathrm{x1} * \mathrm{z1} * e^{-\sqrt{(\mathrm{x1}^2+\mathrm{y1}^2+\mathrm{z1}^2)}/\mathrm{a0}}\right) + \left(\mathrm{x2} * \mathrm{z2} * e^{-\sqrt{(\mathrm{x2}^2+\mathrm{y2}^2+\mathrm{z2}^2)}/\mathrm{a0}}\right)\right.$$

$$+ \left(\mathrm{x3} * \mathrm{z3} * e^{-\sqrt{(\mathrm{x3}^2+\mathrm{y3}^2+\mathrm{z3}^2)}/\mathrm{a0}}\right) + \left(\mathrm{x4} * \mathrm{z4} * e^{-\sqrt{(\mathrm{x4}^2+\mathrm{y4}^2+\mathrm{z4}^2)}/\mathrm{a0}}\right)$$

$$\left. + \left(\mathrm{x5} * \mathrm{z5} * e^{-\sqrt{(\mathrm{x5}^2+\mathrm{y5}^2+\mathrm{z5}^2)}/\mathrm{a0}}\right) + \left(\mathrm{x6} * \mathrm{z6} * e^{-\sqrt{(\mathrm{x6}^2+\mathrm{y6}^2+\mathrm{z6}^2)}/\mathrm{a0}}\right)\right)$$

= -0.00196778

$$\boldsymbol{X`Y} = \boldsymbol{Y`X} = (-i/(12 * \mathrm{a0}))$$

$$* \left(\left(\mathrm{x1} * \mathrm{y1} * e^{-\sqrt{(\mathrm{x1}^2+\mathrm{y1}^2+\mathrm{z1}^2)}/\mathrm{a0}} \right) + \left(\mathrm{x2} * \mathrm{y2} * e^{-\sqrt{(\mathrm{x2}^2+\mathrm{y2}^2+\mathrm{z2}^2)}/\mathrm{a0}} \right) \right.$$

$$+ \left(\mathrm{x3} * \mathrm{y3} * e^{-\sqrt{(\mathrm{x3}^2+\mathrm{y3}^2+\mathrm{z3}^2)}/\mathrm{a0}} \right) + \left(\mathrm{x4} * \mathrm{y4} * e^{-\sqrt{(\mathrm{x4}^2+\mathrm{y4}^2+\mathrm{z4}^2)}/\mathrm{a0}} \right)$$

$$\left. + \left(\mathrm{x5} * \mathrm{y5} * e^{-\sqrt{(\mathrm{x5}^2+\mathrm{y5}^2+\mathrm{z5}^2)}/\mathrm{a0}} \right) + \left(\mathrm{x6} * \mathrm{y6} * e^{-\sqrt{(\mathrm{x6}^2+\mathrm{y6}^2+\mathrm{z6}^2)}/\mathrm{a0}} \right) \right)$$

=0+0i

$$\mathbf{Z`XZ} = \mathbf{XZ`Z} = \left(1/\left(9\sqrt{(10)} * \mathrm{a0} \right) \right)$$

$$* \left(\left(\mathrm{z1} * \mathrm{x1} * \mathrm{z1} * e^{-(5/6)*\sqrt{(\mathrm{x1}^2+\mathrm{y1}^2+\mathrm{z1}^2)}/\mathrm{a0}} \right) \right.$$

$$+ \left(\mathrm{z2} * \mathrm{x2} * \mathrm{z2} * e^{-(5/6)*\sqrt{(\mathrm{x2}^2+\mathrm{y2}^2+\mathrm{z2}^2)}/\mathrm{a0}} \right)$$

$$+ \left(\mathrm{z3} * \mathrm{x3} * \mathrm{z3} * e^{-(5/6)*\sqrt{(\mathrm{x3}^2+\mathrm{y3}^2+\mathrm{z3}^2)}/\mathrm{a0}} \right)$$

$$+ \left(\mathrm{z4} * \mathrm{x4} * \mathrm{z4} * e^{-(5/6)*\sqrt{(\mathrm{x4}^2+\mathrm{y4}^2+\mathrm{z4}^2)}/\mathrm{a0}} \right)$$

$$+ \left(\mathrm{z5} * \mathrm{x5} * \mathrm{z5} * e^{-(5/6)*\sqrt{(\mathrm{x5}^2+\mathrm{y5}^2+\mathrm{z5}^2)}/\mathrm{a0}} \right)$$

$$\left. + \left(\mathrm{z6} * \mathrm{x6} * \mathrm{z6} * e^{-(5/6)*\sqrt{(\mathrm{x6}^2+\mathrm{y6}^2+\mathrm{z6}^2)}/\mathrm{a0}} \right) \right)$$

= -0.00249127

$$\mathbf{YZ`Z} = \mathbf{Z`YZ} = \left(-i/\left(9\sqrt{(10)} * \mathrm{a0}\right)\right)$$

$$* \left(\left(\mathrm{z1} * \mathrm{y1} * \mathrm{z1} * e^{-(5/6)*\sqrt{(\mathrm{x1}^2+\mathrm{y1}^2+\mathrm{z1}^2)}/\mathrm{a0}}\right)\right.$$

$$+ \left(\mathrm{z2} * \mathrm{y2} * \mathrm{z2} * e^{-(5/6)*\sqrt{(\mathrm{x2}^2+\mathrm{y2}^2+\mathrm{z2}^2)}/\mathrm{a0}}\right)$$

$$+ \left(\mathrm{z3} * \mathrm{y3} * \mathrm{z3} * e^{-(5/6)*\sqrt{(\mathrm{x3}^2+\mathrm{y3}^2+\mathrm{z3}^2)}/\mathrm{a0}}\right)$$

$$+ \left(\mathrm{z4} * \mathrm{y4} * \mathrm{z4} * e^{-(5/6)*\sqrt{(\mathrm{x4}^2+\mathrm{y4}^2+\mathrm{z4}^2)}/\mathrm{a0}}\right)$$

$$+ \left(\mathrm{z5} * \mathrm{y5} * \mathrm{z5} * e^{-(5/6)*\sqrt{(\mathrm{x5}^2+\mathrm{y5}^2+\mathrm{z5}^2)}/\mathrm{a0}}\right)$$

$$\left.+ \left(\mathrm{z6} * \mathrm{y6} * \mathrm{z6} * e^{-(5/6)*\sqrt{(\mathrm{x6}^2+\mathrm{y6}^2+\mathrm{z6}^2)}/\mathrm{a0}}\right)\right)$$

=0+0i

$$\mathbf{Z`YX} = \mathbf{YX`Z} = \left(i/\left(18\sqrt{(10)} * \mathrm{a0}\right)\right)$$

$$* \left(\left(\mathrm{z1} * \mathrm{y1} * \mathrm{x1} * e^{-(5/6)*\sqrt{(\mathrm{x1}^2+\mathrm{y1}^2+\mathrm{z1}^2)}/\mathrm{a0}}\right)\right.$$

$$+ \left(\mathrm{z2} * \mathrm{y2} * \mathrm{x2} * e^{-(5/6)*\sqrt{(\mathrm{x2}^2+\mathrm{y2}^2+\mathrm{z2}^2)}/\mathrm{a0}}\right)$$

$$+ \left(\mathrm{z3} * \mathrm{y3} * \mathrm{x3} * e^{-(5/6)*\sqrt{(\mathrm{x3}^2+\mathrm{y3}^2+\mathrm{z3}^2)}/\mathrm{a0}}\right)$$

$$+ \left(\mathrm{z4} * \mathrm{y4} * \mathrm{x4} * e^{-(5/6)*\sqrt{(\mathrm{x4}^2+\mathrm{y4}^2+\mathrm{z4}^2)}/\mathrm{a0}}\right)$$

$$+ \left(\mathrm{z5} * \mathrm{y5} * \mathrm{x5} * e^{-(5/6)*\sqrt{(\mathrm{x5}^2+\mathrm{y5}^2+\mathrm{z5}^2)}/\mathrm{a0}}\right)$$

$$\left.+ \left(\mathrm{z6} * \mathrm{y6} * \mathrm{x6} * e^{-(5/6)*\sqrt{(\mathrm{x6}^2+\mathrm{y6}^2+\mathrm{z6}^2)}/\mathrm{a0}}\right)\right)$$

=0+0i

$$\mathbf{Y`XZ} = \mathbf{XZ`Y} = \left(-i/\left(18\sqrt{(5)} * \mathrm{a0}\right)\right)$$

$$* \left(\left(\mathrm{z1} * \mathrm{y1} * \mathrm{x1} * e^{-(5/6)*\sqrt{(\mathrm{x1}^2+\mathrm{y1}^2+\mathrm{z1}^2)}/\mathrm{a0}}\right)\right.$$

$$+ \left(\mathrm{z2} * \mathrm{y2} * \mathrm{x2} * e^{-(5/6)*\sqrt{(\mathrm{x2}^2+\mathrm{y2}^2+\mathrm{z2}^2)}/\mathrm{a0}}\right)$$

$$+ \left(\mathrm{z3} * \mathrm{y3} * \mathrm{x3} * e^{-(5/6)*\sqrt{(\mathrm{x3}^2+\mathrm{y3}^2+\mathrm{z3}^2)}/\mathrm{a0}}\right)$$

$$+ \left(\mathrm{z4} * \mathrm{y4} * \mathrm{x4} * e^{-(5/6)*\sqrt{(\mathrm{x4}^2+\mathrm{y4}^2+\mathrm{z4}^2)}/\mathrm{a0}}\right)$$

$$+ \left(\mathrm{z5} * \mathrm{y5} * \mathrm{x5} * e^{-(5/6)*\sqrt{(\mathrm{x5}^2+\mathrm{y5}^2+\mathrm{z5}^2)}/\mathrm{a0}}\right)$$

$$\left.+ \left(\mathrm{z6} * \mathrm{y6} * \mathrm{x6} * e^{-(5/6)*\sqrt{(\mathrm{x6}^2+\mathrm{y6}^2+\mathrm{z6}^2)}/\mathrm{a0}}\right)\right)$$

=0+0i

$$\mathbf{Y`YZ} = \mathbf{YZ`Y} = \left(-1/\left(18\sqrt{(5)} * \mathrm{a0}\right)\right)$$

$$* \left(\left(\mathrm{z1} * \mathrm{y1} * \mathrm{y1} * e^{-(5/6)*\sqrt{(\mathrm{x1}^2+\mathrm{y1}^2+\mathrm{z1}^2)}/\mathrm{a0}}\right)\right.$$

$$+ \left(\mathrm{z2} * \mathrm{y2} * \mathrm{y2} * e^{-(5/6)*\sqrt{(\mathrm{x2}^2+\mathrm{y2}^2+\mathrm{z2}^2)}/\mathrm{a0}}\right)$$

$$+ \left(\mathrm{z3} * \mathrm{y3} * \mathrm{y3} * e^{-(5/6)*\sqrt{(\mathrm{x3}^2+\mathrm{y3}^2+\mathrm{z3}^2)}/\mathrm{a0}}\right)$$

$$+ \left(\mathrm{z4} * \mathrm{y4} * \mathrm{y4} * e^{-(5/6)*\sqrt{(\mathrm{x4}^2+\mathrm{y4}^2+\mathrm{z4}^2)}/\mathrm{a0}}\right)$$

$$+ \left(\mathrm{z5} * \mathrm{y5} * \mathrm{y5} * e^{-(5/6)*\sqrt{(\mathrm{x5}^2+\mathrm{y5}^2+\mathrm{z5}^2)}/\mathrm{a0}}\right)$$

$$\left.+ \left(\mathrm{z6} * \mathrm{y6} * \mathrm{y6} * e^{-(5/6)*\sqrt{(\mathrm{x6}^2+\mathrm{y6}^2+\mathrm{z6}^2)}/\mathrm{a0}}\right)\right)$$

= -0.00078528

$$\mathbf{Y`YX} = \mathbf{YX`Y} = \left(1/\left(36\sqrt{(5)} * \mathrm{a0}\right)\right)$$

$$* \left(\left(\mathrm{x1} * \mathrm{y1} * \mathrm{y1} * e^{-(5/6)*\sqrt{(\mathrm{x1}^2+\mathrm{y1}^2+\mathrm{z1}^2)}/\mathrm{a0}}\right)\right.$$

$$+ \left(\mathrm{x2} * \mathrm{y2} * \mathrm{y2} * e^{-(5/6)*\sqrt{(\mathrm{x2}^2+\mathrm{y2}^2+\mathrm{z2}^2)}/\mathrm{a0}}\right)$$

$$+ \left(\mathrm{x3} * \mathrm{y3} * \mathrm{y3} * e^{-(5/6)*\sqrt{(\mathrm{x3}^2+\mathrm{y3}^2+\mathrm{z3}^2)}/\mathrm{a0}}\right)$$

$$+ \left(\mathrm{x4} * \mathrm{y4} * \mathrm{y4} * e^{-(5/6)*\sqrt{(\mathrm{x4}^2+\mathrm{y4}^2+\mathrm{z4}^2)}/\mathrm{a0}}\right)$$

$$+ \left(\mathrm{x5} * \mathrm{y5} * \mathrm{y5} * e^{-(5/6)*\sqrt{(\mathrm{x5}^2+\mathrm{y5}^2+\mathrm{z5}^2)}/\mathrm{a0}}\right)$$

$$\left.+ \left(\mathrm{x6} * \mathrm{y6} * \mathrm{y6} * e^{-(5/6)*\sqrt{(\mathrm{x6}^2+\mathrm{y6}^2+\mathrm{z6}^2)}/\mathrm{a0}}\right)\right)$$

= -0.00105262

$$\mathbf{X`XZ} = \mathbf{XZ`X} = \left(-1/\left(18\sqrt{(5)} * \mathrm{a0}\right)\right)$$

$$* \left(\left(\mathrm{z1} * \mathrm{x1} * \mathrm{x1} * e^{-(5/6)*\sqrt{(\mathrm{x1}^2+\mathrm{y1}^2+\mathrm{z1}^2)}/\mathrm{a0}}\right)\right.$$

$$+ \left(\mathrm{z2} * \mathrm{x2} * \mathrm{x2} * e^{-(5/6)*\sqrt{(\mathrm{x2}^2+\mathrm{y2}^2+\mathrm{z2}^2)}/\mathrm{a0}}\right)$$

$$+ \left(\mathrm{z3} * \mathrm{x3} * \mathrm{x3} * e^{-(5/6)*\sqrt{(\mathrm{x3}^2+\mathrm{y3}^2+\mathrm{z3}^2)}/\mathrm{a0}}\right)$$

$$+ \left(\mathrm{z4} * \mathrm{x4} * \mathrm{x4} * e^{-(5/6)*\sqrt{(\mathrm{x4}^2+\mathrm{y4}^2+\mathrm{z4}^2)}/\mathrm{a0}}\right)$$

$$+ \left(\mathrm{z5} * \mathrm{x5} * \mathrm{x5} * e^{-(5/6)*\sqrt{(\mathrm{x5}^2+\mathrm{y5}^2+\mathrm{z5}^2)}/\mathrm{a0}}\right)$$

$$\left.+ \left(\mathrm{z6} * \mathrm{x6} * \mathrm{x6} * e^{-(5/6)*\sqrt{(\mathrm{x6}^2+\mathrm{y6}^2+\mathrm{z6}^2)}/\mathrm{a0}}\right)\right)$$

= 0.00299026

$$\mathbf{X`YZ} = \mathbf{YZ`X} = \left(i/\left(18\sqrt{(5)} * \mathrm{a0}\right)\right)$$

$$* \left(\left(\mathrm{z1} * \mathrm{y1} * \mathrm{x1} * e^{-(5/6)*\sqrt{(\mathrm{x1}^2+\mathrm{y1}^2+\mathrm{z1}^2)}/\mathrm{a0}}\right)\right.$$

$$+ \left(\mathrm{z2} * \mathrm{y2} * \mathrm{x2} * e^{-(5/6)*\sqrt{(\mathrm{x2}^2+\mathrm{y2}^2+\mathrm{z2}^2)}/\mathrm{a0}}\right)$$

$$+ \left(\mathrm{z3} * \mathrm{y3} * \mathrm{x3} * e^{-(5/6)*\sqrt{(\mathrm{x3}^2+\mathrm{y3}^2+\mathrm{z3}^2)}/\mathrm{a0}}\right)$$

$$+ \left(\mathrm{z4} * \mathrm{y4} * \mathrm{x4} * e^{-(5/6)*\sqrt{(\mathrm{x4}^2+\mathrm{y4}^2+\mathrm{z4}^2)}/\mathrm{a0}}\right)$$

$$+ \left(\mathrm{z5} * \mathrm{y5} * \mathrm{x5} * e^{-(5/6)*\sqrt{(\mathrm{x5}^2+\mathrm{y5}^2+\mathrm{z5}^2)}/\mathrm{a0}}\right)$$

$$\left. + \left(\mathrm{z6} * \mathrm{y6} * \mathrm{x6} * e^{-(5/6)*\sqrt{(\mathrm{x6}^2+\mathrm{y6}^2+\mathrm{z6}^2)}/\mathrm{a0}}\right)\right)$$

=0+0i

$$\mathbf{X`YX} = \mathbf{YX`X} = \left(-i/\left(36\sqrt{(5)} * \mathrm{a0}\right)\right)$$

$$* \left(\left(\mathrm{x1} * \mathrm{y1} * \mathrm{x1} * e^{-(5/6)*\sqrt{(\mathrm{x1}^2+\mathrm{y1}^2+\mathrm{z1}^2)}/\mathrm{a0}}\right)\right.$$

$$+ \left(\mathrm{x2} * \mathrm{y2} * \mathrm{x2} * e^{-(5/6)*\sqrt{(\mathrm{x2}^2+\mathrm{y2}^2+\mathrm{z2}^2)}/\mathrm{a0}}\right)$$

$$+ \left(\mathrm{x3} * \mathrm{y3} * \mathrm{x3} * e^{-(5/6)*\sqrt{(\mathrm{x3}^2+\mathrm{y3}^2+\mathrm{z3}^2)}/\mathrm{a0}}\right)$$

$$+ \left(\mathrm{x4} * \mathrm{y4} * \mathrm{x4} * e^{-(5/6)*\sqrt{(\mathrm{x4}^2+\mathrm{y4}^2+\mathrm{z4}^2)}/\mathrm{a0}}\right)$$

$$+ \left(\mathrm{x5} * \mathrm{y5} * \mathrm{x5} * e^{-(5/6)*\sqrt{(\mathrm{x5}^2+\mathrm{y5}^2+\mathrm{z5}^2)}/\mathrm{a0}}\right)$$

$$\left. + \left(\mathrm{x6} * \mathrm{y6} * \mathrm{x6} * e^{-(5/6)*\sqrt{(\mathrm{x6}^2+\mathrm{y6}^2+\mathrm{z6}^2)}/\mathrm{a0}}\right)\right)$$

=0+0i

XZ`YZ = YZ`XZ

$$= (-i/(135 * \mathrm{a0}))$$

$$* \left(\left(\mathrm{x1} * \mathrm{y1} * \mathrm{z1} * \mathrm{z1} * e^{-(2/3)*\sqrt{(\mathrm{x1}^2+\mathrm{y1}^2+\mathrm{z1}^2)}/\mathrm{a0}} \right) \right.$$

$$+ \left(\mathrm{x2} * \mathrm{y2} * \mathrm{z2} * \mathrm{z2} * e^{-(2/3)*\sqrt{(\mathrm{x2}^2+\mathrm{y2}^2+\mathrm{z2}^2)}/\mathrm{a0}} \right)$$

$$+ \left(\mathrm{x3} * \mathrm{y3} * \mathrm{z3} * \mathrm{z3} * e^{-(2/3)*\sqrt{(\mathrm{x3}^2+\mathrm{y3}^2+\mathrm{z3}^2)}/\mathrm{a0}} \right)$$

$$+ \left(\mathrm{x4} * \mathrm{y4} * \mathrm{z4} * \mathrm{z4} * e^{-(2/3)*\sqrt{(\mathrm{x4}^2+\mathrm{y4}^2+\mathrm{z4}^2)}/\mathrm{a0}} \right)$$

$$+ \left(\mathrm{x5} * \mathrm{y5} * \mathrm{z5} * \mathrm{z5} * e^{-(2/3)*\sqrt{(\mathrm{x5}^2+\mathrm{y5}^2+\mathrm{z5}^2)}/\mathrm{a0}} \right)$$

$$\left. + \left(\mathrm{x6} * \mathrm{y6} * \mathrm{z6} * \mathrm{z6} * e^{-(2/3)*\sqrt{(\mathrm{x6}^2+\mathrm{y6}^2+\mathrm{z6}^2)}/\mathrm{a0}} \right) \right)$$

=0+0i

XZ`YX = YX`XZ

$$= (i/(270 * a0))$$

$$* \left(\left(x1 * y1 * z1 * x1 * e^{-(2/3)*\sqrt{(x1^2+y1^2+z1^2)}/a0} \right) \right.$$

$$+ \left(x2 * y2 * z2 * x2 * e^{-(2/3)*\sqrt{(x2^2+y2^2+z2^2)}/a0} \right)$$

$$+ \left(x3 * y3 * z3 * x3 * e^{-(2/3)*\sqrt{(x3^2+y3^2+z3^2)}/a0} \right)$$

$$+ \left(x4 * y4 * z4 * x4 * e^{-(2/3)*\sqrt{(x4^2+y4^2+z4^2)}/a0} \right)$$

$$+ \left(x5 * y5 * z5 * x5 * e^{-(2/3)*\sqrt{(x5^2+y5^2+z5^2)}/a0} \right)$$

$$\left. + \left(x6 * y6 * z6 * x6 * e^{-(2/3)*\sqrt{(x6^2+y6^2+z6^2)}/a0} \right) \right)$$

=0+0i

$$\mathbf{YZ`YX = YX`YZ}$$

$$= (-1/(270 * \mathrm{a0}))$$

$$* \left(\left(\mathrm{x1} * \mathrm{y1} * \mathrm{z1} * \mathrm{y1} * e^{-(2/3)*\sqrt{(\mathrm{x1}^2+\mathrm{y1}^2+\mathrm{z1}^2)}/\mathrm{a0}} \right) \right.$$

$$+ \left(\mathrm{x2} * \mathrm{y2} * \mathrm{z2} * \mathrm{y2} * e^{-(2/3)*\sqrt{(\mathrm{x2}^2+\mathrm{y2}^2+\mathrm{z2}^2)}/\mathrm{a0}} \right)$$

$$+ \left(\mathrm{x3} * \mathrm{y3} * \mathrm{z3} * \mathrm{y3} * e^{-(2/3)*\sqrt{(\mathrm{x3}^2+\mathrm{y3}^2+\mathrm{z3}^2)}/\mathrm{a0}} \right)$$

$$+ \left(\mathrm{x4} * \mathrm{y4} * \mathrm{z4} * \mathrm{y4} * e^{-(2/3)*\sqrt{(\mathrm{x4}^2+\mathrm{y4}^2+\mathrm{z4}^2)}/\mathrm{a0}} \right)$$

$$+ \left(\mathrm{x5} * \mathrm{y5} * \mathrm{z5} * \mathrm{y5} * e^{-(2/3)*\sqrt{(\mathrm{x5}^2+\mathrm{y5}^2+\mathrm{z5}^2)}/\mathrm{a0}} \right)$$

$$+ \left. \left(\mathrm{x6} * \mathrm{y6} * \mathrm{z6} * \mathrm{y6} * e^{-(2/3)*\sqrt{(\mathrm{x6}^2+\mathrm{y6}^2+\mathrm{z6}^2)}/\mathrm{a0}} \right) \right)$$

= -0.0004018

These are the off-diagonal terms, fortunately many of them go to zero. From these terms, our matrix can be constructed:

GaONorm//MatrixForm

E_p	0	0	-0.00105*b*	-0.000785*b*	0
0	E_p	-0.00197*a*	0	0	-0.00249*b*
0	-0.001968*a*	E_p	0	0	0.00299*b*
-0.00105*b*	0	0	5148	0.000402*c*	0
-0.000785*b*	0	0	0.000402*c*	5148	0
0	-0.00249*b*	0.00299*b*	0	0	0

Table A4: Matrix with off-diagonal elements calculated before any more assumptions about parameters are made

Each section is given a different parameter to account for the only partial normalization of the wavefunctions and resulting mismatched units. *a* is used when the term contains 2 coordinate variables, *b* for 3, and *c* for 4. Had the model panned out more successfully, I would have had to make more efforts to physically justify parameter choices, but for early tests we simply were attempting to get eigenvalues/vectors that made sense.

One of the simplest approaches is to let $a=c=0$, by saying that only the *b* terms are directly acting upon our 5148 cm^{-1} states. Setting E_p to 20000 (arbitrary, just >> than 5148 and $b=$ 180000 (simply playing with the parameter until the eigenvalues approached the expected energies). The output eigenvalues/eigenvectors for these parameters are shown below:

Eigenvalues[GaONorm]

{20059.20537, 20009.09859 ,20000. ,5148. ,5138.90141, −59.20537}

Eigenvectors[GaONorm]

{{0., 0.639149, -0.767167, 0., 0., -0.054248},

{0.999694, -1.03967*10^-15, -8.65222*10^-16,-0.0198266, -0.014791, 0.},

{1.35329*10^-15, 0.768298, 0.640092, 0., -1.66533*10^-16, 0.},

{1.0646*10^-14, 1.65525*10^-16, 6.41077*10^-17, -0.597957, 0.801528, 0.},

{0.024736, 5.1856*10^-17, 1.75243*10^-17, 0.801283, 0.597774, 0.},

{0., 0.0347237, -0.0416787, 0., 0., 0.998527}}

These eigenvalues suggest that the peaks are split by 10 cm^{-1}, which is of course too long and would require more tuning to match our results, but the actual issue arises in the eigenvectors. Those 4^{th} and 5^{th} eigenvector lines imply that the ratio between the two peaks should be ~.6/.8, but the reality is that our sidebands are only a percent of the primary peak and no amount of tuning the current allowed parameters will fix this.

BIBLIOGRAPHY

[1] W. Schottky, Naturwissenschaften **26**, 843 (1938).

[2] J. Bardeen and W.H. Brattain, Phys. Rev. **74**, 230 (1948).

[3] H.J. Round, Electrical World **49**, 309 (1907).

[4] M.A. Becker, R. Vaxenburg, G. Nedelcu, P.C. Sercel, A. Shabaev, M.J. Mehl, J.G. Michopoulos, S.G. Lambrakos, N. Bernstein, J.L. Lyons, T. Stöferle, R.F. Mahrt, M.V. Kovalenko, D.J. Norris, G. Rainò, and A.L. Efros, Nature **553**, 189 (2018).

[5] G. Ablon, J Clin Aesthet Dermatol **11**, 21 (2018).

[6] P. Yu and M. Cardona, *Fundamentals of Semiconductors: Physics and Material Properties*, 2nd ed. (Springer, 1999).

[7] M. McCluskey and E. Haller, *Dopants and Defects in Semiconductors* (CRC press, 2012).

[8] A. West, *Solid State Chemistry and Its Applications*, 2nd ed. (2014).

[9] B. Allabergenov, S.-H. Chung, S.M. Jeong, S. Kim, and B. Choi, Opt. Mater. Express **3**, 1733 (2013).

[10] M.D. McCluskey, C.D. Corolewski, J. Lv, M.C. Tarun, S.T. Teklemichael, E.D. Walter, M.G. Norton, K.W. Harrison, and S. Ha, Journal of Applied Physics **117**, 112802 (2015).

[11] A.S. Barker and A.J. Sievers, Rev. Mod. Phys. **47**, S1 (1975).

[12] S.I. Stepanov, V.I. Nikolaev, V.E. Bougrov, and A.E. Romanov, 24 (n.d.).

[13] J.B. Varley, J.R. Weber, A. Janotti, and C.G. Van de Walle, Appl. Phys. Lett. **97**, 142106 (2010).

[14] L.L. Liu, M.K. Li, D.Q. Yu, J. Zhang, H. Zhang, C. Qian, and Z. Yang, Appl. Phys. A **98**, 831 (2010).

[15] T. Onuma, S. Fujioka, T. Yamaguchi, M. Higashiwaki, K. Sasaki, T. Masui, and T. Honda, Appl. Phys. Lett. **103**, 041910 (2013).

[16] Z. Galazka, K. Irmscher, R. Uecker, R. Bertram, M. Pietsch, A. Kwasniewski, M. Naumann, T. Schulz, R. Schewski, D. Klimm, and M. Bickermann, Journal of Crystal Growth **404**, 184 (2014).

[17] K. Takakura, D. Koga, H. Ohyama, J.M. Rafi, Y. Kayamoto, M. Shibuya, H. Yamamoto, and J. Vanhellemont, Physica B: Condensed Matter **404**, 4854 (2009).

[18] G.A. Battiston, R. Gerbasi, M. Porchia, R. Bertoncello, and F. Caccavale, Thin Solid Films **279**, 115 (1996).

[19] F.B. Zhang, K. Saito, T. Tanaka, M. Nishio, and Q.X. Guo, Journal of Crystal Growth **387**, 96 (2014).

[20] K. Sasaki, A. Kuramata, T. Masui, E.G. Víllora, K. Shimamura, and S. Yamakoshi, Appl. Phys. Express **5**, 035502 (2012).

[21] Y. Tomm, J.M. Ko, A. Yoshikawa, and T. Fukuda, Solar Energy Materials and Solar Cells **66**, 369 (2001).

[22] A. Kuramata, K. Koshi, S. Watanabe, Y. Yamaoka, T. Masui, and S. Yamakoshi, Jpn. J. Appl. Phys. **55**, 1202A2 (2016).

[23] K. Irmscher, Z. Galazka, M. Pietsch, R. Uecker, and R. Fornari, Journal of Applied Physics **110**, 063720 (2011).

[24] H. Peelaers and C.G.V. de Walle, Physica Status Solidi (b) **252**, 828 (2015).

[25] M. Mohamed, C. Janowitz, I. Unger, R. Manzke, Z. Galazka, R. Uecker, R. Fornari, J.R. Weber, J.B. Varley, and C.G. Van de Walle, Appl. Phys. Lett. **97**, 211903 (2010).

[26] H. Peelaers, J.L. Lyons, J.B. Varley, and C.G. Van de Walle, APL Materials **7**, 022519 (2019).

[27] J.R. Ritter, J. Huso, P.T. Dickens, J.B. Varley, K.G. Lynn, and M.D. McCluskey, Appl. Phys. Lett. **113**, 052101 (2018).

[28] M. Higashiwaki, K. Sasaki, A. Kuramata, T. Masui, and S. Yamakoshi, Phys. Status Solidi A **211**, 21 (2014).

[29] M. Higashiwaki, K. Sasaki, A. Kuramata, T. Masui, and S. Yamakoshi, Appl. Phys. Lett. **100**, 013504 (2012).

[30] K. Sasaki, M. Higashiwaki, A. Kuramata, T. Masui, and S. Yamakoshi, Journal of Crystal Growth **378**, 591 (2013).

[31] C.E. Nebel, Semicond. Sci. Technol. **18**, S1 (2003).

[32] R.D. Gould, S. Kasap, and A.K. Ray, in *Springer Handbook of Electronic and Photonic Materials*, edited by S. Kasap and P. Capper (Springer International Publishing, Cham, 2017), pp. 1–1.

[33] P. Capper, in *Springer Handbook of Electronic and Photonic Materials*, edited by S. Kasap and P. Capper (Springer International Publishing, Cham, 2017), pp. 1–1.

[34] N. Kolesnikov and E. Borisenko, *Modern Aspects of Bulk Crystal and Thin Film Preparation* (2012).

[35] P. Capper, S. Irvine, and T. Joyce, in *Springer Handbook of Electronic and Photonic Materials*, edited by S. Kasap and P. Capper (Springer International Publishing, Cham, 2017), pp. 1–1.

[36] J.H. Leach, K. Udwary, J. Rumsey, G. Dodson, H. Splawn, and K.R. Evans, APL Materials **7**, 022504 (2019).

[37] E.G. Víllora, K. Shimamura, Y. Yoshikawa, K. Aoki, and N. Ichinose, Journal of Crystal Growth **270**, 420 (2004).

[38] Z. Galazka, R. Uecker, K. Irmscher, M. Albrecht, D. Klimm, M. Pietsch, M. Brützam, R. Bertram, S. Ganschow, and R. Fornari, Crystal Research and Technology **45**, 1229 (2010).

[39] N. Ueda, H. Hosono, R. Waseda, and H. Kawazoe, Appl. Phys. Lett. **71**, 933 (1997).

[40] M.D. McCluskey, S.J. Jokela, K.K. Zhuravlev, P.J. Simpson, and K.G. Lynn, Appl. Phys. Lett. **81**, 3807 (2002).

[41] W. Ulrici, M. Czupalla, and M. Seifert, Physica Status Solidi (b) **210**, 551 (1998).

[42] P. Weiser, M. Stavola, W.B. Fowler, Y. Qin, and S. Pearton, Appl. Phys. Lett. **112**, 232104 (2018).

[43] J.L. Lyons, Semicond. Sci. Technol. **33**, 05LT02 (2018).

[44] B.E. Kananen, L.E. Halliburton, E.M. Scherrer, K.T. Stevens, G.K. Foundos, K.B. Chang, and N.C. Giles, Appl. Phys. Lett. **111**, 072102 (2017).

[45] O.F. Schirmer, A. Forster, H. Hesse, M. Wohlecke, and S. Kapphan, J. Phys. C: Solid State Phys. **17**, 1321 (1984).

[46] B. Andlauer, J. Schneider, and W. Tolksdorf, Physica Status Solidi (b) **73**, 533 (1976).

[47] M. Kleverman, P. Omling, L. Ledebo, and H.G. Grimmeiss, Journal of Applied Physics **54**, 814 (1983).

[48] M.D. McCluskey and E.E. Haller, in *Semiconductors and Semimetals.*, edited by R.K. Willardson, A.C. Beer, and N.H. Nickel (Academic Press, New York, 1999).

[49] J.B. Varley, H. Peelaers, A. Janotti, and C.G.V. de Walle, J. Phys.: Condens. Matter **23**, 334212 (2011).

[50] W.M. Hlaing Oo, S. Tabatabaei, M.D. McCluskey, J.B. Varley, A. Janotti, and C.G. Van de Walle, Phys. Rev. B **82**, 193201 (2010).

[51] M.E. Ingebrigtsen, J.B. Varley, A.Yu. Kuznetsov, B.G. Svensson, G. Alfieri, A. Mihaila, U. Badstübner, and L. Vines, Appl. Phys. Lett. **112**, 042104 (2018).

[52] C.A. Lenyk, N.C. Giles, E.M. Scherrer, B.E. Kananen, L.E. Halliburton, K.T. Stevens, G.K. Foundos, J.D. Blevins, D.L. Dorsey, and S. Mou, Journal of Applied Physics **125**, 045703 (2019).

[53] S.J. Pearton, D.P. Norton, K. Ip, Y.W. Heo, and T. Steiner, Journal of Vacuum Science & Technology B: Microelectronics and Nanometer Structures Processing, Measurement, and Phenomena **22**, 932 (2004).

[54] M.D. McCluskey and S.J. Jokela, J. Appl. Phys. 14 (n.d.).

[55] C. Persson, C. Platzer-Björkman, J. Malmström, T. Törndahl, and M. Edoff, Phys. Rev. Lett. **97**, 146403 (2006).

[56] C.-Y. Moon, S.-H. Wei, Y.Z. Zhu, and G.D. Chen, Phys. Rev. B **74**, 233202 (2006).

[57] B.K. Meyer, A. Polity, B. Farangis, Y. He, D. Hasselkamp, Th. Krämer, and C. Wang, Appl. Phys. Lett. **85**, 4929 (2004).

[58] M. Jaquez, K.M. Yu, M. Ting, M. Hettick, J.F. Sánchez-Royo, M. Wełna, A. Javey, O.D. Dubon, and W. Walukiewicz, Journal of Applied Physics **118**, 215702 (2015).

[59] J.S. McCloy, W. Wolf, E. Wimmer, and B.J. Zelinski, Journal of Applied Physics **113**, 023706 (2013).

[60] T.M. Friedlmeier, P. Jackson, A. Bauer, D. Hariskos, O. Kiowski, R. Wuerz, and M. Powalla, IEEE Journal of Photovoltaics **5**, 1487 (2015).

[61] M. Bär, A. Ennaoui, J. Klaer, T. Kropp, R. Sáez-Araoz, N. Allsop, I. Lauermann, H.-W. Schock, and M.C. Lux-Steiner, Journal of Applied Physics **99**, 123503 (2006).

[62] M.D. McCluskey, Journal of Applied Physics **87**, 3593 (2000).

[63] L. Genzel and W. Bauhofer, Z Physik B **25**, 13 (1976).

[64] D.W. Feldman, M. Ashkin, and J.H. Parker, Phys. Rev. Lett. **17**, 1209 (1966).

[65] Y.S. Chen, W. Shockley, and G.L. Pearson, Phys. Rev. **151**, 648 (1966).

[66] M. Balkanski, R. Beserman, and J.M. Besson, Solid State Communications **4**, 201 (1966).

[67] I.F. Chang and S.S. Mitra, Phys. Rev. **172**, 924 (1968).

[68] J.D. Ye, K.W. Teoh, X.W. Sun, G.Q. Lo, D.L. Kwong, H. Zhao, S.L. Gu, R. Zhang, Y.D. Zheng, S.A. Oh, X.H. Zhang, and S. Tripathy, Appl. Phys. Lett. **91**, 091901 (2007).

[69] Y. Chen, D.O. Dumcenco, Y. Zhu, X. Zhang, N. Mao, Q. Feng, M. Zhang, J. Zhang, P.-H. Tan, Y.-S. Huang, and L. Xie, Nanoscale **6**, 2833 (2014).

[70] J.H. Fertel and C.H. Perry, Phys. Rev. **184**, 874 (1969).

[71] S. Yu, K.W. Kim, L. Bergman, M. Dutta, M.A. Stroscio, and J.M. Zavada, Phys. Rev. B **58**, 15283 (1998).

[72] M. Mayer, Nuclear Instruments and Methods in Physics Research Section B: Beam Interactions with Materials and Atoms **332**, 176 (2014).

[73] L. Bergman, M. Dutta, and R.J. Nemanich, in *Raman Scattering in Materials Science*, edited by W.H. Weber and R. Merlin, 1st ed. (Springer, Berlin; New York, 2000).

[74] P.Y. Yu and M. Cardona, *Fundamentals of Semiconductors: Physics and Materials Properties* (Springer, Berlin; New York, 1996).

[75] J.F. Kong, W.Z. Shen, Y.W. Zhang, C. Yang, and X.M. Li, Appl. Phys. Lett. **92**, 191910 (2008).

[76] D. Strauch, B. Dorner, and K. Karch, in *Phonons 89 Proceedings of the Third International Conference on Phonon Physics and the Sixth International Conference on Phonon Scattering in Condensed Matter* (Federal Republic of Germany, 1989).

[77] W. Martienssen and H. Warlimont, editors , *Springer Handbook of Condensed Matter and Materials Data* (Springer-Verlag, Berlin Heidelberg, 2005).

[78] J. Serrano, A.H. Romero, F.J. Manjón, R. Lauck, M. Cardona, and A. Rubio, Phys. Rev. B **69**, 094306 (2004).

[79] A. Schleife, F. Fuchs, J. Furthmüller, and F. Bechstedt, Phys. Rev. B **73**, 245212 (2006).

[80] M. Guc, M. Neuschitzer, D. Hariskos, A. Bauer, W. Witte, W. Hempel, L. Calvo-Barrio, P. Pistor, A. Perez-Rodriguez, and V. Izquierdo-Roca, RSC Adv. **6**, 24536 (2016).

[81] D. Thapa, J. Huso, H. Che, M. Huso, J.L. Morrison, D. Gutierrez, M. Grant Norton, and L. Bergman, Applied Physics Letters **102**, 191902 (2013).

[82] D. Gammon, in *Raman Scattering in Materials Science*, edited by W.H. Weber and R. Merlin (Springer, New York, 2000).

[83] D. Gammon, S.W. Brown, E.S. Snow, T.A. Kennedy, D.S. Katzer, and D. Park, Science **277**, 85 (1997).

[84] W. Martienssen and H. Warlimont, *Springer Handbook of Condensed Matter and Materials Data* (Springer, Heidelberg; New York, 2005).

[85] M. Cardona and G. Harbeke, Phys. Rev. **137**, A1467 (1965).

[86] P. Schröer, P. Krüger, and J. Pollmann, Phys. Rev. B **47**, 6971 (1993).

[87] O. Brafman and I.T. Steinberger, Physical Review **143**, 501 (1966).

[88] J. Serrano, A. Cantarero, M. Cardona, N. Garro, R. Lauck, R.E. Tallman, T.M. Ritter, and B.A. Weinstein, Physical Review B **69**, (2004).

[89] S.K. Pandey, S. Pandey, V. Parashar, R.S. Yadav, G.K. Mehrotra, and A.C. Pandey, Nanoscale **6**, 1602 (2014).

[90] T.M. Friedlmeier, P. Jackson, A. Bauer, D. Hariskos, O. Kiowski, R. Wuerz, and M. Powalla, IEEE J. Photovoltaics **5**, 1487 (2015).

[91] M. Bär, A. Ennaoui, J. Klaer, T. Kropp, R. Sáez-Araoz, N. Allsop, I. Lauermann, H.-W. Schock, and M.C. Lux-Steiner, Journal of Applied Physics **99**, 123503 (2006).

[92] J. Huso, J.R. Ritter, D. Thapa, K.M. Yu, L. Bergman, and M.D. McCluskey, Journal of Applied Physics **123**, 161537 (2017).

[93] C.A. Arguello, D.L. Rousseau, and S.P.S. Porto, Phys. Rev. **181**, 1351 (1969).

[94] O. Madelung, U. Rössler, and M. Schulz, editors , in *II-VI and I-VII Compounds; Semimagnetic Compounds* (Springer Berlin Heidelberg, Berlin, Heidelberg, 1999), pp. 1–6.

[95] O. Madelung, U. Rössler, and M. Schulz, editors , in *II-VI and I-VII Compounds; Semimagnetic Compounds* (Springer Berlin Heidelberg, Berlin, Heidelberg, 1999), pp. 1–3.

[96] M. Cardona, R.K. Kremer, R. Lauck, G. Siegle, A. Muñoz, A.H. Romero, and A. Schindler, Phys. Rev. B **81**, 075207 (2010).

[97] W.G. Nilsen, Phys. Rev. **182**, 838 (1969).

[98] Y.C. Cheng, C.Q. Jin, F. Gao, X.L. Wu, W. Zhong, S.H. Li, and P.K. Chu, Journal of Applied Physics **106**, 123505 (2009).

[99] I.F. Chang and S.S. Mitra, Phys. Rev. **172**, 924 (1968).

[100] D.W. Feldman, M. Ashkin, and J.H. Parker, Phys. Rev. Lett. **17**, 1209 (1966).

[101] Y.S. Chen, W. Shockley, and G.L. Pearson, Phys. Rev. **151**, 648 (1966).

[102] R.J. Elliott, W. Hayes, G.D. Jones, H.F. Macdonald, and C.T. Sennett, Proc. R. Soc. Lond. A **289**, 1 (1965).

[103] H.C. Alt, Materials Science Forum **196–201**, 1577 (1995).

[104] Ewen. Smith and Geoffrey. Dent, *Modern Raman Spectroscopy: A Practical Approach* (J. Wiley, Hoboken, NJ, 2005).

[105] P.Y. Yu, Phys. Rev. B **20**, 5286 (1979).

[106] P.Y. Yu, in *Excitons* (Springer, Berlin, Heidelberg, 1979), pp. 211–253.

[107] P.Y. Yu, M.H. Pilkuhn, and F. Evangelisti, Solid State Communications **25**, 371 (1978).

[108] K. Ishikawa, N. Fujima, and H. Komura, Journal of Applied Physics **57**, 973 (1985).

[109] G.P. Montgomery, M.V. Klein, B.N. Ganguly, and R.F. Wood, Phys. Rev. B **6**, 4047 (1972).

[110] B.N. Ganguly, R.D. Kirby, M.V. Klein, and G.P. Montgomery, Phys. Rev. Lett. **28**, 307 (1972).

[111] R. Kaiser, W. Spencler, and W. Möller, Physica Status Solidi (b) **55**, 659 (1973).

[112] R.T. Harley, J.B. Page Jr., and C.T. Walker, Phys. Rev. Lett. **23**, 922 (1969).

[113] C. Raptis, Phys. Rev. B **33**, 1350 (1986).

[114] R.M. Martin and C.M. Varma, Phys. Rev. Lett. **26**, 1241 (1971).

[115] R. Zeyher, Solid State Communications **16**, 49 (1975).

[116] G. Uddin and Z. Azam, (n.d.).

[117] J.I. Wu, M.A. Dobrowolski, M.K. Cyrański, B.L. Merner, G.J. Bodwell, Y. Mo, and P. v R. Schleyer, Molecular Physics **107**, 1177 (2009).

[118] A. Mohr, P. Talbiersky, H.-G. Korth, R. Sustmann, R. Boese, D. Bläser, and H. Rehage, J. Phys. Chem. B **111**, 12985 (2007).

[119] D. Zhang, D. Liu, M. Li, Y. Yang, Y. Wang, H. Yin, J. Liu, B. Jia, and X. Wu, Analytica Chimica Acta **1033**, 180 (2018).

[120] O. Valdes-Aguilera, C.P. Pathak, and D.C. Neckers, Macromolecules **23**, 689 (1990).

[121] T.M. Figueira-Duarte and K. Müllen, Chem. Rev. **111**, 7260 (2011).

[122] D. Chercka, S.-J. Yoo, M. Baumgarten, J.-J. Kim, and K. Müllen, J. Mater. Chem. C **2**, 9083 (2014).

[123] W.-L. Jia, T. McCormick, Q.-D. Liu, H. Fukutani, M. Motala, R.-Y. Wang, Y. Tao, and S. Wang, J. Mater. Chem. **14**, 3344 (2004).

[124] N.P.E. Barry and B. Therrien, in *Organic Nanoreactors: From Molecular to Supramolecular Organic Compounds* (Academic Press, 2016).

[125] G.K. Bains, S.H. Kim, E.J. Sorin, and V. Narayanaswami, Biochemistry **51**, 6207 (2012).

[126] A. Munoz de la Pena, T. Ndou, J.B. Zung, and I.M. Warner, J. Phys. Chem. **95**, 3330 (1991).

[127] V. Glushko, M.S.R. Thaler, and C.D. Karp, Archives of Biochemistry and Biophysics **210**, 33 (1981).

[128] S. Hamai, J. Phys. Chem. **93**, 6527 (1989).

[129] G. Pistolis and A. Malliaris, J. Phys. Chem. B **108**, 2846 (2004).

[130] W. Kohn and L.J. Sham, Phys. Rev. **140**, A1133 (1965).

[131] J.P. Perdew, K. Burke, and M. Ernzerhof, Phys. Rev. Lett. **77**, 3865 (1996).

[132] C. Adamo and V. Barone, J. Chem. Phys. **110**, 6158 (1999).

[133] E. Runge and E.K.U. Gross, Phys. Rev. Lett. **52**, 997 (1984).

[134] C.M. Hegguilustoy, R.S. Montani, P.G. Del Rosso, M.J. Romagnoli, and R.O. Garay, Journal of Photochemistry and Photobiology A: Chemistry **347**, 67 (2017).

[135] J.F. Ogilvie, The Hydrogen Atom According to Wave Mechanics in Cartesian Coordinates. (2017.).

[136] K. Persson, LBNL Materials Project; Lawrence Berkeley National Laboratory (LBNL) (2014).